JETP Letters, Vol. 79, No. 4, 2004, pp. 141–143. Translated from Pis'ma v Zhurnal Éksperimental'noĭ i Teoreticheskoĭ Fiziki, Vol. 79, No. 4, 2004, pp. 175–177.

Estimate of the Mass Composition of Cosmic Rays above 4×10^{19} eV

A. A. Mikhaĭlov

Institute of Cosmophysical Research and Aeronomy, Siberian Division, Russian Academy of Sciences, pr. Lenina 31, Yakutsk, 677891 Russia

e-mail: mikhailov@ikfia.ysn.ru

Received September 28, 2003; in final form, December 3, 2003

The arrival directions of extensive air showers are analyzed on the basis of world data. It is found that the zenith-angle distributions for energies $E > 10^{19}$ eV and $E > 4 \times 10^{19}$ eV differ from each other. According to our estimates, the SUGAR array detects no showers above 10^{20} eV. The mass composition of ultrahigh-energy cosmic rays is estimated. Cosmic rays with $E > 4 \times 10^{19}$ eV most likely consist of superheavy nuclei. © *2004 MAIK "Nauka/Interperiodica".*

PACS numbers: 98.70.Sa; 96.40.Pq

The composition of cosmic rays is an important characteristic for determining their origin. The muon component of a shower is essential for solving this problem, because it is most sensitive to a change in the composition of primary radiation. Analysis of the AGASA data (Japan) for the muon component of extensive air showers (EASs) shows that cosmic rays with $E > 10^{19}$ eV consist predominately of light nuclei [1]. According to the HiRes (USA) results on the rate of displacement of the shower development maximum with an increase in energy, cosmic rays with $E \sim 2.5 \times 10^{19}$ eV also consist predominantly of light nuclei [2]. The Cherenkov-radiation-based estimate of the composition of cosmic rays at the Yakutsk EAS array shows that cosmic rays with $E \sim 3 \times 10^{19}$ eV also consist predominantly of protons [3]. Unfortunately, the experimental data in those works are interpreted on the basis of model calculations including NN and πN interactions of ultrahigh-energy particles, with the corresponding cross sections extrapolated from the accelerating region. This extrapolation can involve errors. Moreover, the corresponding experiments present difficulties, and errors are possible.

In this work, we propose a new method for estimating the composition of cosmic rays on the basis of clearly determined experimental data.

Figure 1 shows the distribution of showers with $E > 10^{19}$ eV over the zenith angle θ according to the (a) Yakutsk and (b) Haverah Park data [4]. The number of showers is 458 and 144, respectively. The dashed line is the expected number of events for the isotropic distribution of primary radiation according to [5]. Comparison of the observed and expected distributions of showers by the Pearson χ^2 criterion shows that they do not contradict each other at a significance level of 0.9. According to Fig. 1, inclined showers prevail in the distribution of showers with $E > 10^{19}$ eV, as is expected in the case of isotropic primary radiation.

Figure 2 shows the distribution of showers with $E > 4 \times 10^{19}$ eV according to the (a) Yakutsk and

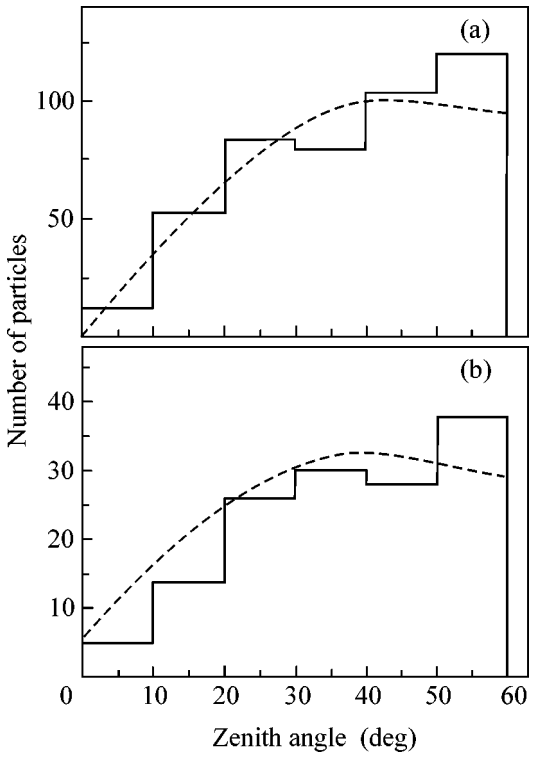

Fig. 1. Distribution of showers with $E > 10^{19}$ eV over the zenith angle θ for the (a) Yakutsk and (b) Haverah Park data. The dashed line is the number of showers expected in the isotropic case.

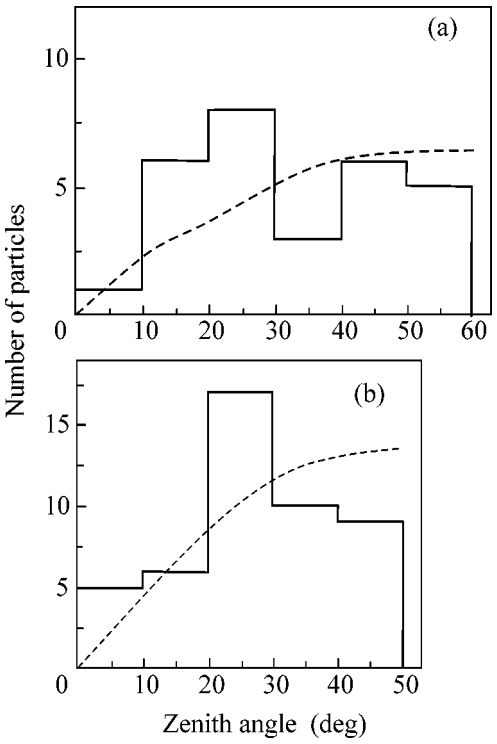

Fig. 2. Zenith-angle distribution of showers with $E > 4 \times 10^{19}$ eV for the (a) Yakutsk and (b) AGASA data. The dashed line is the number of showers expected in the isotropic case.

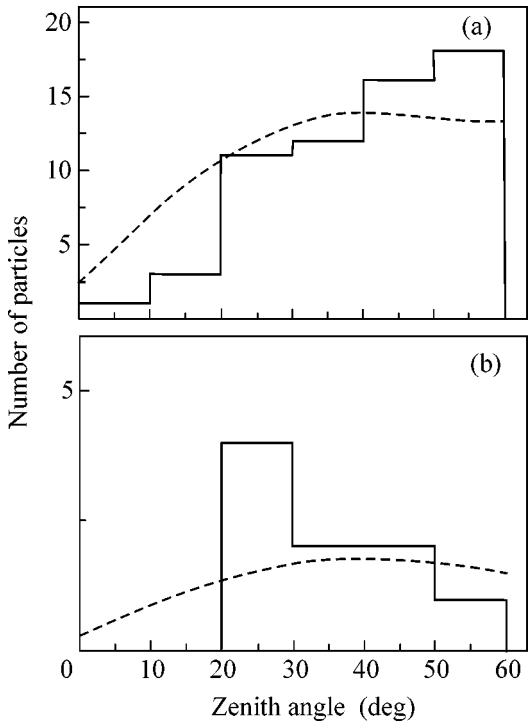

Fig. 3. Zenith-angle distribution of showers detected at the SUGAR array with $E >$ (a) 10^{19} and (b) 4×10^{19} eV according to the Sydney model and (a) with $E > 4 \times 10^{19}$ eV according to the Hillas-E model. The dashed line is the number of showers expected in the isotropic case.

(b) AGASA data [6] for 29 and 47 showers, respectively. The dashed line is the number of events that is expected for the isotropic case. As is seen in Fig. 2, the maximum of the distribution of the number of showers lies in the angular range 20°–30°, and the number of inclined showers is lower than the number expected in the isotropic case (see also [7]). According to the Pearson χ^2 criterion, the number of showers observed at the Yakutsk array (Fig. 2a) does not contradict the expected number of showers at a significance level of 0.15. This is also true for the AGASA data (Fig. 2b), though for a significance level of 0.1. According to the χ^2 criterion, the distribution combining both these distributions contradicts the number of events expected in the isotropic case at a significance level of 0.03. In this case, the number of showers observed in the angular range 20°–30° exceeds the expected number by a factor of 2.3σ, where σ is the standard deviation from the expected number of events.

Thus, the maximum in the zenith-angle distribution of showers with $E > 4 \times 10^{19}$ eV lies in the range of middle angles. Next, we analyze the zenith-angle distribution of showers detected at the SUGAR array. In [8], the energies of showers were estimated by two models, Sydney and Hillas-E. Figure 3 shows the distribution of showers with $E >$ (a) 10^{19} and (b) 4×10^{19} eV for the Sydney model. These distributions are similar to the ones obtained at the Yakutsk, Haverah Park, and AGASA arrays for the corresponding energies (Figs. 1, 2). According to the Hillas-E model, showers in Fig. 3a have energies above 4×10^{19} eV. In this case, the shower distribution contradicts the data from the other arrays mentioned above (Fig. 2). One can thus conclude that the Sydney model estimates the shower energies more correctly; i.e., according to this model, no shower was detected above 10^{20} eV at the SUGAR array [8].

To determine why the number of inclined showers with $E > 4 \times 10^{19}$ eV is smaller than the expected number (Fig. 2), we analyze these showers. As an example, Fig. 4 shows the electron–photon and muon components of two inclined showers with angles $\theta_1 = 58.7°$ and $\theta_2 = 54.5°$ and energies $E_1 = 1.2 \times 10^{20}$ eV and $E_2 = 2 \times 10^{19}$ eV. These showers are detected at the Yakutsk EAS array on May 7, 1989, and December 2, 1996, respectively. The axes of both showers were inside the array perimeter. As is seen in Fig. 4a, the particle densities in scintillation detectors (with 3-MeV detection threshold for electrons and photons) and muon detectors (1-GeV detection threshold) are equal to each other; i.e., the shower with $E_2 = 1.2 \times 10^{20}$ eV has only the muon component. The shower with the lower energy, $E_1 = 2 \times 10^{19}$ eV, has the electron–photon component at the same zenith angle θ (Fig. 4b). The

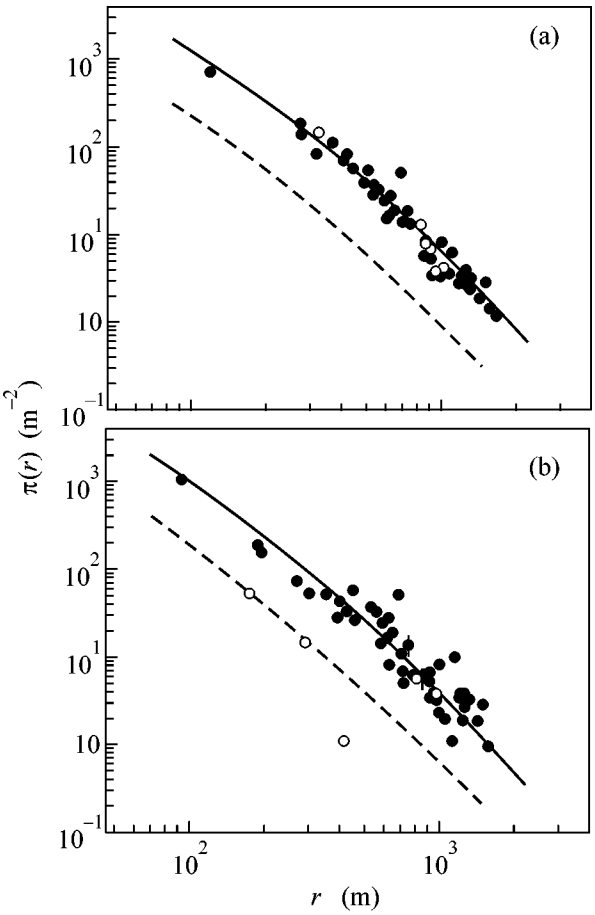

Fig. 4. Densities of (closed circles) electrons and photons and (open circles) muons at the distance r from the axis of the shower with (a) $E_1 = 1.2 \times 10^{20}$ and (b) $E_2 = 2 \times 10^{19}$ eV. The solid and dashed lines are the densities expected for the electron–photon and muon components, respectively.

increase in the muon fraction in inclined showers with an increase in energy was found for all the data in [9].

Thus, it is found for $E > 4 \times 10^{19}$ eV that, first, the number of observed inclined showers is relatively small and, second, the muon component starts to prevail in the inclined showers and dominates over the other components at $E \sim 10^{20}$ eV.

Previously, we have concluded that cosmic rays with $E > 4 \times 10^{19}$ eV are, most likely, Galactic cosmic rays [10]. The above facts can be treated as a change in the mass composition of Galactic cosmic rays toward heavier particles.

The qualitative pattern of the shower development is as follows. A heavy nucleus interacts with atoms in atmospheric layers lying higher than the layers of lighter nuclei and decays into individual nucleons. These nucleons produce lower-energy showers, and, likely, the inclined showers of relatively lower energy are more strongly absorbed in the atmosphere. For this reason, the corresponding inclined showers are in deficiency (Fig. 2), while in the inclined showers with relatively higher energies the muon component likely starts to dominate over the electron–photon component. Based on these facts, one can conclude that the mass composition of cosmic rays with $E > 4 \times 10^{19}$ eV is heavier than for $E \sim 10^{19}$ eV.

As was shown in [11], the cosmic rays with 10^{19} eV most likely consist of iron nuclei. Thus, cosmic rays with $E > 4 \times 10^{19}$ eV are likely heavier than the iron nuclei. Due to a change in the mass composition of primary radiation, the lateral distribution function of secondary particles in showers can change and, correspondingly, the estimate of shower energy changes (at the Yakutsk array, the shower energy is estimated from the density of electrons and photons at a distance of 600 m from the shower axis). Therefore, it is difficult to conclude to what extent the mass composition of cosmic rays with $E > 4 \times 10^{19}$ eV is heavier than the iron nuclei.

The Yakutsk EAS array is supported by the Ministry of Education of the Russian Federation, project no. 01-30.

REFERENCES

1. K. Shinozaki, M. Chikawa, M. Fukushima, *et al.*, in *Proceedings of 28th ICRC* (Tsukuba, 2003), Vol. 1, p. 401.
2. G. Archbold, P. V. Sokolsky, *et al.*, in *Proceedings of 28th ICRC* (Tsukuba, 2003), Vol. 1, p. 405.
3. S. Knurenko, V. A. Kolosov, Z. E. Petrov, and I. Ye. Sleptsov, in *Proceedings of 27th ICRC* (Hamburg, 2001), Vol. 1, p. 145.
4. J. Linsley, R. J. O. Reid, A. A. Watson, and M. Wada, in *Catalogue of Highest Energy Cosmic Rays*, Ed. by M. Wada (World Data Center C2, Tokyo, 1980), Vol. 1, p. 97.
5. N. N. Efimov, M. I. Pravdin, and A. A. Mikhailov, in *Proceedings of 18th ICRC* (Bangalore, 1983), Vol. 2, p. 149.
6. M. Takeda, N. Hayashida, K. Honda, *et al.*, astro-ph/9902239.
7. A. A. Mikhailov, in *Proceedings of 28th ICRC* (Tsukuba, 2003), Vol. 1, p. 441.
8. M. M. Winn, J. Ulrichs, L. S. Peak, *et al.*, J. Phys. G: Nucl. Phys. **12**, 653 (1986).
9. A. V. Glushkov, I. T. Makarov, E. S. Nikiforova, *et al.*, Astropart. Phys. **4**, 15 (1995).
10. A. A. Mikhaĭlov, Pis'ma Zh. Éksp. Teor. Fiz. **77**, 181 (2003) [JETP Lett. **77**, 151 (2003)].
11. A. A. Mikhaĭlov, Pis'ma Zh. Éksp. Teor. Fiz. **72**, 233 (2000) [JETP Lett. **72**, 160 (2000)].

Translated by R. Tyapaev

JETP Letters, Vol. 79, No. 4, 2004, pp. 144–147. Translated from Pis'ma v Zhurnal Éksperimental'noĭ i Teoreticheskoĭ Fiziki, Vol. 79, No. 4, 2004, pp. 178–182.

New Scheme of a Petawatt Laser Based on Nondegenerate Parametric Amplification of Chirped Pulses in DKDP Crystals

N. F. Andreev[1], V. I. Bespalov[1], V. I. Bredikhin[1], S. G. Garanin[2], V. N. Ginzburg[1], K. L. Dvorkin[1], E. V. Katin[1], A. I. Korytin[1], V. V. Lozhkarev[1], O. V. Palashov[1], N. N. Rukavishnikov[2], A. M. Sergeev[1], S. A. Sukharev[2], G. I. Freĭdman[1], E. A. Khazanov[1,*], and I. V. Yakovlev[1]

[1] *Institute of Applied Physics, Russian Academy of Sciences, ul. Ul'yanova 46, Nizhni Novgorod, 603950 Russia*

** e-mail: khazanov@appl.sci-nnov.ru*

[2] *All-Russia Research Institute of Experimental Physics, Russian Federal Nuclear Center, Arzamas-16, Nizhni Novgorod oblast, 607188 Russia*

Received December 29, 2003

The ultra-broadband phase matching was experimentally observed in a DKDP crystal upon parametric amplification of signal radiation with a wavelength of 911 nm in a pump field with a wavelength of 527 nm. The original scheme was used to excite the first parametric amplification stage by chirped pulses of idler radiation with a wavelength of 1250 nm. The saturated gain of a three-stage parametric amplifier was equal to 10^8. © *2004 MAIK "Nauka/Interperiodica".*

PACS numbers: 42.65.Yj; 42.60.By

Parametric amplification of chirped femtosecond laser pulses has been actively devised in the last several years as one of the promising methods of reaching a petawatt level for optical radiation. For the lower power levels, this idea was formulated probably about 15 years ago [1]. However, it has attracted practical interest in achieving the highest (multipetawatt) power only recently, after the design of femtosecond lasers with pulse durations as short as 10 fs and nonlinear crystals with an aperture up to 40 cm [2, 3].

In the theoretical and experimental works [2–5] devoted to the development of ultrahigh-power laser sources, a KDP crystal was considered and used as a nonlinear element in the final stages of parametric amplifiers. The use of second-harmonic radiation from neodymium lasers with a wavelength of 527 nm as a pump radiation holds the most promise for the development of powerful systems. The corresponding maximal amplification bandwidth in a KDP crystal is achieved in the case of degenerate interaction for a signal radiation wavelength of ~1054 nm. In the experiments [4, 5], the initial duration of amplified chirped pulses was no less than 100 fs because of the difficulties associated with the fabrication of shorter-duration femtosecond oscillators in the wavelength range of ~1054 nm.

Analysis of the parametric interaction in a highly deuterated DKDP crystal suggests [6] that the characteristics of this crystal are substantially different from the characteristics of a KDP crystal. According to the most reliable Selmeier's dispersion relations for DKDP [7], the broadband matching in this crystal at a pump wavelength of 527 nm occurs upon noncollinear wavevector interaction in the amplification wavelength range 800–1054 nm. Moreover, calculations show that ultra-broadband phase matching in DKDP takes place for the central wavelength $\lambda_{10} \approx 910$ nm of signal radiation. In this case, the second-order wave-mismatch dispersion tends to zero and the amplification bandwidth is determined by the third-order dispersion. If the conditions for the ultra-broadband matching are met, the maximal amplification bandwidth in DKDP, all things being the same, is approximately twice as large as in KDP and is equal to 2300–2500 cm^{-1} for a pump intensity of 1–4 GW/cm^2 (Fig. 1), allowing the amplification of pulses with a duration of ~15 fs.

In the DKDP parametric amplifiers, chirped pulses of a femtosecond Ti:Sapphire laser can serve as a source of signal pulses, whose initial duration at a wavelength of ~910 nm can reach 30 fs. It is also shown in this work that signal radiation with $\lambda_{10} \sim 910$ nm can be excited at the input of the first amplifier stage by the chirped pulses of a femtosecond Cr:Forsterite laser, and they can generate pulses with a duration of 30 fs at a wavelength of ~1250 nm, coinciding with the wavelength of frequency-conjugated radiation.

To use the entire DKDP amplification bandwidth and produce, using DKDP amplifiers, pulses with a duration of 10–20 fs, it is necessary to devise femtosecond oscillators generating pulses of the corresponding duration at wavelengths of ~910 nm (or ~1250 nm), e.g., to devise a femtosecond parametric oscillator, as was proposed in [8] for KDP amplifiers.

0021-3640/04/7904-0144$26.00 © 2004 MAIK "Nauka/Interperiodica"

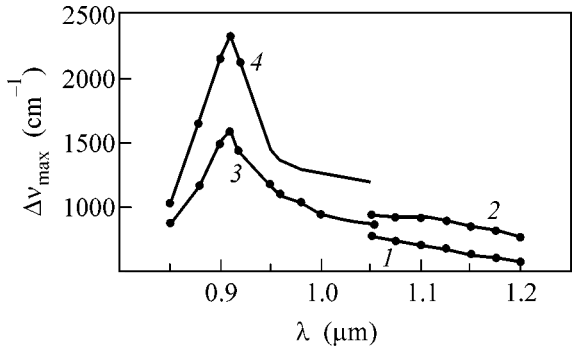

Fig. 1. Amplification bandwidth of signal radiation as a function of its wavelength for KDP and DKDP crystals, a pump intensity of 1 GW/cm^2, and a stage gain of ~10^3: (*1*) KDP crystal with broadband phase matching; (*2*) the same with optimized angles; (*3*) DKDP crystal with ultrabroadband matching; and (*4*) the same with optimized angles.

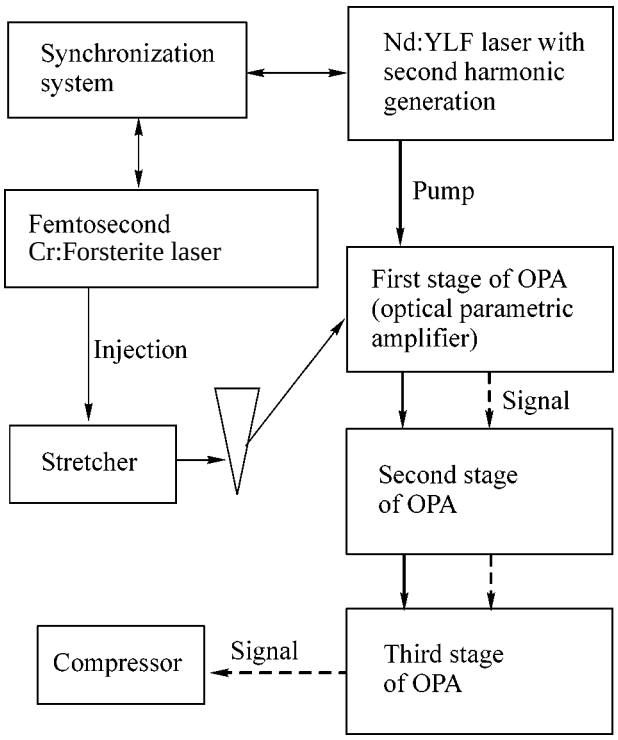

Fig. 2. Schematic block diagram of the experimental setup.

In the experiments (Fig. 2), a femtosecond Cr:Forsterite laser with a mean power of ~0.25 W generating pulses of a duration of ~40 fs with a spectrum FWHM of ~400 cm^{-1} was used as a source of injected radiation. A parametric amplifier was pumped by the second harmonic radiation from a Nd:YLF laser with a wavelength of 527 nm, a pulse energy of 1 J, and a pulse duration of 1.5–1.7 ns. The pulse repetition rate was 2 Hz. The pump intensity at the input of the first parametric amplifier stage had almost uniform cross-sectional distribution and was equal to ~1 GW/cm^2.

A two-stage synchronization scheme [9] provided the simultaneous (to within ~50 ps) passage of the pump and amplified radiation pulses through the nonlinear crystals. The nonlinear DKDP elements in the parametric amplifier were 70 mm in length, and the deuteration level was 88.7%.

The requirements to the stretcher dispersion characteristic change significantly if the signal is excited by the idler wave. In this case, the phase of the compressed amplified signal pulse is given by the expression $\Phi(\Omega) = \Phi_{com}(\omega_{10} + \Omega) - \Phi_{str}(\omega_{20} - \Omega)$ (ω_{10} and ω_{20} are the central frequencies of the signal and injected radiations, respectively, and Ω is the detuning from the central frequency). It follows from this expression that the quadratic dispersion of the system is zero if the second-order dispersions of the stretcher and compressor are identical. As for the cubic dispersion of the system, it can turn to zero only if the third derivatives of the phase incursions in the stretcher and compressor are opposite in sign. Our calculations showed that this requirement can be satisfied if, by analogy with a compressor, a system with negative quadratic dispersion and two prisms with identical apex angles is used as a stretcher. For a certain choice of parameters of such a system, one can not only vary cubic dispersion within a relatively narrow range, as was demonstrated in [10], but even change the sign of this dispersion and, thereby, exactly compensate the compressor dispersion up to the fourth order inclusive.

A stretcher having a transmission band of 1000 cm^{-1} and stretching 40-fs pulses of the injected radiation to a half-height duration of 0.5 ns was devised on the basis of a holographic diffraction grating with a groove density of 1200 mm^{-1} and the appropriately fabricated prisms.

In our scheme with the excitation of the parametric amplifier by the idler wave, the spectral components of a signal radiation with $\lambda_{10} \sim 910$ nm propagate unidirectionally only if the propagation direction of the injected radiation components change according to the law

$$\mathbf{k}_2(\omega_{20} - \Omega) = \mathbf{k}_3 - \mathbf{z}_0 k_1(\omega_{10} + \Omega),$$

where $\mathbf{k}_i$ are the interacting wavevectors and $\mathbf{z}_0$ is the unit vector in the direction of a signal wave. In the experiment, this was achieved by passing the injected idler beam through a dispersing prism. The image of this beam at the prism output was translated to the first amplifier stage by a narrowing telescope. This diminished the effect of pump radiation divergence on the amplification process. The radius of the exciting injected beam in the crystal was ~1 mm.

The pump and signal beams were fed to the input of the second amplifier stage through a system of mirrors without changing the scale. From the output of the second stage, the signal beam was translated to the input of

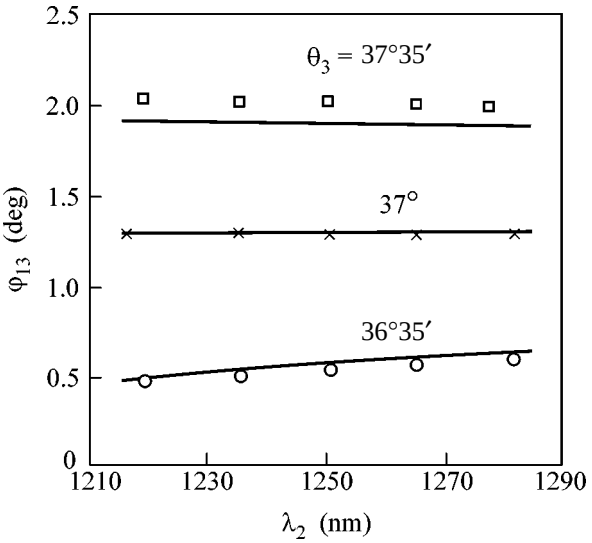

Fig. 3. Theoretical (curves) and experimental (dots) dependences of the exterior angle φ_{13} on λ_2 for different values of θ_3.

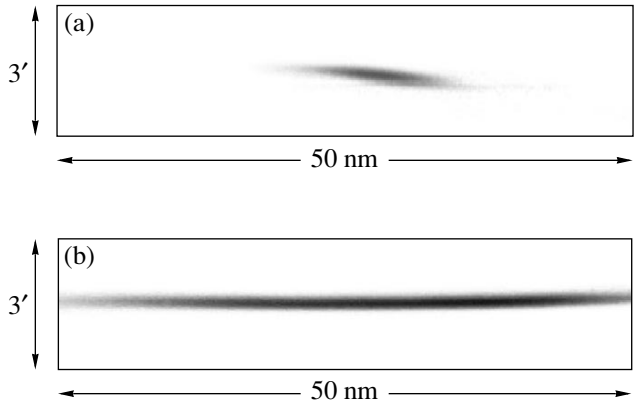

Fig. 4. Spectrum diagram of signal radiation in the critical plane in the lens focus f = 406 mm: (a) for the collimated injected radiation and (b) for the optimized angular chirp.

the third stage with a fourfold magnification, while the pump beam was fed with a 1.1-fold demagnification.

To determine the conditions for broadband amplification in a DKDP crystal, the phase-matching angles between the interacting waves were measured as functions of the amplified wavelength. The angle $\varphi_{13}(\lambda_2)$ between the pump beam and the signal-radiation-matching direction in the principal plane was measured for different angles θ_3 between the pump wavevector and the crystal axis. Figure 3 shows a good coincidence between the experimental and theoretical curves calculated using the Selmeier relations [7]. For the optimal angle $\theta_{30} \sim 37°$, the tuning of the injected wavelength did not change the direction of the signal wavevector in the spectral range considered. This result was also confirmed by the studies of spectral and angular distributions of parametric superradiance in the range $\lambda_1 \sim$ 885–935 nm.

The propagation direction of the signal spectral components amplified in the first and second stages was studied as a function of the wavelength for different angular chirps of the injected radiation at the output of a quartz prism. To this end, the signal beam was focused onto the entrance slit of a spectrometer with a CCD camera placed in the plane of its exit slit. Thus, we measured the dependence of the direction of amplified signal on its frequency (signal spectrum-diagram) in the principal plane. For a collimated injected beam, the angular spectrum of the output signal was frequency-dependent (Fig. 4a), and the signal beam became collimated upon setting the dispersing prism at a calculated angle [11]. This was accompanied by a significant broadening of the spectrum of amplified signal (Fig. 4b).

For an energy of ~1 J of the pump pulses at the input of the system, the energy of signal pulses reached ~0.1 J after the third amplifier stage, and the amplification became saturated (Fig. 5). Due to the losses on the path, the pump-pulse energy at the input of the third stage was ~0.7 J and, correspondingly, the energy transformation coefficient for the pump beam in the third stage was ~15%. This is in accordance with the results of numerical simulation of the amplifier operation with allowance for the relative walk-off of the interacting beams.

At the output of the second stage, the amplified beam was close to Gaussian with a radius of ~0.1 cm and a nearly diffractional divergence. After the amplification in the third stage, it had a clearly defined outer boundary with a diameter of ~0.8 cm, corresponding to the pump beam. The directivity diagram of signal beam at the output of the third stage was symmetric and close to the diagram of a beam with uniform intensity distribution and flat phase front (Fig. 6).

For a gain of $\sim 10^8$, the spectral width of signal radiation markedly decreases, because the side frequencies are amplified in a pump field of lower intensity. However, spectrum narrowing is insignificant after stretching the pulse to 0.5 ns. The spectral width of the amplified pulse was approximately 30% narrower than the spectral width of the injected signal. The compression of this pulse without fine adjustment of the stretcher–compressor system gave pulses with a duration of ~80 fs.

Numerical simulation of the parametric amplification process shows that, upon the amplification to a multiterawatt or petawatt level, the spectrum narrowing, to a large extent, can be compensated by the "supersaturation" effect [3]. The energy transformation coefficient for the pump pulse increases to ~25–30%.

Our experimental results and the results of numerical simulation suggest that petawatt pulses with a duration of up to 30–50 fs can be obtained upon the excitation of a DKDP parametric amplifier by the idler radia-

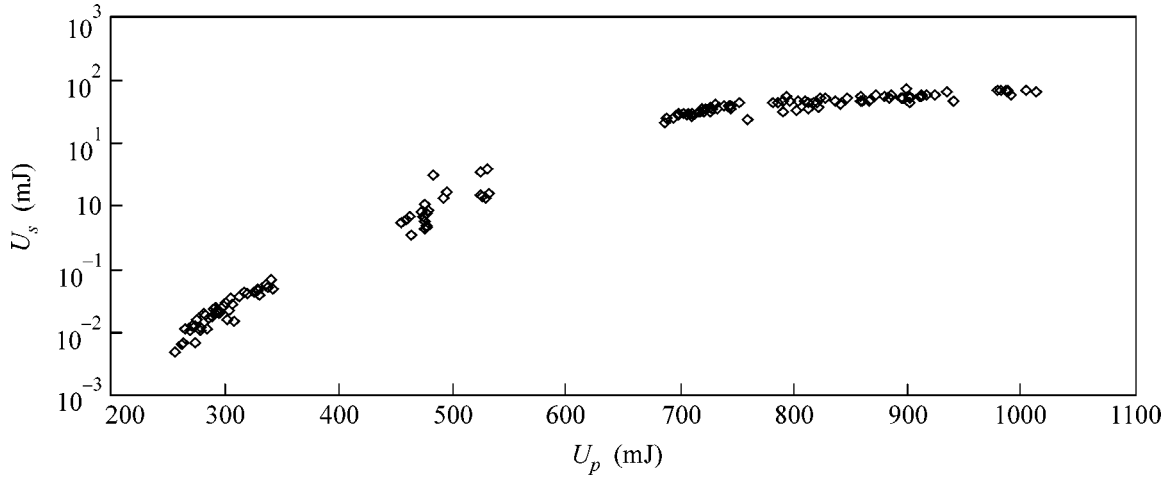

Fig. 5. Dependence of the energy U_s of signal pulses after the third amplification stage on the energy U_p of pump pulses.

tion. This will require the use of a wide-aperture nonlinear DKDP element and pump pulses with a duration of ~1.5 ns and energy of ~1 kJ at a wavelength of 527 nm. Joint work in this direction is in progress at the Institute of Applied Physics RAS and the All-Russia Research Institute of Experimental Physics of the Russian Federal Nuclear Center (Arzamas-16) on the basis of a powerful neodymium phosphate glass facility LUCh [12]. At the Institute of Applied Physics, nonlinear elements with a cross section of ~10^2 cm^2 have already been fabricated and the preparation for the experiment aimed at reaching ~100 TW and for the fabrication of elements with a cross section of 10^3 cm^2 has been started.

This work was supported by the Russian Foundation for Fundamental Research (project no. 02-02-17474), the Program of Leading Scientific Schools (project no. NSh-1625.2003.2), the Program of the Presidium of the Russian Academy of Sciences, and the program of the Section of Physical Sciences of the Russian Academy of Sciences.

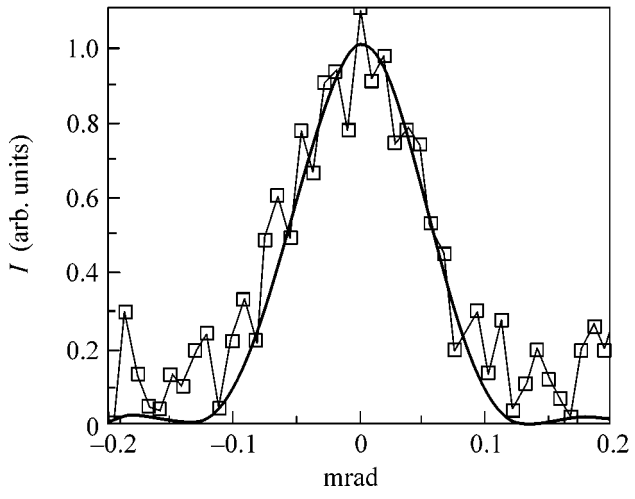

Fig. 6. Directivity diagram I of a signal beam at the output of third amplifier stage (dots). Solid line is the theoretical dependence for a beam with a diameter of 8 mm and uniform intensity distribution.

REFERENCES

1. A. Piskarskas, A. Stabinis, and A. Yankauskas, Usp. Fiz. Nauk **150**, 127 (1986) [Sov. Phys. Usp. **29**, 869 (1986)].
2. I. N. Ross, P. Matousek, M. Towrie, *et al.*, Opt. Commun. **144**, 125 (1997).
3. P. Matousek, B. Rus, and I. N. Ross, IEEE J. Quantum Electron. **36**, 158 (2000).
4. I. N. Ross, J. L. Collier, P. Matousek, *et al.*, Appl. Opt. **39**, 2422 (2000).
5. X. D. Yang, Z. Z. Xu, Y. X. Leng, *et al.*, Opt. Lett. **27**, 1135 (2002).
6. G. Freidman, N. Andreev, V. Ginzburg, *et al.*, Proc. SPIE **4630**, 135 (2002).
7. K. W. Kirby and L. G. DeShazer, J. Opt. Soc. Am. B **4**, 1072 (1987).
8. Z. Z. Xu, X. D. Yang, Y. X. Leng, *et al.*, Chin. Opt. Lett. **1**, 24 (2003).
9. E. V. Katin, V. V. Lozhkarev, O. V. Palashov, and E. A. Khazanov, Kvantovaya Élektron. (Moscow) **33**, 836 (2003).
10. S. Kane, J. Squier, J. V. Rudd, and G. Mourou, Opt. Lett. **19**, 1876 (1994).
11. G. Freidman, N. Andreev, V. Bespalov, *et al.*, in *Postdeadline Papers of Conference on Lasers and Electro-Optics, CLEO-2002* (Long Beach, Calif., 2002), CPDA9-1.
12. N. N. Beznasyuk, I. V. Galakhov, S. G. Garanin, *et al.*, in *Book of Abstracts of XXVII European Conference on Laser Interaction with Matter ECLIM-2002* (Moscow, 2002), p. 61.

Translated by V. Sakun

JETP Letters, Vol. 79, No. 4, 2004, pp. 148–154. Translated from Pis'ma v Zhurnal Éksperimental'noĭ i Teoreticheskoĭ Fiziki, Vol. 79, No. 4, 2004, pp. 183–189.

Ordered Phases of Lithium Nickelite $Li_{1-x-z}Ni_{1+x}O_2$

A. I. Gusev

Institute of Solid-State Chemistry, Ural Division, Russian Academy of Sciences, Yekaterinburg, 620219 Russia
e-mail: gusev@ihim.uran.ru

Received January 5, 2004

A symmetry analysis of ordering in lithium nickelite $Li_{1-x-z}Ni_{1+x}O_2$ ($Li_{1-x-z}\square_yNi_{1+x}O_2$) was performed with regard to the substitution of Li and Ni atoms and the occurrence of structural vacancies □ in the metal sublattice. For all the ordered phases, the $\mathbf{k}_9^{(3)}$ ray of the Lifshitz $\{\mathbf{k}_9\}$ star is present in the order–disorder transition channel. This ray determines the consecutive alternation of atomic planes filled with only Ni atoms or only Li atoms and vacancies in the $[1\bar{1}1]_{B1}$ direction. It was shown that the rhombohedral ordered $LiNiO_2$ phase is formed in the defect-free lithium nickelite, whereas a family of three monoclinic $Li_3\square Ni_4O_8$ ($C2/m$ space group) and $Li_2\square Ni_3O_6$ ($C2/m$ and $C2$ space groups) superstructures arises as the concentration of structural vacancies increases. For all the superstructures, the order–disorder phase-transition channels were determined and the distribution functions of Li and Ni atoms have been calculated. The long-range order parameters describing each superstructure were found as functions of the $Li_{1-x-z}Ni_{1+x}O_2$ composition. © *2004 MAIK "Nauka/Interperiodica".*

PACS numbers: 61.50.Ks; 61.66.Fn; 64.70.Kb

Lithium nickelite, the related oxide compounds $LiMO_2$, and their solid solutions are being studied intensively as rather promising cathode materials for chemical power sources [1]. The implementation of their high potentialities is hampered by the instability of their properties caused by the complicated defect structure, which is primarily due to the lithium nonstoichiometry and to the possibility of ordering and disordering. The crystal structures of complex oxides $LiMO_2$ (M = Ni, Co) are derivatives of the $B1$-type (NaCl) structure and differ in the way of ordering of lithium and transition-metal cations in the $(111)_{B1}$ or equivalent $(\bar{1}11)_{B1}$, $(1\bar{1}1)_{B1}$, and $(11\bar{1})_{B1}$ planes of the face-centered cubic (fcc) sublattice. In the cases where lithium and transition-metal ions separately occupy alternating metal $(111)_{B1}$ planes of the basic cubic lattice, layered structures are formed.

Several ways of writing the chemical formula for lithium nickelite are used in the literature: Li_xNiO_2 [2–4], $Li_{1-x}Ni_{1+x}O_2$ [3, 5], and $Li_{x'}Ni_{2-x'}O_2$ (or $Li_yNi_{1-y}O$, where $y = x'/2$) [6–8]. The difference in the formulas is associated with a difference in the understanding of the lithium nickelite structure. A solid solution $Li_yNi_{1-y}O$ ($0 \le y \le 0.5$) is formed in the ternary Li–Ni–O system, whose extreme members are cubic nickel monoxide NiO (at $y = 0$) and rhombohedral (trigonal) stoichiometric $LiNiO_2$ lithium nickelite (at $y = 0.5$, i.e., $Li_{0.5}Ni_{0.5}O$). The structure of stoichiometric $LiNiO_2$ lithium nickelite can be considered as a result of the ordering of lithium and nickel atoms (ions) in the basic cubic structure of the $B1$ type. The $Li_{1-x}Ni_{1+x}O_2$ and $Li_{x'}Ni_{2-x'}O_2$ formulas are, in essence, similar ($x' = 1 - x$) and reflect the substitution of nickel for lithium in the solid solution but take no account of the possible occurrence of structural vacancies in the lithium sublattice of rhombohedral lithium nickelite. In fact, if the composition of lithium nickelite departs from the stoichiometric $LiNiO_2$, structural vacancies appear in the lithium sublattice whose concentration can be rather high. The occurrence of vacancies is taken into account in the Li_xNiO_2 formula (or $Li_x\square_{1-x}NiO_2$, where □ is a structural vacancy in the lithium sublattice) [2–4]; however, the substitution of nickel for lithium is not taken into account in this representation. To take into account the substitution of nickel for lithium upon the formation of a solid solution between NiO and $LiNiO_2$ and the occurrence of structural vacancies in the metal sublattice, the lithium nickelite formula should be represented as $Li_{1-x-z}Ni_{1+x}O_2$ ($Li_{1-x-z}\square_zNi_{1+x}O_2$). This formula takes into account the specific features of the lithium nickelite structure and allows the ordering of lithium nickelite to be analyzed using the atomic distribution function and the concept [9–11] of the order–disorder phase transition channel in nonstoichiometric compounds.

Up to now, the majority of structural investigations of lithium nickelite and related compounds have been empirical; a theoretical analysis of the structures has not been performed. This prevents the specific features of experimentally observed ordered phases from being understood; moreover, it is not possible to predict the ordered phases that are formed and the concentration

regions in which they arise. In this work, we perform a theoretical symmetry analysis of the experimentally observed and theoretically possible superstructures of $Li_{1-x-z}\square_z Ni_{1+x}O_2$ lithium nickelite, from the determination of the order–disorder transition channel to the calculation of the distribution function of the ordering atoms.

The unit cell of the rhombohedral (trigonal) ordered phase $Li_{1-x-z}Ni_{1+x}O_2$ is shown in Fig. 1. In the coordinates of the basic cubic structure, the unit cell of the perfect rhombohedral ($R\bar{3}m$ (D_{3d}^5) space group) $LiNiO_2$ phase has the translation vectors $\mathbf{a}_{tr} = \frac{1}{2}\langle 1\bar{2}1\rangle_{B1}$, $\mathbf{b}_{tr} = \frac{1}{2}\langle 2\bar{1}1\rangle_{B1}$, and $\mathbf{c}_{tr} = \frac{1}{2}\langle 1\bar{1}2\rangle_{B1}$. The rhombohedral cell is primitive with respect to the lithium atoms and contains one Li atom in the 1*a* (0 0 0) position, one Ni atom in the 1*b* (1/2 1/2 1/2) position, and two O atoms in the 2*c* (1/4 1/4 1/4) position. The nonprimitive cell is hexagonal, has a three times larger volume, and contains three Li atoms, three Ni atoms, and six O atoms in the 3*a* (0 0 0), 3*b* (0 0 1/2), and 6*c* (0 0 1/4) positions, respectively. This cell has the translation vectors $\mathbf{a}_{hex} = \frac{1}{2}\langle 112\rangle_{B1}$, $\mathbf{b}_{hex} = \frac{1}{2}\langle 110\rangle_{B1}$, and $\mathbf{c}_{hex} = 2\langle 1\bar{1}1\rangle_{B1}$.

In order to determine the structural order–disorder phase-transition channel through which the rhombohedral (trigonal) $LiNiO_2$ superstructure with the $R\bar{3}m$ space group is formed, the reciprocal-lattice vectors of the superstructure were calculated and the $\{\mathbf{k}_s\}$ stars to which these vectors belong were determined. The calculation showed that the rhombohedral superstructure of lithium nickelite is formed through the phase-transition channel that involves one ray $\mathbf{k}_9^{(3)} = \mathbf{b}_2/2$ of the Lifshitz $\{\mathbf{k}_9\}$ star (the subscript and superscript of the wave vector correspond to the star number and the ray number in the star, respectively; from here on, the numbering of wave-vector stars $\{\mathbf{k}_s\}$ is given according to [9–13], and the numbering of their rays $\mathbf{k}_s^{(j)}$ corresponds to [9–11]; $\mathbf{b}_1 = \{-1\ 1\ 1\}$, $\mathbf{b}_2 = \{1\ -1\ 1\}$, and $\mathbf{b}_3 = \{1\ 1\ -1\}$ are the basis vectors of the reciprocal lattice of fcc crystal in $2\pi/a_{B1}$ units).

The found order–disorder transition channel allows one to calculate the distribution functions for lithium and nickel atoms in the rhombohedral superstructure. The star $\{\mathbf{k}_9\}$ is characterized by the long-range order parameter $\eta_9^{(M)}$ in the fcc metal sublattice. The arrangement of atoms of sort ν in an ordering crystal is described by the distribution function $n^{(\nu)}(\mathbf{r})$ that possesses symmetry of the ordered lattice and represents the probability of finding an atom of the given sort at the crystal lattice site **r**. In the disordered $Li_{1-x-z}Ni_{1+x}O_2$

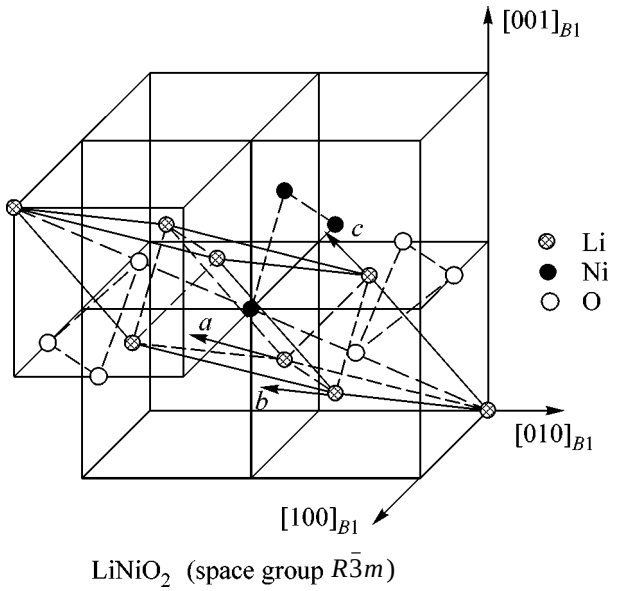

Fig. 1. Position of the rhombohedral ($R\bar{3}m$ space group) unit cell of $LiNiO_2$ lithium nickelite in the lattice with the *B*1 structure. The consecutive alternation of atomic planes filled with only Li atoms, only O atoms, or only Ni atoms in the $[1\bar{1}1]_{B1}$ direction is shown.

($Li_{1-x-z}\square_z Ni_{1+x}O_2$), the probabilities $n^{(Li)}(\mathbf{r})$, $n^{(Ni)}(\mathbf{r})$, and $n^{(\square)}(\mathbf{r})$ coincide with the fraction of metal sublattice sites occupied by lithium or nickel atoms or with the fraction of vacant sites, respectively; i.e., $n^{(Li)}(\mathbf{r}) = (1 - x - z)/2$, $n^{(Ni)}(\mathbf{r}) = (1 + x)/2$, and $n^{(\square)}(\mathbf{r}) = z/2$.

The order–disorder transition induces a spatially periodic modulation of the atomic uniform distribution over the crystal lattice sites in the disordered compound, resulting in the formation of the ordered phase. This modulation, i.e., the departure of the probability $n^{(\nu)}(\mathbf{r})$ from its value for the disordered (random) distribution, can be represented as a superposition of several plane concentration waves [14]. The wave vectors of the concentration waves are the superstructure vectors that form the order–disorder phase-transition channel [10, 11, 15]. In the method of static concentration waves [14], the distribution function is expressed through the fraction of sites y_ν occupied by the atoms of a given sort ν in the ordering sublattice and through the modulation, i.e., superposition of static waves.

In the case under consideration, the metal fcc sublattice represents the Ising lattice, in which the ordering of Ni atoms occurs, on the one hand, and Li atoms and structural vacancies, on the other. The translation vectors determining the position of its sites **r** have the form $\mathbf{r} = x_I a_1 + y_I a_2 + z_I a_3$, where x_I, y_I, and z_I are the coordinates of metal fcc sublattice sites and a_1, a_2, and a_3 are the fundamental translations of the basic lattice in the $[100]_{B1}$, $[010]_{B1}$, and $[001]_{B1}$ directions. The calculation

performed showed that the distribution function of nickel atoms in the rhombohedral ($R\bar{3}m$ space group) $Li_{1-x-z}Ni_{1+x}O_2$ superstructure takes the form

$$n^{(Ni)}(x_I, y_I, z_I) = (1+x)/2 - (\eta_9^{(M)}/2)\cos[\pi(x_I - y_I + z_I)] \quad (1)$$

and depends on one long-range order parameter $\eta_9^{(M)}$. The distribution function (1) takes two values on all sites of the metal fcc sublattice: $n_{Ni}^{(Ni)} = (1+x)/2 + \eta_9^{(M)}/2$ and $n_{Li}^{(Ni)} = (1+x)/2 - \eta_9^{(M)}/2$. The former value, $n_{Ni}^{(Ni)}$, is the probability of finding Ni atoms at the nickel sublattice sites, and the latter, $n_{Li}^{(Ni)}$, is the probability of finding Ni atoms at the lithium sublattice sites (from here on, the subscript in the designations of probabilities n and concentrations signifies the sublattice under consideration, and the superscript corresponds to the sorts of atoms arranged at the sites of this sublattice). In the case of rhombohedral ordering, Li atoms and vacancies □ are randomly distributed over the sites of a unified lithium sublattice; therefore, the site distribution function in the basic cubic lattice of the unified Li sublattice can be written as follows:

$$n^{(Li,\,\square)}(x_I, y_I, z_I) = (1-x)/2 + (\eta_9^{(M)}/2)\cos[\pi(x_I - y_I + z_I)]. \quad (2)$$

The distribution function (2) takes two values on the sites of the metal fcc sublattice: $n_{Li}^{(Li)} = (1-x)/2 + \eta_9^{(M)}/2$ and $n_{Ni}^{(Li)} = (1-x)/2 + \eta_9^{(M)}/2$.

The completely ordered state of lithium nickelite is attained for the stoichiometric $LiNiO_2$ composition when the long-range order parameter $\eta_9^{(M)}(x) = 1$ and the relative concentrations of lithium and nickel atoms in the metal sublattice are equal, while the structural vacancies are absent; i.e., $x_{st} = 0$ and $z_{st} = 0$.

In the metal sublattice of the completely ordered rhombohedral ($R\bar{3}m$ space group) $LiNiO_2$ structure, the hexagonal atomic $[1\bar{1}1]_{B1}$ planes, whose sites are occupied by lithium atoms, and the $(1\bar{1}1)_{B1}$ planes, whose sites are occupied by nickel atoms, consecutively alternate in the $(1\bar{1}1)_{B1}$ direction.

The formation of the rhombohedral (trigonal) ordered $LiNiO_2$ phase is associated with the Lifshitz $\{\mathbf{k}_9\}$ star, which satisfies the Landau criterion for the second-order transition. Thus, the ordering of $Li_{1-x-z}Ni_{1+x}O_2$ nickelite with the formation of the rhombohedral ($R\bar{3}m$ space group) superstructure of the $LiNiO_2$ type can proceed through the second-order phase-transition mechanism. The rotational and translational reductions of symmetry upon the formation of the rhombohedral $LiNiO_2$ phase are equal to 4 and 3/2, respectively; the overall reduction of symmetry equals 6.

From the results obtained, it follows that the structure of rhombohedral lithium nickelite is described by only one long-range order parameter $\eta_9^{(M)}$, though some authors (see, for example, [7]) believe that two parameters are required to describe order in this phase; one is necessary for the description of order in the lithium sublattice and the other is necessary for the description of order in the nickel sublattice. However, long-range order in these sublattices is completely determined by the parameter $\eta_9^{(M)}$. In fact, using the parameter $\eta_9^{(M)}$ and the found values of the distribution function, one can obtain expressions for the estimations of the degree of order in the Li and Ni sublattices. In the general case, the degree of order in the Ni sublattice equals $\eta_{Ni} = (c_{Ni}^{(Ni)} - c_{Ni}^{(Li)})/c_{Ni}^{(Ni)max} \equiv (n_{Ni}^{(Ni)} - n_{Ni}^{(Li)})/c_{Ni}^{(Ni)max}$. The highest possible concentration of nickel in the Ni sublattice is $c_{Ni}^{(Ni)max} = 1$. With regard to this equality and the values of $n_{Ni}^{(Ni)}$ and $n_{Ni}^{(Li)}$ given by distribution functions (1) and (2), the degree of order in the nickel sublattice is

$$\eta_{Ni} = \eta_9^{(M)} + x. \quad (3)$$

Similarly, the degree of order in the Li sublattice is defined as $\eta_{Li} = (c_{Li}^{(Li)} - c_{Li}^{(Ni)})/c_{Li}^{(Li)max}$, where $c_{Li}^{(Li)} \equiv n_{Li}^{(Li)}$ and $c_{Li}^{(Ni)} \equiv n_{Li}^{(Ni)}$ are the concentrations of Li and Ni atoms in the lithium sublattice, respectively, or, which is the same, in the lithium layers. The value $c_{Li}^{(Li)max} = (1-x)$ is the highest possible concentration of lithium in the Li sublattice. With regard to the found values of $n_{Li}^{(Ni)}$ and $n_{Li}^{(Li)}$ for functions (1) and (2), one obtains

$$\eta_{Li} = \frac{\eta_9^{(M)} - x}{1-x}. \quad (4)$$

The dependence of the maximum value of the long-range order parameter $\eta_9^{(M)}$ on the composition of $Li_{1-x-z}Ni_{1+x}O_2$ lithium nickelite upon the formation of the rhombohedral $LiNiO_2$ superstructure has the form for values $0 \le x \le 1$, $0 \le z < (1-x)$

$$\eta_9^{(M)max}(x, z) = 1 - x. \quad (5)$$

With regard to Eq. (5), $\eta_{Li}^{max} = (1-2x)/(1-x)$ and $\eta_{Ni}^{max} = 1$. For the maximal long-range order in

$Li_{1-x-z}Ni_{1+x}O_2$, when $x = 0$ and $z = 0$, the degree of order in the nickel and lithium sublattices is 1. At $x > 0$, the degree of order in the Ni sublattice is still equal to unity, because all its sites are occupied by only Ni atoms, and the degree of order in the Li sublattice is no higher than $\eta_{Li}^{max} = (1-2x)/(1-x)$, because not only Li atoms but also xN_A Ni atoms are located at its sites. The degree of order cannot be negative; therefore, it follows from the equation for η_{Li}^{max} that the rhombohedral structure ($R\bar{3}m$ space group) cannot exist at $x > 0.5$. Actually, at a high concentration of vacancies ($z \geq 1/6$), disordering must proceed to the cubic phase, or the symmetry must be reduced with the retention of nickel atomic planes and with ordering of Li atoms and vacancies in the $(1\bar{1}1)_{B1}$ planes relating to the unified lithium sublattice. In lithium nickelite with a high excess of Ni ($x \geq 1/6$), a variant of the symmetry reduction can take place with the redistribution of Li and Ni atoms over all $(1\bar{1}1)_{B1}$ planes of the metal sublattice and their ordering in these planes. Such orderings can proceed as first-order phase transitions through the transition channels involving the $\{\mathbf{k}_4\}$ and $\{\mathbf{k}_3\}$ star rays, in addition to the $\{\mathbf{k}_9\}$ star rays. As a result, superstructures of the $Li_5\square Ni_6O_{12}$ or $(Li_5Ni)_6O_{12}$ types with the monoclinic and trigonal symmetries can arise. At an even higher concentration of vacancies $z \geq 0.25$, superstructures of the $Li_3\square Ni_4O_8$ or $Li_2\square Ni_3O_6$ types can arise. Actually, the monoclinic $Li_3\square Ni_4O_8$ superstructure was detected in $Li_{0.50-0.75}NiO_2$ nickelite by X-ray and electron diffraction [2, 16].

All the superstructures that are formed on the basis of the rhombohedral phase retain the alternation of the $(1\bar{1}1)_{B1}$ planes, whose sites are occupied by only Ni atoms or only Li atoms and by structural vacancies; the alternation of planes is determined by the superstructure vector $\mathbf{k}_9^{(3)}$, which is characterized by the long-range order parameter $\eta_9^{(M)}$ in the metal fcc sublattice. The distribution of Ni atoms over the sites of the metal fcc sublattice is described by Eq. (1), as in the rhombohedral structure, and the dependence $\eta_9^{(M)max}(x, z)$ for all superstructures is described by Eq. (5). Lithium atoms and vacancies in the $(1\bar{1}1)_{B1}$ planes are arranged in the ordered way; i.e., the unified lithium sublattice in the rhombohedral phase is divided into two nonequivalent sublattices containing only lithium atoms and only vacancies, respectively. In these superstructures, the fraction of Li atoms among the lithium atoms and vacancies is $(1-x-z)/(1-x)$; therefore, the first term in the corresponding distribution functions of

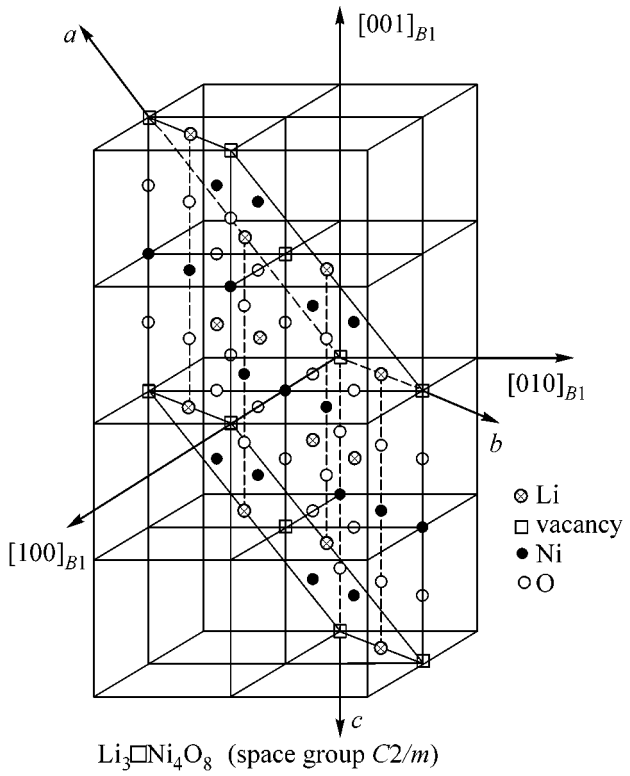

Fig. 2. Perfect monoclinic ($C2/m$ space group) unit cell of ordered $Li_3\square Ni_4O_8$ nickelite in the lattice with the $B1$ structure.

Li atoms, which corresponds to the concentration wave with the wave vector $\mathbf{k}_9^{(3)}$, will be

$$[(1-x-z)/(1-x)]n^{(Li,\square)}(x_I, y_I, z_I) \equiv (1-x-z)/2 + (1-x-z)\eta_9^{(M)}/[2(1-x)]\cos[\pi(x_I - y_I + z_I)].$$

The unit cell of the perfect monoclinic ordered $Li_3\square Ni_4O_8$ phase ($C2/m(C_{2h}^3)$ space group) has the translation vectors $\mathbf{a}_m = \langle 1\bar{1}2\rangle_{B1}$, $\mathbf{b}_m = \langle 110\rangle_{B1}$, and $\mathbf{c}_m = \langle 00\bar{2}\rangle_{B1}$ (Fig. 2). The unit cell contains 6 Li atoms in the 2*b* (0 1/2 0) and 4*f* (1/4 1/4 1/2) positions; 2 structural vacancies in the 2*a* (0 0 0) position; 8 Ni atoms in the 2*c* (0 0 1/2), 2*d* (0 1/2 1/2), and 4*e* (1/4 1/4 0) positions; and 16 O atoms in the 4*i* (0 0 1/4), 4*i* (1/2 0 1/4), and 8*j* (1/4 3/4 3/4) positions (without regard for displacements). The symmetry analysis performed has shown that the distribution of Li atoms and vacancies □ depends on three superstructure vectors $\mathbf{k}_9^{(1)}$, $\mathbf{k}_9^{(2)}$, and $\mathbf{k}_9^{(4)}$, which are characterized by the long-range order parameter $\eta_9^{(Li)}$. The calculated distribution function of lithium atoms in the monoclinic ($C2/m$ space group)

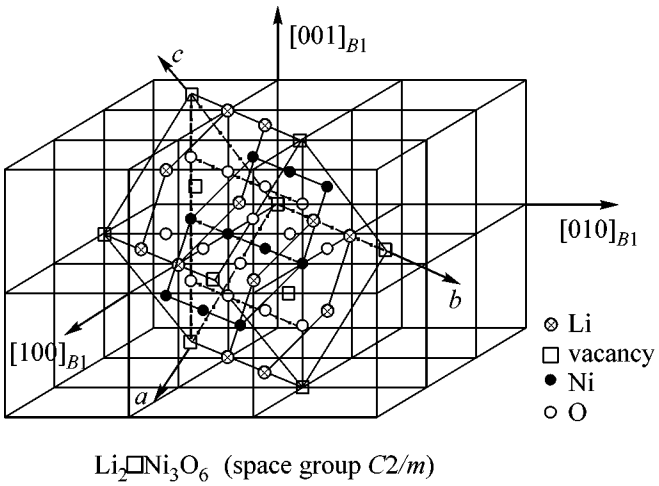

Fig. 3. Position of the monoclinic (*C*2/*m* space group) unit cell of the ordered $Li_2□Ni_3O_6$ phase in the lattice with the *B*1 structure.

ordered $Li_3□Ni_4O_8$ phase of $Li_{1-x-z}Ni_{1+x}O_2$ nickelite has the form

$$n^{(\mathrm{Li})}(x_\mathrm{I}, y_\mathrm{I}, z_\mathrm{I}) = (1-x-z)/2 + (1-x-z)\eta_9^{(\mathrm{M})}/[2(1-x)]\cos[\pi(x_\mathrm{I}-y_\mathrm{I}+z_\mathrm{I})] - \eta_9^{(\mathrm{Li})}/4)\{\cos[\pi(x_\mathrm{I}+y_\mathrm{I}+z_\mathrm{I})] + \cos[\pi(-x_\mathrm{I}+y_\mathrm{I}+z_\mathrm{I})] + \cos[\pi(x_\mathrm{I}+y_\mathrm{I}-z_\mathrm{I})] \quad (6)$$

and depends on two long-range order parameters $\eta_9^{(\mathrm{M})}$ and $\eta_9^{(\mathrm{Li})}$. At the 2*b* and 4*f* sites of the Li sublattice, the function given by Eq. (6) is $n_{\mathrm{Li}}^{(\mathrm{Li})} = (1-x-z)/2 + (1-x-z)\eta_9^{(\mathrm{M})}/[2(1-x)] + \eta_9^{(\mathrm{Li})}/4$. At the 2*a* sites of the vacancy sublattice, it equals $n_{□}^{(\mathrm{Li})} = (1-x-z)/2 + (1-x-z)\eta_9^{(\mathrm{M})}/[2(1-x)] - 3\eta_9^{(\mathrm{Li})}/4$.

The dependence of the maximum value of the long-range order parameter $\eta_9^{(\mathrm{Li})}$ on the composition of $Li_{1-x-z}Ni_{1+x}O_2$ lithium nickelite upon the formation of the monoclinic (*C*2/*m* space group) $Li_3□Ni_4O_8$ superstructure has the form

$$\eta_9^{(\mathrm{Li})\max}(x, z) = \begin{cases} 4(x+z), \text{ if } (x+z) \le 1/4 \\ 4(1-x-z)/3, \text{ if } (x+z) > 1/4 \end{cases} \quad (7)$$

for values $x \ge 0$ and $z \ge 0$.

The authors of [3] assumed that, as the concentration of structural vacancies in $Li_{1-x-z}Ni_{1+x}O_2$ lithium nickelite increases from $z = 1/4$ to $z = 1/2$, the structure of the ordered phase remains unchanged and only the degree of occupation of the 2*b* positions by lithium atoms decreases from 1 to 0. This is improbable because, as a rule, the variation of the relative concentration of structural vacancies Δz within the homogeneity regions of ordered phases of nonstoichiometric compounds does not exceed 0.1 [10, 11]. This assumption also contradicts the experimental data [2]: electron diffraction patterns obtained for $Li_{1-x-z}Ni_{1+x}O_2$ of different composition ($x = 0$, $0.35 \le z \le 0.75$) are noticeably different.

If the concentration of structural vacancies in $Li_{1-x-z}Ni_{1+x}O_2$ reaches $z \approx 1/3$, the formation of the ordered $Li_2□Ni_3O_6$ phase is most probable. This phase is also monoclinic and belongs to the *C*2/*m* (C_{2h}^3) space group but has a different unit cell with the translation vectors $\mathbf{a}_m = \frac{1}{2}\langle 1\bar{1}\bar{2}\rangle_{B1}$, $\mathbf{b}_m = \frac{3}{2}\langle 110\rangle_{B1}$, and $\mathbf{c}_m = \frac{1}{2}\langle 1\bar{1}2\rangle_{B1}$ (Fig. 3). The unit cell contains 4 Li atoms in the 4*g* (0 1/3 0) position, 2 structural vacancies in the 2*a* (0 0 0) position, 6 Ni atoms in the 2*d* (0 1/2 1/2) and 4*h* (0 1/6 1/2) positions, and 12 O atoms in the 4*i* (1/4 0 3/4) and 8*j* (1/4 2/3 3/4) positions. Because the $Li_2□Ni_3O_6$, like the previous $Li_3□Ni_4O_8$, arises on the basis of the rhombohedral phase, the transition channel retains the superstructure vector $\mathbf{k}_9^{(3)}$, which determines the alternation of the $(1\bar{1}1)_{B1}$ planes, whose sites are occupied by only Ni atoms or only Li atoms and structural vacancies. This vector is characterized by the long-range order parameter $\eta_9^{(\mathrm{M})}$. The distribution of lithium atoms and vacancies in the $(1\bar{1}1)_{B1}$ planes of the phase under consideration is determined by the superstructure vectors $\mathbf{k}_4^{(1)}$ and $\mathbf{k}_4^{(2)}$, which are characterized by the long-range order parameter $\eta_4^{(\mathrm{Li})}$. The calculated distribution function of lithium atoms in the ordered $Li_2□Ni_3O_6$ phase of $Li_{1-x-z}Ni_{1+x}O_2$ lithium nickelite has the form

$$n^{(\mathrm{Li})}(x_\mathrm{I}, y_\mathrm{I}, z_\mathrm{I}) = (1-x-z)/2 + (1-x-z)\eta_9^{(\mathrm{M})}/[2(1-x)]\cos[\pi(x_\mathrm{I}-y_\mathrm{I}+z_\mathrm{I})] - (2\eta_4^{(\mathrm{Li})}/3)\cos[4\pi(x_\mathrm{I}+y_\mathrm{I})/3]. \quad (8)$$

The function given by Eq. (8) depends on two order parameters $\eta_9^{(\mathrm{M})}$ and $\eta_9^{(\mathrm{Li})}$. At the 4*g* sites of the lithium sublattice, it takes the value $n_{\mathrm{Li}}^{(\mathrm{Li})} = (1-x-z)/2 + (1-x-z)\eta_9^{(\mathrm{M})}/[2(1-x)] + \eta_4^{(\mathrm{Li})}/3$. At the 2*a* sites of the vacancy sublattice, it equals $n_{□}^{(\mathrm{Li})} = (1-x-z)/2 + (1-x-z)\eta_9^{(\mathrm{M})}/[2(1-x)] - 2\eta_4^{(\mathrm{Li})}/3$.

The dependence of the maximum value of the long-range order parameter $\eta_4^{(\mathrm{Li})}$ on the composition of $Li_{1-x-z}Ni_{1+x}O_2$ lithium nickelite upon the forma-

tion of the monoclinic ($C2/m$ space group) $Li_2\square Ni_3O_6$ superstructure in lithium nickelite has the form for $x \geq 0$ and $z \geq 0$

$$\eta_4^{(\mathrm{Li})\max}(x, z) = \begin{cases} 3(x+z), \text{ if } (x+z) \leq 1/3 \\ 3(1-x-z)/2, \text{ if } (x+z) > 1/3 \end{cases}. \quad (9)$$

The monoclinic ordered $Li_2\square Ni_3O_6$ phase can have a twice as large unit cell that corresponds to the $C2$ space group and has the translation vectors $\mathbf{a}_m = \frac{1}{2}\langle 1\bar{1}\bar{2}\rangle_{B1}$, $\mathbf{b}_m = \frac{3}{2}\langle 110\rangle_{B1}$, and $\mathbf{c}_m = \langle 1\bar{1}2\rangle_{B1}$ (Fig. 4). The unit cell contains 8 Li atoms in the 2*a* (0 1/3 0), 2*a* (0 2/3 0), 2*b* (0 0 1/2), and 2*b* (0 2/3 1/2) positions; 4 structural vacancies in the 2*a* (0 0 0) and 2*b* (0 1/3 1/2) positions; 12 Ni atoms in the 4*c* (0 1/6 1/4), (0 1/2 1/4), and (0 5/6 1/4) positions; and 24 O atoms in the 4*c* positions. In addition to the vector $\mathbf{k}_9^{(3)}$, the transition channel involves the superstructure vectors $\mathbf{k}_4^{(1)}$, $\mathbf{k}_4^{(2)}$, $\mathbf{k}_3^{(3)}$, $\mathbf{k}_3^{(4)}$, $\mathbf{k}_0^{(4)}$, $\mathbf{k}_0^{(28)}$, $\mathbf{k}_0^{(13)}$, and $\mathbf{k}_0^{(37)}$ of the $\{\mathbf{k}_4\}$, $\{\mathbf{k}_3\}$, and $\{\mathbf{k}_0\}$ stars. The distribution of lithium atoms and vacancies in the $(1\bar{1}1)_{B1}$ planes of the phase under discussion is determined by the superstructure vectors of the $\{\mathbf{k}_4\}$, $\{\mathbf{k}_3\}$, and $\{\mathbf{k}_0\}$ stars, which are characterized by the long-range order parameters $\eta_4^{(\mathrm{Li})}$, $\eta_3^{(\mathrm{Li})}$, and $\eta_0^{(\mathrm{Li})}$. The calculated distribution function of lithium atoms in the monoclinic ($C2$ space group) ordered $Li_2\square Ni_3O_6$ phase of $Li_{1-x-z}Ni_{1+x}O_2$ nickelite has the form

$$\begin{aligned} n^{(\mathrm{Li})}(x_\mathrm{I}, y_\mathrm{I}, z_\mathrm{I}) &= (1-x-z)/2 \\ &+ (1-x-z)\eta_9^{(\mathrm{M})}/[2(1-x)]\cos[\pi(x_\mathrm{I}-y_\mathrm{I}+z_\mathrm{I})] \\ &-(\eta_4^{(\mathrm{Li})}/12)\{\cos[4\pi(x_\mathrm{I}+y_\mathrm{I})/3]-(\sqrt{3})\sin[4\pi(x_\mathrm{I}+y_\mathrm{I})/3]\} \\ &-(\eta_3^{(\mathrm{Li})}/12)\{\cos[\pi(x_\mathrm{I}-5y_\mathrm{I}-3z_\mathrm{I})/3] \\ &-(\sqrt{3})\sin[\pi(x_\mathrm{I}-5y_\mathrm{I}-3z_\mathrm{I})/3]\} \\ &-(\eta_0^{(\mathrm{Li})}/2)\{\cos[\pi(x_\mathrm{I}+7y_\mathrm{I}+9z_\mathrm{I})/6] \\ &-(\sqrt{3})\sin[\pi(x_\mathrm{I}+7y_\mathrm{I}+9z_\mathrm{I})/6]\} \end{aligned} \quad (10)$$

and depends on four long-range order parameters. The function given by Eq. (10) takes five different values (see, for example, the analogous function for the $M_6X_5\square$ superstructure [15]). In the case of equal order parameters, $\eta_4^{(\mathrm{Li})} = \eta_3^{(\mathrm{Li})} = \eta_0^{(\mathrm{Li})} = \eta^{(\mathrm{Li})}$, these values degenerate into two values: $\eta_{\mathrm{Li}}^{(\mathrm{Li})} = (1-x-z)/2 + (1-x-z)\eta_9^{(\mathrm{M})}/[2(1-x)] + \eta^{(\mathrm{Li})}/3$ at the sites of the lithium sublattice and $n_\square^{(\mathrm{Li})} = (1-x-z)/2 + (1-x-z)\eta_9^{(\mathrm{M})}/[2(1-x)] - 2\eta^{(\mathrm{Li})}/3$ at the sites of the vacancy sublattice.

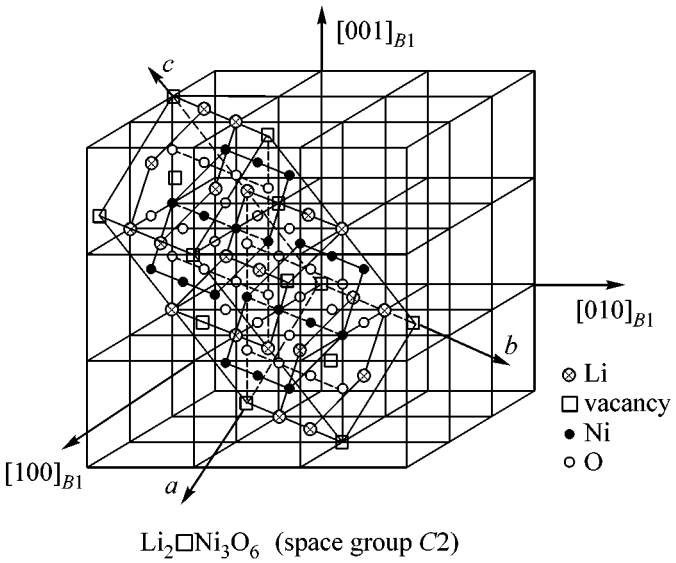

Fig. 4. Position of the monoclinic ($C2$ space group) unit cell of the ordered $Li_2\square Ni_3O_6$ nickelite in the lattice with the $B1$ structure.

The dependence of the maximum value of the long-range order parameter $\eta^{(\mathrm{Li})}$ on the composition of $Li_{1-x-z}Ni_{1+x}O_2$ upon the formation of the monoclinic ($C2$ space group) ordered $Li_2\square Ni_3O_6$ phase in lithium nickelite has the form for $x \geq 0$ and $z \geq 0$

$$\eta^{(\mathrm{Li})\max}(x, z) = \begin{cases} 3(x+z), \text{ if } (x+z) \leq 1/3 \\ 3(1-x-z)/2, \text{ if } (x+z) > 1/3 \end{cases}. \quad (11)$$

The presence of non-Lifshitz star rays in the order–disorder transition channels associated with the formation of monoclinic superstructures signifies that these superstructures are formed through the first-order phase-transition mechanism, i.e., with a stepwise change in the period a_{B1} of the basic cubic lattice. The diffraction patterns of the monoclinic superstructures will differ in both the position and intensity of superstructure reflections; however, structural neutron diffraction analysis should be used along with X-ray and electron diffractions to provide an accurate determination of the structure of ordered phases.

This work was supported by the Russian Foundation for Basic Research, project no. 03-03-32031a.

REFERENCES

1. C. Delmas, in *Industrial Chemistry Library. 5. Lithium Batteries. New Materials, Developments and Perspectives*, Ed. by G. Pistoia (Elsevier, Amsterdam, 1993), p. 457.
2. C. Delmas, M. Ménétrier, L. Croguennec, *et al.*, Int. J. Inorg. Mater. **1**, 11 (1999).
3. J. P. Peres, F. Weil, and C. Delmas, Solid State Ionics **116**, 19 (1999).

4. M. E. Arroyo y de Dompabio and G. Ceder, J. Power Sources **119–121**, 654 (2003).
5. H. Arai, S. Okada, H. Ohtsuka, *et al.*, Solid State Ionics **80**, 261 (1995).
6. W. Li, J. N. Reimers, and J. R. Dahn, Phys. Rev. B **46**, 3236 (1992).
7. I. J. Pickering and J. T. Lewandowski, Solid State Ionics **53–56**, 405 (1992).
8. J. N. Reimers, W. Li, and J. R. Dahn, Phys. Rev. B **47**, 8486 (1993).
9. A. I. Gusev and A. A. Rempel', *Structural Phase Transitions in Nonstoichiometric Compounds* (Nauka, Moscow, 1988).
10. A. I. Gusev and A. A. Rempel', *Nonstoichiometry, Disorder, and Order in Solids* (Ural. Otd. Ross. Akad. Nauk, Yekaterinburg, 2001).
11. A. I. Gusev, A. A. Rempel, and A. J. Magerl, *Disorder and Order in Strongly Nonstoichiometric Compounds: Transition Metal Carbides, Nitrides and Oxides* (Springer, Berlin, 2001).
12. O. V. Kovalev, *Irreducible Representations of the Space Groups* (Naukova Dumka, Kiev, 1961; Gordon and Breach, New York, 1965).
13. O. V. Kovalev, *Representations of the Crystallographic Space Groups: Irreducible Representations, Induced Representations, and Corepresentations* (Nauka, Moscow, 1986; Gordon and Breach, Yverdon, Switzerland, 1993).
14. A. G. Khachaturyan, *The Theory of Phase Transformations and the Structure of Solids Solutions* (Nauka, Moscow, 1974).
15. A. I. Gusev and A. A. Rempel, Phys. Status Solidi A **135**, 15 (1993).
16. J. P. Peres, A. Demourgues, and C. Delmas, Solid State Ionics **111**, 135 (1998).

Translated by A. Bagatur'yants

JETP Letters, Vol. 79, No. 4, 2004, pp. 155–159. Translated from Pis'ma v Zhurnal Éksperimental'noĭ i Teoreticheskoĭ Fiziki, Vol. 79, No. 4, 2004, pp. 190–194.

Magnetization-Induced Third Harmonic Generation in Magnetic Nanogranular Films: Correlation with Giant Magnetoresistance

T. V. Murzina[1, *], E. M. Kim[1], S. E. Matskevich[1], O. A. Aktsipetrov[1], A. F. Kravets[2], and A. Y. Vovk[2]

[1] *Faculty of Physics, Moscow State University, Vorob'evy gory, Moscow, 119992 Russia*
**e-mail: mur@shg.ru*

[2] *Institute of Magnetism, National Academy of Sciences of Ukraine, Kiev, 03680 Ukraine*

Received November 24, 2003; in final form, January 8, 2004

Magnetization-induced third harmonic (TH) generation was observed in magnetic nanostructures—nanogranular Co_xAg_{1-x} films—possessing giant magnetoresistance (GMR). The magnetization-induced contribution to the TH intensity was studied as a function of the concentration of a magnetic component (cobalt) in the films. Magnetic contrast of the TH intensity was found to correlate with the GMR coefficient: both parameters simultaneously reach extremum in the range of cobalt concentrations $x \sim 0.3$–0.35. © *2004 MAIK "Nauka/Interperiodica".*

PACS numbers: 42.65.Ky; 75.70.Ak; 75.75.+a; 75.47.De

Magnetic nanostructures have attracted attention over the last two decades as structures exhibiting unusual magnetic and magnetooptical effects, such as oscillation of exchange interaction between magnetic layers separated by a nonmagnetic spacer [1], spin-dependent scattering and tunneling [2, 3], giant magnetoresistance (GMR) [4], giant nonlinear magnetooptical Kerr (GMK) effect in the second harmonic (SH) generation [5], etc. The latter two effects were observed in the multilayer magnetic structures and in magnetic nanogranulated alloys consisting of nonmagnetic (dielectric or metallic) matrices and magnetic nanoparticles distributed in their bulk [6].

The transport properties (including GMR) of such magnetic nanostructures are largely governed by the structure of internal interfaces between the multilayers (nanoparticles) and by the matrix material [7]. At the same time, the nonlinear optical effects and, primarily, the SH generation, which is forbidden in the bulk of centrosymmetric media (including metals) in the electric-dipole approximation, are distinguished by a high sensitivity to the interface properties. In this case, the surfaces and internal interfaces, for which the inversion center is absent, are the SH sources [8].

In magnetic media, the quadratic susceptibility tensor acquires additional (magnetization-induced) components, because the time-reversal symmetry is broken due to the magnetization, while the spatial inversion symmetry is broken at the surfaces and interfaces as a result of structural disturbance, giving rise to the surface (interfacial) magnetization-induced SH. Due to the unique sensitivity of the magnetization-induced SH to the magnetism of low-dimensional systems, its generation is used for studying the magnetic properties of surfaces and thin films of ferromagnets, magnetic superlattices, and nanoparticles [9]. In the study of the SH generation in magnetic nanogranular films, the intensive nonlinear optical magnetic Kerr effect was observed, for which the dependence of magnetic contrast of the magnetization-induced SH intensity on the film concentrational composition qualitatively coincided with the analogous dependence of the GMR coefficient [10].

Up to now, all nonlinear magneto-optics was practically concentrated on the study of the magnetization-induced SH, while the fact that the third harmonic (TH) generation in magnetic nanostructures can also be informative was disregarded, and the magnetization-induced TH generation was not observed in magnetic nanostructures.

In this work, the magnetization-induced TH generation was observed in magnetic nanogranular films possessing GMR. The magnetic contrast of the TH intensity was found to correlate with the GMR coefficient as a function of the concentration of the magnetic component in nanogranular Co_xAg_{1-x} films. A comparison with a similar effect in the magnetization-induced SH generation was also carried out.

Samples of nanogranular Co_xAg_{1-x} films with a Co atomic fraction of $0.04 < x < 0.9$ were prepared by the separate electron-beam coevaporation of Co and Ag from two sources in a high vacuum (10^{-4} Pa) and condensation of a mixed metal vapor onto glass-ceramic substrates at room temperature. Film thicknesses were about 200 nm. Film composition was determined by the

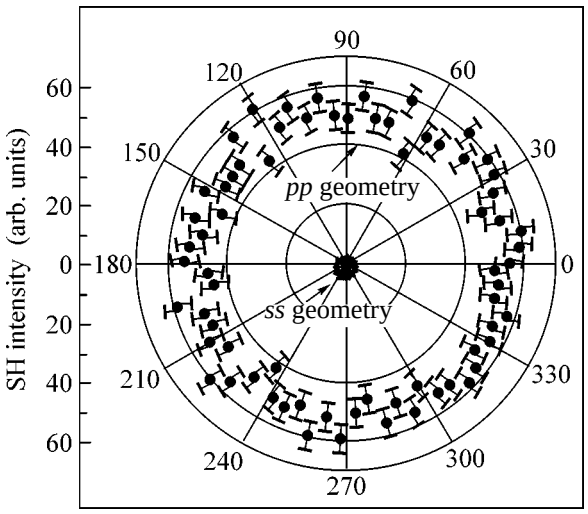

Fig. 1. Azimuthal dependences of the SH intensity for the *pp*- and *ss*-polarization combinations; $Co_{0.4}Ag_{0.6}$ film.

EDXA method. The crystal structure of films was determined by X-ray diffraction. To estimate the sizes of magnetic grains, the SQUID magnetometry data and the magnetization curves were analyzed by the method described in [2]. Film magnetoresistance was measured by the four-probe method at room temperature in a magnetic field up to 8 kOe.

Analysis showed that, at $x < 0.5$, the average size of Co grains in the granulated films was 3 Å. In the domain of existence of the granulated structure ($x < 0.5$), the Co grains in the Co_xAg_{1-x} films are characterized by an fcc (111) structure which coherently matches with the fcc structure of the Ag matrix.

The magnetization-induced TH generation was observed upon the irradiation of film surfaces by an YAG:Nd^{3+} laser with a wavelength of 1064 nm, a pulse intensity of 10 MW/cm^2, a pulse duration of 15 ns, and a pulse repetition rate of 25 Hz. The TH radiation reflected from the granular films was separated by the appropriately chosen filters and detected using a photomultiplier and a gated electronic recording system. In a similar manner, the magnetization-induced SH was studied in the same films. A magnetic field of about 2 kOe was produced by permanent magnets and oriented in the film planes.

Figure 1 presents the azimuthal angular dependences of SH intensity for the $Co_{0.4}Ag_{0.6}$ sample in the case of *pp*- and *ss*-polarization combinations, where the first index stands for the polarization of SH radiation and the second indicates the polarization of fundamental radiation. Similar dependences were obtained for all the studied Co_xAg_{1-x} samples. The isotropic character of these dependences is, primarily, evidence of the absence of anisotropy for the properties in the film plane, allowing these films to be considered isotropic as regards the magnetization-induced nonlinear optical effects. Moreover, the presence of a nonzero isotropic *ss* SH-intensity component violates so-called *ss* forbidding [11] that is likely caused by the granular character of film structure and is an indication of the second-order hyper-Rayleigh scattering, i.e., appearance of an incoherent diffuse SH component [12].

Let us consider what kind of magnetization-induced effects can be observed for the second and third harmonics in an isotropic magnetic film. The nonlinear polarization can be written in the form

$$P(2\omega, 3\omega) = \chi^{(2)}_{ijk}(M) : E_jE_k + \chi^{(3)}_{ijkl}(M) : E_jE_kE_l, \quad (1)$$

where $\chi^{(2)}$ and $\chi^{(3)}$ are, respectively, the quadratic and cubic susceptibility tensors determining the SH and TH generation processes and, in the general case, are functions of the medium magnetization M; and E_j is the jth component of the fundamental field. A consistent consideration of the form of material tensors of different rank was carried out in [13] for magnetized media belonging to each of the point symmetry groups. According to the approach developed in [14] for the description of the magnetization-induced effects in SH, the quadratic susceptibility tensor of a magnetized medium can be represented as the sum of the magnetization-even and magnetization-odd components, $\chi^{(2)}_{ijk}(M) = \chi^{(2,\,\mathrm{even})}_{ijk} \pm \chi^{(2,\,\mathrm{odd})}_{ijk}(M)$, the first of which is invariant about the magnetization inversion, while the second changes its sign upon changing M direction. Similarly, in the case of TH generation, the cubic susceptibility tensor can be written as $\chi^{(3)}_{ijkl}(M) = \chi^{(3,\,\mathrm{even})}_{ijkl} \pm \chi^{(3,\,\mathrm{odd})}_{ijkl}(M)$.

The nonzero components of tensors $\chi^{(2)}$ and $\chi^{(3)}$ are presented in the table. The coordinate system is chosen

Magnetization-even $\chi^{(\mathrm{even})}$ and magnetization-odd $\chi^{(\mathrm{odd})}$ quadratic and cubic susceptibility components; the odd components are calculated for the geometries of equatorial ($M \parallel Y$) and meridional ($M \parallel X$) magnetooptical Kerr effect

	$\chi^{(\mathrm{even})}$ ($M = 0$)	$\chi^{(\mathrm{odd})}$ ($M \parallel Y$)	$\chi^{(\mathrm{odd})}$ ($M \parallel X$)
SH	$\chi^{(2)}_{zzz}, \chi^{(2)}_{zxx} = \chi^{(2)}_{zyy}, \chi^{(2)}_{xxz} = \chi^{(2)}_{yyz}$	$\chi^{(2),M}_{xyy}$, $\chi^{(2),M}_{xxx}$, $\chi^{(2),M}_{yyx}$, $\chi^{(2),M}_{xzz}$, $\chi^{(2),M}_{zzx}$	$\chi^{(2),M}_{yyy}$, $\chi^{(2),M}_{yxx}$, $\chi^{(2),M}_{yzz}$
TH	$\chi^{(3)}_{zzzz}, \chi^{(3)}_{xxxx} = \chi^{(3)}_{yyyy}, \chi^{(3)}_{zzxx} = \chi^{(3)}_{zzyy}$	$\chi^{(3),M}_{zxzz}$, $\chi^{(3),M}_{xxxz}$, $\chi^{(3),M}_{zxxx}$, $\chi^{(3),M}_{yyxx}$, $\chi^{(3),M}_{xzzz}$	$\chi^{(3),M}_{zyyy}, \chi^{(3),M}_{yxxz}$
	$\chi^{(3)}_{xxyy} = \chi^{(3)}_{yyxx}, \chi^{(3)}_{xxzz} = \chi^{(3)}_{yyzz}$		$\chi^{(3),M}_{yzzz}$

so that the *Z* axis is perpendicular to the film surface, while the (*XZ*) plane coincides with the incidence plane of the fundamental radiation (see inset in Fig. 2a). It follows from the table that, in the absence of the external magnetic field, the SH generation is possible only for the *pp* and *sp* polarization combinations, while the TH generation is possible only for the *pp* and *ss* combinations. Depending on the direction of external field, various magnetization-induced effects can be observed in the SH and TH generation. For the equatorial Kerr effect with *Y*-directed magnetic field, only the *p*-polarized magnetization-induced SH and TH components appear (table, second column). In this case, a change in the direction of the applied magnetic field brings about *M*-odd changes in the intensity of the corresponding harmonic, because the total SH/TH intensity can be represented as

$$I_{2\omega,3\omega}(M) \sim (E^{\text{even}}_{2\omega/3\omega} + E^{\text{odd}}_{2\omega/3\omega})^2 = E^{\text{even}\,2}_{2\omega/3\omega} + 2\cos(\phi)E^{\text{even}}_{2\omega/3\omega}E^{\text{odd}}_{2\omega/3\omega} + E^{\text{odd}\,2}_{2\omega/3\omega}, \quad (2)$$

where the term $E^{\text{even}}_{2\omega/3\omega}(E^{\text{odd}}_{2\omega/3\omega})$ is responsible for the even (odd) magnetic effect and ϕ is the phase difference between $E^{\text{odd}}_{2\omega,3\omega}$ and $E^{\text{even}}_{2\omega,3\omega}$ (inset in Fig. 2b). As is customary in magneto-optics, magnetic contrast

$$\rho_{2\omega,3\omega} = (I_{2\omega,3\omega}(\uparrow) - I_{2\omega,3\omega}(\downarrow))/(I_{2\omega,3\omega}(\uparrow) + I_{2\omega,3\omega}(\downarrow)) = 4E^{\text{even}}_{2\omega,3\omega}E^{\text{odd}}_{2\omega,3\omega}\cos(\phi)/(I_{2\omega,3\omega}(\uparrow) + I_{2\omega,3\omega}(\downarrow)) \quad (3)$$

serves as a measure of a magnetization-induced change in the signal intensity. In Eq. (3), $I_{2\omega,3\omega}(\uparrow)$ and $I_{2\omega,3\omega}(\downarrow)$ are, respectively, the SH (TH) intensities measured for the oppositely directed magnetic fields. Thus, both the ratio of field amplitudes of the magnetic and nonmagnetic SH (TH) and the phase relations between them prove to be essential in the measurement of magnetic contrast. For this reason, measurement of the intensive magnetic contrast was accompanied by measuring the phases of harmonic fields using SH or TH interferometry [15].

Note that there are no coinciding even and odd components among the quadratic and cubic susceptibilities. This means that, in the general case, the Fresnel and local-field factors can be different for these components, which may result in different spectral dependences of the nonmagnetic and magnetic SH- and TH-field components.

One can see in the table that, in the case of the meridional Kerr effect, the magnetization-odd *s*-polarized SH and TH components appear for the *p*-polarized fundamental radiation, resulting in the rotation of polarization planes of the SH and TH waves. The magnetization-induced angle of rotation of the SH-wave polarization plane in the $Co_{0.4}Ag_{0.6}$ film was found to be 10°–15°.

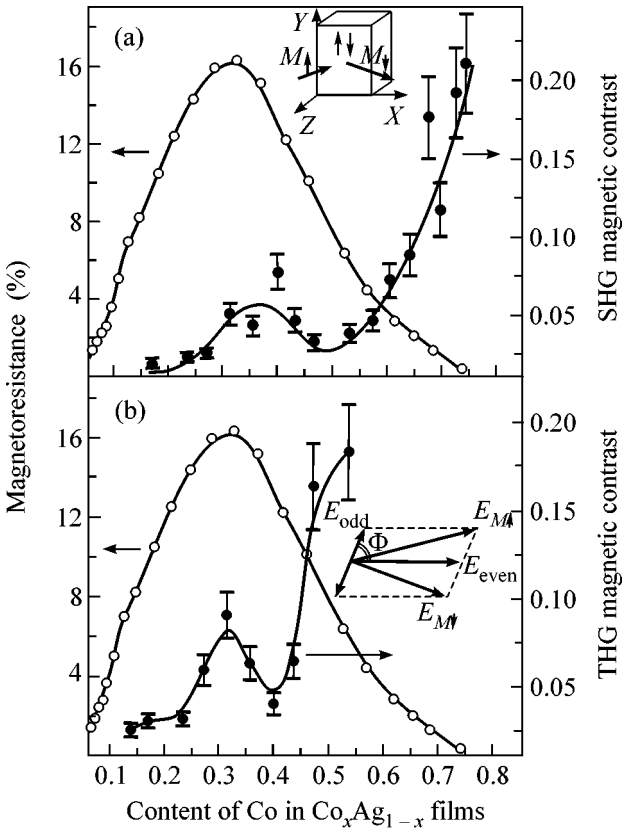

Fig. 2. Magnetoresistance and magnetic contrast of (a) SH and (b) TH intensity as functions of the concentration *x* of magnetic component in the Co_xAg_{1-x} films for the *pp*-polarization combination in the geometry of equatorial magnetic Kerr effect. Inset: (upper panel) measurement geometry for the equatorial Kerr effect and (lower panel) vector-addition diagram for the magnetization-even and magnetization-odd SH- and TH-field components.

The GMR coefficient and the magnetic contrast of the magnetization-induced SH intensity in the geometry of equatorial Kerr effect are shown in Fig. 2a as functions of cobalt concentration *x* in the Co_xAg_{1-x} films. The GMR is maximal at $x \sim 0.33$. The magnetic contrast also shows a maximum in the range $x = 0.3$–0.4 followed by increase at $x > 0.55$. Analogous dependence of magnetic contrast is presented in Fig. 2b for the TH intensity. As in the case of SH, the TH magnetic contrast has a local maximum at $x = 0.3$–0.4, which corresponds to the GMR maximum.

To take into account the phase relations between the magnetization-even and magnetization-odd contributions to SH and TH, the magnetization-induced phase shift of the SH and TH waves was measured in the geometry of equatorial Kerr effect for oppositely directed magnetic fields. The scheme of interferometry of the magnetization-induced SH and TH is shown in Fig. 3a. The dependences of the SH/TH intensity on the position of a reference SH/TH source are presented in

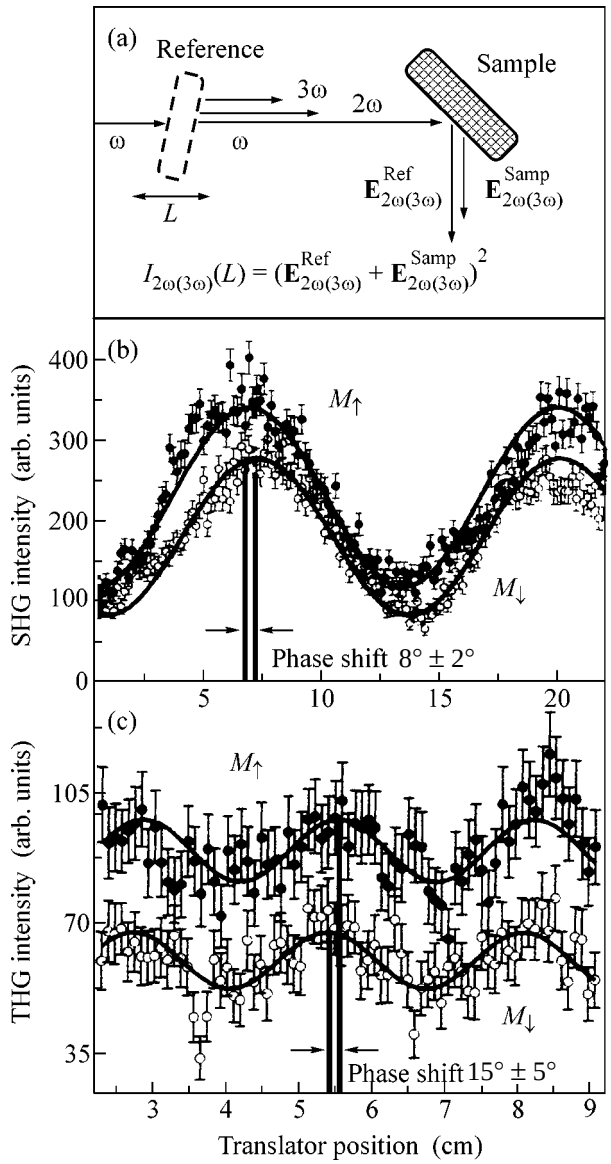

Fig. 3. (a) Measurement scheme for the interferometry of magnetization-induced SH and TH; (b, c) magnetization-induced (b) SH and (c) TH intensities as functions of the position of reference SH/TH source, as obtained by measuring interferometry of magnetization-induced SH and TH in the geometry of equatorial magnetic Kerr effect for the *pp*-polarization combination.

Figs. 3b and 3c. The periods of the interference pattern proved to be substantially different (~13 and ~3 cm) because of the difference in the dispersion of air refractive index at the SH and TH frequencies (532 and 355 nm). Since the magnetization-induced phase shift is ~10°, it can be ignored when estimating the ratio $\chi^{(\mathrm{odd})}/\chi^{(\mathrm{even})}$, so that the experimentally measured magnetic contrast reflects the ratio between the effective magnetization-even and magnetization-odd components of the nonlinear susceptibility tensor.

Thus, the magnetic contrast for the intensities of the magnetization-induced third and second optical harmonics clearly correlates with the coefficient of giant magnetoresistance. This correlation is manifested in the identical dependence of these effects on the film composition. In the case of magnetization-induced SH generation, the maximum at $x = 0.3$–0.4 is less pronounced because of a local increase in the intensity of nonmagnetic SH component in this range of x values.

Among the effects that can play an important part in the nonlinear magnetooptical Kerr effect and in its correlation with the GMR in nanogranular films, one should first of all examine the possibility of exciting local surface plasmons. As was shown in [10], the excitation of surface plasmons with optical frequencies in metallic magnetic nanoparticles surrounded by a nonmagnetic metallic matrix is possible for nanogranular systems and can lead to SH generation. In this case, one can expect that the magnetic contrast will be frequency-dependent, because the resonance properties of the magnetization-even and magnetization-odd SH/TH-field components are different, as follows from the different forms of the nonlinear susceptibility tensor components (table). At the same time, it was shown in [10] that, for different fundamental-radiation wavelengths (1064 and 800 nm), such a dependence of the magnetization-induced SH generation in the Co_xAg_{1-x} films is absent. It has also been found in this work that the magnetic contrast for the second and third harmonics depends on x qualitatively in the same way, indicating that the spectral dependence is absent for the magnetic contrast at the frequencies of recorded signal. The experimentally observed correlation between the SH/TH magnetic contrasts is likely caused by the structural features of the films near the percolation threshold and the attendant increase [16] in the nonmagnetic component of the nonlinear optical response, which has a significant effect on the magnetic contrast.

In summary, the magnetization-induced third harmonic generation has been experimentally observed in this work for nanogranular magnetic films possessing giant magnetoresistance. In the Co_xAg_{1-x} films, the magnetic effect for the TH intensity is on the same order of magnitude as (or even somewhat stronger than) the previously observed analogous effect for the magnetization-induced SH. It has been shown that, similar to the magnetization-induced SH, the GMR effect correlates with the nonlinear magnetooptical Kerr effect in the third harmonic. This correlation is manifested in the identical dependence of these effects on the film composition and in the fact that these effects reach their maxima at the same concentration of magnetic component in the nanogranular films.

This work was supported by the Presidential grant “Leading Scientific Schools of the Russian Federation” (grant no. NSh-1604.2003.2), grant from Moscow (no. 2003), and the complex program for basic research “Nanosystems, Nanomaterials, and Nanotechnology”

of the National Academy of Sciences of Ukraine within the theme "Physics of Magnetic Nanostructures with Giant Magnetoresistance Effect."

REFERENCES

1. S. S. P. Parkin, R. Bhadra, and K. P. Roche, Phys. Rev. Lett. **66**, 2152 (1991).
2. Yu. G. Pogorelov, G. N. Kakazey, J. B. Sousa, *et al.*, Phys. Rev. B **60**, 12200 (1999).
3. C. J. O'Connor, V. O. Golub, A. Ya. Vovk, *et al.*, IEEE Trans. Magn. **38**, 647 (2001).
4. M. N. Baibich, J. M. Broto, A. Fert, *et al.*, Phys. Rev. Lett. **61**, 2472 (1988).
5. H. A. Wierenga, W. de Jong, M. W. J. Prins, *et al.*, Phys. Rev. Lett. **74**, 1462 (1995).
6. A. E. Berkowitz, J. R. Mitchell, M. J. Carey, *et al.*, Phys. Rev. Lett. **68**, 3745 (1992).
7. W. Zhang and R. Yang, Phys. Lett. A **255**, 343 (1999).
8. Y. R. Shen, *The Principles of Nonlinear Optics* (Wiley, New York, 1984; Nauka, Moscow, 1989); O. A. Aktsipetrov, Colloids Surf., A **202**, 165 (2002).
9. J. Reif, J. C. Zink, C.-M. Schneider, and J. Kirschner, Phys. Rev. Lett. **67**, 2878 (1991); K. H. Bennemann, J. Magn. Magn. Mater. **200**, 679 (1999).
10. T. V. Murzina, T. V. Misuryaev, A. F. Kravets, *et al.*, Surf. Sci. **482–485**, 1101 (2001).
11. O. A. Aktsipetrov, I. M. Baranova, and Yu. A. Il'inskiĭ, Zh. Éksp. Teor. Fiz. **91**, 287 (1986) [Sov. Phys. JETP **64**, 167 (1986)].
12. T. V. Murzina, A. A. Nikulin, O. A. Aktsipetrov, *et al.*, Appl. Phys. Lett. **79**, 1309 (2001).
13. R. R. Birss, *Symmetry and Magnetism*, Vol. 3 of *Series on Selected Topics in Solid State Physics*, Ed. by E. P. Wohlfarth (North-Holland, Amsterdam, 1964).
14. Ru-Pin Pan, H. D. Wei, and Y. R. Shen, Phys. Rev. B **39**, 1229 (1989).
15. R. Stolle, G. Marowsky, E. Schwarzberg, and G. Berkovic, Appl. Phys. B **63**, 491 (1996).
16. E. Poliakov, V. M. Shalaev, V. Shubin, and V. A. Markel, Phys. Rev. B **60**, 10739 (1999).

Translated by V. Sakun

JETP Letters, Vol. 79, No. 4, 2004, pp. 160–165. Translated from Pis'ma v Zhurnal Éksperimental'noĭ i Teoreticheskoĭ Fiziki, Vol. 79, No. 4, 2004, pp. 195–200.

On the Hall Effect in a Two-Dimensional Doped Antiferromagnet

A. M. Belemuk[1], A. F. Barabanov[2], and L. A. Maksimov[2]

[1] *Vereshchagin Institute of High-Pressure Physics, Russian Academy of Sciences, Troitsk, Moscow region, 142190 Russia*

[2] *Russian Research Centre Kurchatov Institute, pl. Kurchatova 1, Moscow, 123182 Russia*

Received January 20, 2004

The conductivity and the Hall coefficient of a doped 2D antiferromagnet in the normal state are considered using the Kondo lattice model in the multimoment approximation. The anomalous temperature dependence of the kinetic coefficients is explained by the strong anisotropic charge-carrier scattering from the spin subsystem and found to be in qualitative agreement with the experimental data for the normal state of high-T_c superconductors. © *2004 MAIK "Nauka/Interperiodica".*

PACS numbers: 75.30.Mb; 74.20.Mn; 75.50.Ee

It is generally accepted that the properties of carriers in the CuO_2 planes, which are an almost ideal analogue of a doped 2D antiferromagnet, are the key to understanding the unusual kinetic properties of the normal state of high-temperature superconductors (HTSCs).

The resistivity ρ of HTSCs increases linearly with temperature over a wide range, starting almost with the superconducting transition temperature T_c, which is much lower than the Debye temperature θ_D [1–4]. In addition to the strong temperature dependence, the Hall coefficient R_H exhibits a nontrivial dependence on the doping level [1–6].

Much theoretical work has been devoted to the transport properties of HTSCs. However, the number of publications in which the temperature dependences of the resistivity and the Hall coefficient are studied simultaneously is relatively small, and in most cases, the studies are purely phenomenological. In a widely used approach based on a nearly antiferromagnetic (AFM) Fermi liquid (FL) [7], the strong anisotropy in the scattering of Fermi carriers from the spin subsystem naturally leads to the model of cold and hot spots at the Fermi surface (FS) [7–10].

In this work, the $\rho(T)$ and $R_H(T)$ dependences are also analyzed within the framework of the AFM FL model, whose spectrum corresponds to the lower spin-polaron band. It is well known that the charge dynamics of carriers in the CuO_2 planes are successfully described by the three-band Emery model [11–13]. In particular, the analysis of the elementary excitation spectrum on the basis of a spin polaron leads to the spectrum observed in the angle-resolved photoemission experiment (ARPES) over a wide doping range [14]. For example, a residual FS is observed in the undoped regime; with increasing doping level, a pseudogap opens at the FS, and a large FS with the center at (π, π) is observed in the optimal doping regime. The calculation based on the one-band Kondo model (which is simpler for theoretical analysis) qualitatively reproduces the same features.

For this reason, we will use below the model of a regular Kondo lattice for the Hamiltonian of the CuO_2 plane. The charge-carrier spectrum is determined from the calculation of the lower polaron band [14, 15], in contrast to the majority of studies, where the spectrum is chosen on the basis of FS parametrization extracted from the ARPES measurements. Another distinction is that the spin subsystem, which represents a frustrated 2D AFM, is treated in the self-consistent spherically symmetric approximation [16]. It should be noted that, in previous studies, claiming at the microscopic description of kinetic coefficients, the authors ordinarily used the phenomenological spin susceptibility corresponding to the overdamped paramagnons [7, 8]. We will determine the kinetic coefficients using a multimoment approach to the solution of the kinetic equation, which allows one to simultaneously analyze the temperature behavior of the nonequilibrium distribution functions in the problems of resistivity and Hall effect and which is alternative to the multipatch charge-carrier model [10].

The Hamiltonian of a regular square Kondo lattice has the form

$$\hat{H} = \hat{H}_0 + \hat{H}_1, \quad \hat{H}_0 = \hat{H}_h + \hat{I},$$

$$\hat{H}_h = \sum_{\mathbf{k},\sigma} \varepsilon_{\mathbf{k}} a^{\dagger}_{\mathbf{k}\sigma} a_{\mathbf{k}\sigma}, \tag{1}$$

$$\hat{I} = \frac{1}{2} I_1 \sum_{\mathbf{R},\mathbf{g}} S^{\alpha}_{\mathbf{R}+\mathbf{g}} S^{\alpha}_{\mathbf{R}} + \frac{1}{2} I_2 \sum_{\mathbf{R},\mathbf{d}} S^{\alpha}_{\mathbf{R}+\mathbf{d}} S^{\alpha}_{\mathbf{R}}.$$

0021-3640/04/7904-0160$26.00 © 2004 MAIK "Nauka/Interperiodica"

Here, $\hat{H}_h$ and $\hat{I}$ describe, respectively, the carrier (hole) motion and the subsystem of localized spins and **g** and **d** are the vectors of the first and the second nearest neighbors. The exchange Hamiltonian $\hat{I}$ is responsible for the AFM interaction between spins; p ($0 \le p \le 1$) is the frustration parameter; and $I_1 = (1-p)I$ and $I_2 = pI$ are the exchange interaction constants for the first and second nearest neighbors, respectively.

We define the hole spectrum $\varepsilon_{\mathbf{k}}$ by the harmonics with quadratic symmetry, $\gamma_g(\mathbf{k}) = (\cos(k_x) + \cos(k_y))/2$ and $\gamma_d(\mathbf{k}) = \cos(k_x)\cos(k_y)$ (Fig. 1):

$$\varepsilon_{\mathbf{k}} = \tau(a_1\gamma_g(\mathbf{k}) + a_2\gamma_g^2)(\mathbf{k}) + a_3\gamma_d(\mathbf{k}) + a_4\gamma_d^2(\mathbf{k}) + a_5\gamma_g(\mathbf{k})\gamma_d(\mathbf{k})), \quad (2)$$

$$a_1 = 1.5,\ a_2 = 3.0,\ a_3 = -1.25,\ a_4 = 0.0,\ a_5 = 0.1. \quad (3)$$

The term $\hat{H}_1$ is the sum of the on-site exchange $\hat{J}$ and the interaction $\hat{H}_f$ with an external field:

$$\hat{J} = J\frac{1}{\sqrt{N}}\sum_{\mathbf{k},\mathbf{q},\gamma_1,\gamma_2} a^{\dagger}_{\mathbf{k}+\mathbf{q},\gamma_1} S^{\alpha}_{\mathbf{q}}\hat{\sigma}^{\alpha}_{\gamma_1\gamma_2} a_{\mathbf{k}\gamma_2},$$

$$\mathbf{S}_{\mathbf{q}} = \frac{1}{\sqrt{N}}\sum_{\mathbf{q}} e^{-i\mathbf{q}\mathbf{R}}\mathbf{S}_{\mathbf{R}},$$

where $\hat{\sigma}^{\alpha}$ are the Pauli matrices (coinciding Cartesian indices α imply summation). The interaction $\hat{H}_f$ with a uniform external electric field **E** and a magnetic field **H** (perpendicular to the CuO_2 plane) is described in terms of the carrier polarization operator.

The spin subsystem is considered in a spherically symmetric approximation [16]. In this approximation, spin excitations consist of three degenerate branches defined by the two-time retarded Green's function $\langle\langle S^{\alpha}_{\mathbf{q}} | S^{\alpha}_{-\mathbf{q}}\rangle\rangle_{\omega} = A_{\mathbf{q}}/(\omega^2 - \omega^2_{\mathbf{q}})$, where numerator $A_{\mathbf{q}}$ and the spin excitation spectrum $\omega_{\mathbf{q}}$ are calculated self-consistently. The $\omega_{\mathbf{q}}$ and $A_{\mathbf{q}}$ spectra depend on the frustration parameter p and on a finite number of spin correlation functions $C_{\mathbf{r}} = \langle \mathbf{S}_{\mathbf{R}}\mathbf{S}_{\mathbf{R}+\mathbf{r}}\rangle$ and have the form

$$A_{\mathbf{q}} = -8(I_1(1-\gamma_g(\mathbf{q}))G_g + I_2(1-\gamma_d(\mathbf{q}))C_d),$$

$$\omega_{\mathbf{q}} = I\Big(\frac{8}{3}((1-\gamma_g)(B_1 + (1+\gamma_g)B_2) + (1-\gamma_g)(B_3 + (1+\gamma_d)B_4) + \gamma_g(1-\gamma_d)B_5)\Big)^{1/2}. \quad (4)$$

The spectral parameters B_i depend on temperature through $C_{\mathbf{g}}$, $C_{2\mathbf{g}}$, $C_{\mathbf{d}}$, $C_{\mathbf{g}+\mathbf{d}}$, and $C_{2\mathbf{d}}$. The functions $A_{\mathbf{q}}$ and $\omega_{\mathbf{q}}$ tend to zero as $\mathbf{q} \longrightarrow 0$. In the limit $\mathbf{q} \longrightarrow \mathbf{Q}$, the numerator $A_{\mathbf{q}}$ tends to a positive constant $A_{\mathbf{Q}}$, while the spin-wave spectrum $\omega^2_{\mathbf{q}} \approx \Delta^2 + c^2(\mathbf{q}-\mathbf{Q})^2$ is separated from zero by the gap $\Delta \equiv \omega_{\mathbf{Q}}$, which increases with temperature. As $T \longrightarrow 0$, the gap width tends to a finite limit that is determined by the frustration parameter p. It is generally accepted that p increases with the doping level n_h. Bearing in mind that we deal with a doping level close to optimal ($n_h \approx 0.15$), we choose $p = 0.1$ [14].

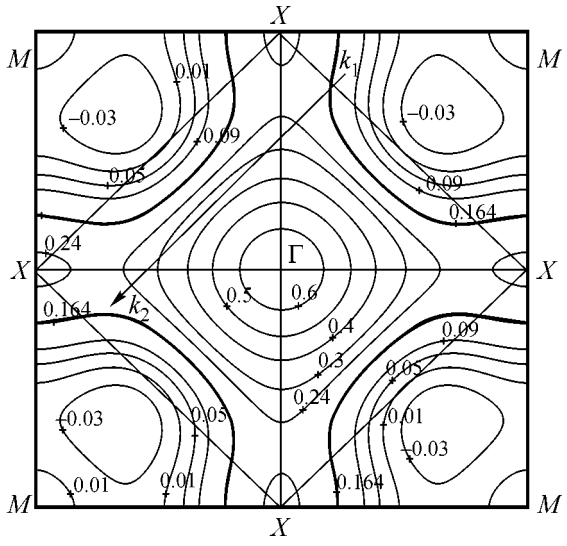

Fig. 1. The spectrum of charge carriers (in electronvolts) is represented by energy isolines $\varepsilon_{\mathbf{k}}$ = const; the bold curves show the level $\varepsilon_{\mathbf{k}} = 1.64$ corresponding to the FS in the optimally doped compounds. The arrow indicates the scattering in hot spots by the AFM vector $\mathbf{Q} = (\pi, \pi)$ from state $\mathbf{k}_1$ under the FS to state $\mathbf{k}_2$ above the FS.

It should be noted that the spin–spin correlation function $C_{\mathbf{q}} = \langle S^{\alpha}_{-\mathbf{q}} S^{\alpha}_{\mathbf{q}}\rangle$ has a sharp peak at $\mathbf{q} = \mathbf{Q}$; this corresponds to a strong dependence of carrier scattering on the resonance structure of the spin fluctuation spectrum.

To take into account the scattering anisotropy that arises in our case due to the strong scattering by vector **Q**, we will use a multimoment approach to the solution of the equation of motion for the density matrix. This approach was developed for the description of the low-temperature behavior of coefficients $\rho(T)$ and $R_H(T)$ in polyvalent metals in the case of scattering from phonons [17, 18], where the scattering anisotropy increases due to the umklapp processes.

In the stationary case, the deviation from equilibrium can be defined by using the density matrix. The most general form of this matrix is $\hat{\rho}^0 = \hat{\rho}^{00}(1 + \hat{F})$, $\hat{\rho}^{00} = Z^{-1}\exp(-\hat{H}_0/T)$, $Z = \mathrm{Sp}\{\hat{H}_0\}$, $\langle\hat{F}\rangle \equiv \{\hat{\rho}^{00}\hat{F}\} = 0$.

To calculate the one-particle distribution function $f_{\mathbf{k}} = \mathrm{Sp}\{\hat{\rho}^0 a^\dagger_{\mathbf{k}\sigma} a_{\mathbf{k}\sigma}\}$, which determines the transport coefficients, we can choose the operator $\hat{F}$ as a one-particle operator, i.e., represent it in the form $\hat{F} = \sum_{\mathbf{k},\sigma} F(\mathbf{k}) a^\dagger_{\mathbf{k}\sigma} a_{\mathbf{k}\sigma}$. In this case, $f_{\mathbf{k}}$ can be written as $f_{\mathbf{k}} = f^0_{\mathbf{k}} + g_{\mathbf{k}}$, $f^0_{\mathbf{k}} = (1 + \exp(\varepsilon_{\mathbf{k}} - \mu)/T)^{-1}$, $g_{\mathbf{k}} = T(-\partial f^0/\partial\varepsilon_{\mathbf{k}})F(\mathbf{k})$, where μ is the chemical potential.

We seek $\hat{F}$ in the form of a linear superposition of a set of moments, viz., operators $\hat{F}_l$: $\hat{F} = \sum_l \eta_l \hat{F}_l$, $\hat{F}_l = \sum_{\mathbf{k},\sigma} F_l(\mathbf{k}) a^\dagger_{\mathbf{k}\sigma} a_{\mathbf{k}\sigma}$.

The solution of the evolution equation for the density matrix within the framework of linear response in the resistivity problem leads to the system of equations

$$X_l = \sum_{l'} P_{ll'}\eta^E_l, \quad X_l = \frac{1}{N}\sum_{\mathbf{k}} F_l(\mathbf{k}) e\mathbf{E}\mathbf{v}_{\mathbf{k}}(-\partial f^0/\partial\varepsilon_{\mathbf{k}}),$$

$$\mathbf{v}_{\mathbf{k}} = \hbar^{-1}\nabla_{\mathbf{k}}\varepsilon_{\mathbf{k}}.$$

$$P_{ll'} = \frac{\pi}{\hbar} J^2 \frac{1}{N^2}\sum_{\mathbf{k},\mathbf{q}} \frac{A_{\mathbf{q}}}{\hbar\omega_{\mathbf{q}}}(F_l(\mathbf{k}) - F_l(\mathbf{k}+\mathbf{q})) \tag{5}$$

$$\times (F_{l'}(\mathbf{k}) - F_{l'}(\mathbf{k}+\mathbf{q}))\, f^0_{\mathbf{k}}(1 - f^0_{\mathbf{k}+\mathbf{q}})$$

$$\times n_B(\hbar\omega_{\mathbf{q}})\delta(\varepsilon_{\mathbf{k}+\mathbf{q}} - \varepsilon_{\mathbf{k}} - \hbar\omega_{\mathbf{k}}).$$

This system is equivalent to the linearized Boltzmann equation if $\{\hat{F}_l\}$ is a complete set of operators commuting with $\hat{H}_0$. Clearly, we must restrict our analysis to a certain finite number l_0 of moments $\hat{F}_l$ that is chosen from the condition that the scattering anisotropy and the shape of the Fermi surface are correctly taken into account.

The usual practice in solving the Boltzmann equation is to use the relaxation time approximation that is equivalent to the one-moment approximation (OMA), $\hat{F} = \eta^E_1 \hat{F}^E_1$; $F^E_1(\mathbf{k}) = \mathbf{n}\mathbf{v}_{\mathbf{k}}$; $g^{(1),E}_{\mathbf{k}} = \tau e\mathbf{E}\mathbf{v}_{\mathbf{k}}(-\partial f^0/\partial\varepsilon_{\mathbf{k}})$; $\eta^E_1 = \tau eE/T$; and $\mathbf{n}$ is the unit vector in the direction of the applied electric field, which is assumed to be directed along the X axis.

We will restrict our subsequent analysis to the case of two moments ($l_0 = 2$), which will enable us to introduce the classification of various areas of the Brillouin zone ("hot" and "cold" spots). In this two-moment approximation (TMA), we choose the moments $F^E_1(\mathbf{k})$, $F^E_2(\mathbf{k})$ and the nonequilibrium distribution function $g^{(2),E}_{\mathbf{k}}$ in the form

$$g^{(2),E}_{\mathbf{k}} = T(\eta^E_1 F^E_1(\mathbf{k}) + \eta^E_2 F^E_2(\mathbf{k}))(-\delta f^0/\partial\varepsilon_{\mathbf{k}});$$
$$F^E_1(\mathbf{k}) = \mathbf{n}\mathbf{v}_{\mathbf{k}}, \quad F^E_2(\mathbf{k}) = (\mathbf{n}\mathbf{v}_{\mathbf{k}})^3. \tag{6}$$

The coefficients η^E_1 and η^E_2 can be found from system of Eqs. (5). The current density $j^\alpha = \sigma^{\alpha\beta}E^\beta$, $j^\alpha = \frac{1}{V}\sum_{\mathbf{k},\sigma} e v^\alpha_{\mathbf{k}} g^E_{\mathbf{k}}$ determines the conductivity tensor $\sigma^{\alpha\beta}$ and the resistivity tensor $\rho_{\alpha\beta} = \sigma^{-1}_{\alpha\beta}$. In the case of quadratic symmetry, $\rho = \rho_{xx} = \rho_{yy}$.

The found correction $g^E_{\mathbf{k}} = T\sum_l \eta^E_l F^E_l(\mathbf{k}) \times (-\partial f^0/\partial\varepsilon_{\mathbf{k}})$ is used at the second step for solving the system of equations in a magnetic field. The correction $g^H_{\mathbf{k}} = T\sum_l \eta^H_l F^H_l(\mathbf{k})(-\partial f^0/\partial\varepsilon_{\mathbf{k}})$ to the equilibrium distribution function in the presence of a Z-directed magnetic field is determined by the system of equations "along the Y axis":

$$X^y_l + X^H_l = \sum_{l'} P_{ll'}\eta^H_l,$$

$$X^y_l = \frac{1}{N}\sum_{\mathbf{k}} F^H_l(\mathbf{k}) eE^y v^y_{\mathbf{k}}(-\partial f^0/\partial\varepsilon_{\mathbf{k}}), \tag{7}$$

$$X^H_l = \frac{1}{N}\sum_{\mathbf{k}} F^H_l(\mathbf{k}) X^H_{\mathbf{k}},$$

$$X^H_{\mathbf{k}} = -\frac{e}{c\hbar}(\mathbf{v}_{\mathbf{k}} \times \mathbf{H})\partial g^E_{\mathbf{k}}/\partial\mathbf{k},$$
$$F^H_1(\mathbf{k}) = v^y_{\mathbf{k}}, \quad F^H_2(\mathbf{k}) = (v^y_{\mathbf{k}})^3. \tag{8}$$

There are two more equations for determining the Hall coefficient R_H and coefficients η^H_l; one of them corresponds to zero current in the Y direction: $j^y = \sum_{\mathbf{k},\sigma} e v^y_{\mathbf{k}} g^y_{\mathbf{k}} = 0$, $E^y = R_H j^x H^z$.

The resistivity $\rho(T)$ and the Hall coefficient $R_H(T)$ were calculated for the hole spectrum $\varepsilon_{\mathbf{k}}$ given by Eq. (3) with parameter $\tau = 0.2$ eV. The spectrum and the FS corresponding to the doping level $n_h = 0.15$ are shown in Fig. 1. For the magnon spectrum determined by Eq. (4), we chose the frustration parameter $p = 0.1$ and the exchange interaction $I = 0.7\tau$. Such a choice corresponds to the realistic spin–spin exchange interaction $I \sim 1500$ K in the CuO_2 plane and the characteristic hole dispersion $\varepsilon(0, 0) - \varepsilon_F \sim 0.5$ eV for the optimally doped HTSCs that is reliably measured in the ARPES

experiments. It should be noted that the spectrum chosen is close to the spectrum of the lower spin-polaron band for the optimal doping. In the majority of publications devoted to the calculations of $\rho(T)$ and $R_H(T)$, the spectrum is chosen so as to fit to the Fermi surface given by the ARPES experiments and corresponding to the doping level $n_h \approx 2$ [7, 8, 10]. It then turns out that the Van Hove singularity lies at points $X = (0, \pm\pi)$, $(\pm\pi, 0)$ and the bandwidth is $W = \varepsilon_\Gamma - \varepsilon_M = 1.6$ eV [7] and 2 eV [8]. In the spectrum used in this work, the Van Hove singularity is shifted, in accordance with the experiment, from the point X toward the point Γ. The bandwidth $\varepsilon_\mathbf{k}$ corresponds to $W \sim 0.7$ eV. It should be noted that, for a larger value of this quantity, it is impossible to describe the spectrum evolution in the direction of the low-doping limit (i.e., with decreasing number of holes) [14]. It will be shown below that the temperature behavior of $R_H(T)$ strongly depends on the choice of $\varepsilon_\mathbf{k}$. For this reason, analysis of $\rho(T)$ and $R_H(T)$ for $\varepsilon_\mathbf{k}$ differing from the values considered earlier seems to be essential.

Figure 2 shows the temperature dependence $\rho^{(2)}(T)$ of the resistivity calculated in the TMA (6) and the Hall coefficient $R_H^{(1,2)}(T)$ determined in the one- and two-moment approximations. In accordance with the experiment, $\rho^{(2)}(T)$ exhibits a linear dependence starting with low temperatures (≈70 K). We do not present the temperature dependence $\rho^{(1)}(T)$ in the OMA, because it differs only slightly from $\rho^{(2)}(T)$. However, the difference increases with decreasing temperature, and $\rho^{(2)}/\rho^{(1)} = 0.85$ at $T = 70$ K. The linear dependence $\rho^{(2)}(T)$ over a wide temperature range is determined by the following. In view of a comparatively narrow gap $\Delta = \omega_\mathbf{Q}$ ($\Delta(200\text{ K}) \approx 250$ K), the main contribution to the collision integral in the magnon spectrum comes from the backward scattering; in other words, for an electric field directed along the diagonal $\Gamma \longrightarrow (\pi, \pi)$ of the Brillouin zone (BZ), these are transitions between the FS sheets located in the first and the third quadrants of the BZ (Fig. 1). Obviously, at high temperatures, where the scattering is isotropic, the $\rho(T)$ dependence obeys a linear law. For a temperature-independent magnon spectrum, the backward scattering processes must be frozen out with a decrease in T, which could lead to a deviation from the linearity. However, in the 2D case, the magnon spectrum in the range of quasi-momenta close to the vector $\mathbf{Q}$ considerably softens with decreasing temperature. In particular, the gap Δ first decreases linearly and reaches a constant value only at $T < T^* \approx 50$ K (in the general case, the value of T^* is a function of I and the frustration parameter p). Such a temperature behavior of the spectrum draws the linear dependence $\rho^{(2)}(T)$ far into the low-temperature region.

Figure 2 shows that the temperature dependences $R_H^{(1)}(T)$ and $R_H^{(2)}(T)$ are noticeably different. The quantity $R_H^{(2)}(T)$ qualitatively reproduces the experimental behavior of the Hall coefficient in the HTSC characterized by the law $R_H(T) \sim 1/T$.

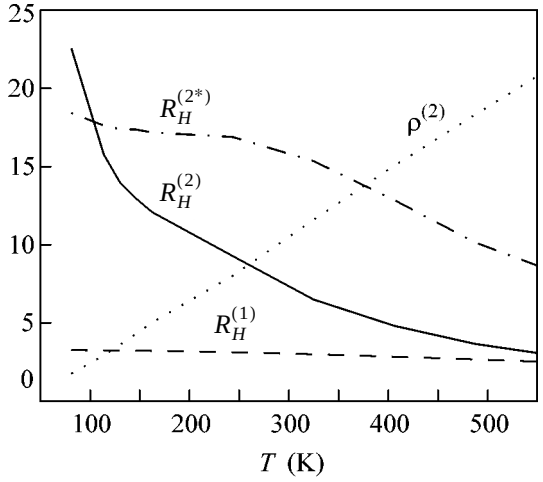

Fig. 2. Temperature dependences of resistivity $\rho^{(2)}(T)$ (in units of the ratio $\rho^{(2)}(T)/\rho^{(2)}$ ($T = 50$ K)) and of the Hall coefficient $R_H^{(1)}(T)$ and $R_H^{(2)}(T)$ (in units of $R_H(T)/R_H^{(1)}$ ($T = 150\text{ K} \cdot 3$) for the spectrum defined by coefficients (3). The temperature dependence $R_H^{(2)*}(T)$ of the Hall coefficient corresponds to coefficients (9) of carrier spectrum (2).

To explain the strong difference between $R_H^{(2)}$ and $R_H^{(1)}$ in the low-temperature range, we compare the nonequilibrium corrections $g_\mathbf{k}^{(1),E}$ and $g_\mathbf{k}^{(2),E}$ to the one-particle distribution function that are calculated in the OMA and TMA, respectively, at the temperature $T = 150$ K and are shown in Figs. 3a and 3b. The functions $g_\mathbf{k}^{(1,2),E}$ are represented by the isolines for an electric field directed along the $\Gamma \longrightarrow (\pi, \pi)$ diagonal.

It can be seen from Fig. 1 that strong scattering occurs between the FS areas in the first and third quadrants, where the FS intersects the AFM BZ boundaries, i.e., X–X lines (transitions from the state $\mathbf{k}_1$ to $\mathbf{k}_2$ in Fig. 1). These areas correspond to the hot spots, and the scattering between them makes the main contribution to the collision integrals $P_{ll'}$ at low temperatures because of a large difference in velocities $(\mathbf{v}_\mathbf{k} - \mathbf{v}_{\mathbf{k}+\mathbf{q}})^2$ (backward scattering) and the closeness of the magnon quasi-momentum $\mathbf{q}$ to the AFM vector $\mathbf{Q}$. For this reason, the hot spots correspond to a short relaxation time. The TMA makes it possible to take into account the fact that the conductivity must be determined by the FS areas corresponding to a long relaxation time, viz., to the cold spots (in our case, these areas correspond to the intersection of the FS with the $(-\pi, -\pi) - (\pi, \pi)$ diagonal). This is clearly seen in Figs. 3a and 3b, where the

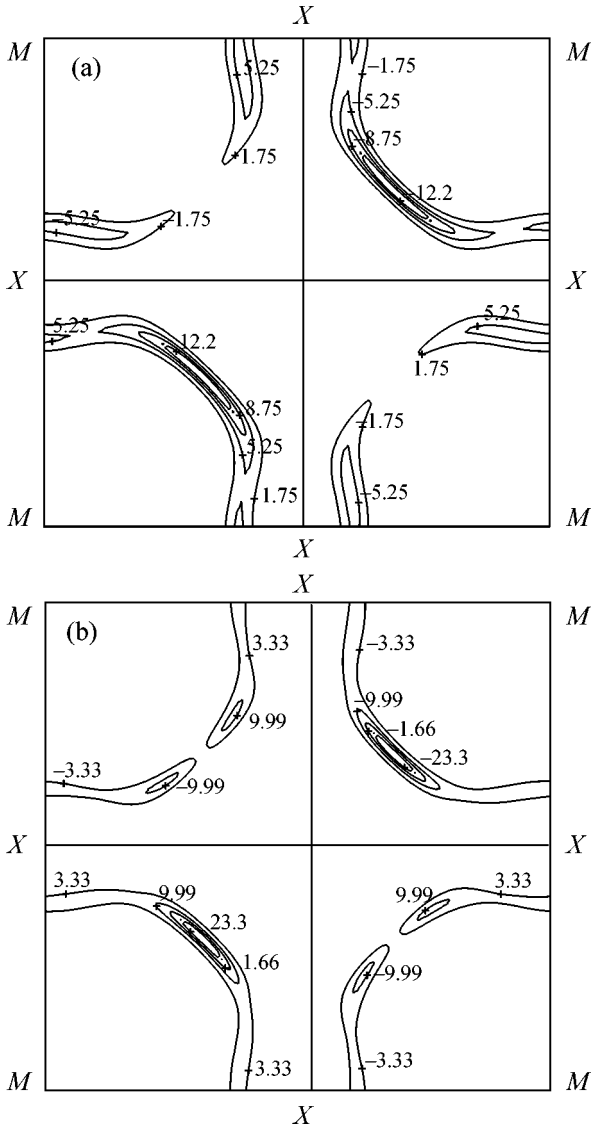

Fig. 3. The nonequilibrium correction to the one-particle distribution function $g_{\mathbf{k}}^{E}$ (in arbitrary units) is represented by isolines for $T = 150$ K (the electric field is directed along the $\Gamma \longrightarrow (\pi, \pi)$ diagonal of the Brillouin zone): (a) in the OMA for $g_{\mathbf{k}}^{(1),E}$ and (b) in the TMA for $g_{\mathbf{k}}^{(2),E}$.

$g_{\mathbf{k}}^{(2),E}$ value at cold spots is twice as large as $g_{\mathbf{k}}^{(1),E}$. It is essential that the strong redistribution in the nonequilibrium density $g_{\mathbf{k}}^{E}$ upon passing from the OMA to the TMA also occurs in the portion of the *k* space corresponding to the FS areas located in the second and fourth quadrants. It can be seen that the derivatives of $g_{\mathbf{k}}^{(2),E}$ in the second and fourth quadrants of the *k* space increase by three to four times relative to the OMA. One can verify that it is the derivatives of $g_{\mathbf{k}}^{(2),E}$ in the second and fourth quadrants that play a decisive role in the Hall-field term $X_{\mathbf{k}}^{H}$.

This determines the strong difference between $R_H^{(2)}$ and $R_H^{(1)}$ in the low-temperature range. With increasing temperature, the scattering becomes isotropic and the shape of $g_{\mathbf{k}}^{(2),E}$ becomes close to the shape of $g_{\mathbf{k}}^{(1),E}$, which is independent of the scattering mechanism and is determined by the purely geometrical factors associated only with the $\varepsilon_{\mathbf{k}}$ spectrum. As a result, $R_H^{(2)}(T)$ approaches $R_H^{(1)}(T)$ with increasing temperature.

Let us also demonstrate that a detailed form of the temperature dependence $R_H(T)$ is determined, to a considerable extent, by the topology of the hole spectrum. The dot-and-dash curve in Fig. 2 shows the dependence $R_H^{(2)}(T)$ for a spectrum which differs only slightly from the one used earlier and which is defined by the coefficients

$$a_1 = 1.5, \quad a_2 = 3.0, \quad a_3 = -1.25, \quad a_4 = -0.3, \quad a_5 = -0.3. \tag{9}$$

It can be seen that the new Hall coefficient $R_H^{(2)*}(T)$ (for the same value $n_h = 0.15$ of the hole concentration) shows a tendency to saturation at both high and low temperatures. The details of the $R_H^{(2)*}(T)$ dependence considerably differ from the $R_H^{(2)}(T)$ dependence.

It should be noted in conclusion that a further analysis of the Hall effect is essential, primarily in connection with an increase in the number of moments and with the necessity of taking into account the fact that the residues for bare holes in the lower spin-polaron band differ from unity and noticeably depend on the quasi-momentum.

This study was supported by the Russian Foundation for Basic Research.

REFERENCES

1. A. Carrington, A. P. Mackenzie, C. T. Lin, and J. R. Cooper, Phys. Rev. Lett. **69**, 2855 (1992).
2. J. M. Harris, Y. F. Yan, and N. P. Ong, Phys. Rev. B **46**, 14293 (1992).
3. A. Malinowski, M. Z. Cieplak, S. Guha, *et al.*, Phys. Rev. B **66**, 104512 (2002).
4. A. Carrington, D. J. C. Walker, A. P. Mackenzie, and J. R. Cooper, Phys. Rev. B **48**, 13051 (1993).
5. H. Y. Hwang, B. Batlogg, H. Takagi, *et al.*, Phys. Rev. Lett. **72**, 2636 (1994).
6. T. Nishikawa, J. Takeda, and M. Sato, J. Phys. Soc. Jpn. **63**, 1441 (1994).
7. B. P. Stojkovic and D. Pines, Phys. Rev. B **55**, 8576 (1997).

8. R. Hlubina and T. M. Rice, Phys. Rev. B **51**, 9253 (1995).
9. L. B. Ioffe and A. J. Millis, Phys. Rev. B **58**, 11631 (1998).
10. A. Perali, M. Sindel, and G. Kotliar, Eur. Phys. J. B **24**, 487 (2001).
11. V. J. Emery, Phys. Rev. Lett. **58**, 2794 (1987).
12. V. J. Emery and G. Reiter, Phys. Rev. B **38**, 4547 (1988).
13. F. C. Zhang and T. M. Rice, Phys. Rev. B **37**, 3759 (1988).
14. A. F. Barabanov, R. Hayn, A. A. Kovalev, *et al.*, Zh. Éksp. Teor. Fiz. **119**, 777 (2001) [JETP **92**, 677 (2001)].
15. A. F. Barabanov, A. A. Kovalev, O. V. Urazaev, and A. M. Belemouk, Phys. Lett. A **265**, 221 (2000).
16. A. F. Barabanov and V. M. Berezovsky, Phys. Lett. A **186**, 175 (1994); Zh. Éksp. Teor. Fiz. **106**, 1156 (1994) [JETP **79**, 627 (1994)].
17. A. F. Barabanov and L. A. Maksimov, Fiz. Met. Metalloved. **29**, 471 (1970).
18. J. Black and D. L. Mills, Phys. Rev. B **9**, 1458 (1974).

Translated by N. Wadhwa

JETP Letters, Vol. 79, No. 4, 2004, pp. 166–170. Translated from Pis'ma v Zhurnal Éksperimental'noĭ i Teoreticheskoĭ Fiziki, Vol. 79, No. 4, 2004, pp. 201–205.

Mesoscopic Fluctuations of Thermopower in a Periodic Antidot Lattice

M. V. Budantsev[1], R. A. Lavrov[1], A. G. Pogosov[1, 2, *], A. E. Plotnikov[1], A. K. Bakarov[1], A. I. Toropov[1], D. K. Maude[3], and J. C. Portal[3]

[1] *Institute of Semiconductor Physics, Siberian Division, Russian Academy of Sciences, pr. Akademika Lavrent'eva 13, Novosibirsk, 630090 Russia*

**e-mail: pogosov@isp.nsc.ru*

[2] *Tomsk State University, Tomsk, 630045 Russia*

[3] *Grenoble High Magnetic Fields Laboratory, MPI-FKF and CNRS, B.P.166, F-38042 Grenoble, France*

Received January 22, 2004

The mesoscopic fluctuations of thermopower (MFT) were experimentally observed in an AlGaAs/GaAs heterojunction with a low-resistance (~$0.02h/e^2$) periodic antidot lattice in the situation where the mesoscopic fluctuations of conductance (MFC) were absent to within the experimental accuracy. The MFT spectrum contained a periodic component associated with the Aharonov–Bohm h/e oscillations in the area occupied by one antidot, whereas the $h/2e$ oscillations were not observed. It is shown that a sizable contribution to the MFT comes from the interference of electron trajectories localized inside billiards formed by four neighboring antidots. Contrary to MFC, the MFT autocorrelation function in single billiards deviates from the Lorentzian form. © *2004 MAIK "Nauka/Interperiodica".*

PACS numbers: 73.23.Ad; 73.50.Lw

Periodic antidot lattices [1] are a version of electron billiards. At present, they are being extensively studied both experimentally and theoretically. As a rule, the emphasis is placed on only one of the kinetic coefficients, namely, on the conductance (resistance), whereas the other kinetic coefficient (thermopower) remains poorly studied. The magnetoresistance of the antidot lattices exhibits so-called commensurate oscillations [2–4] arising as a result of the formation of stable electron orbits [5, 6]. As the temperature decreases, the mesoscopic fluctuations of conductance (MFC) caused by the interference of electron waves are observed on the background of the classical commensurate oscillations [7–12]. Contrary to the conventional disordered conductors, the MFC in electron billiards are not universal and reflect the particular characteristics of billiards and dynamic chaos in them [9]. In this respect, the studies of mesoscopic effects in electron billiards is of considerable interest. However, the experimental study of MFC is possible only in rather high-ohmic conductors, because the amplitude of these fluctuations is on the order of $\delta G \sim e^2/h$, and, hence, the relative fluctuation amplitude $\delta R/R = \delta G/G \sim (e^2/h)R$ of a measured quantity (resistance) is proportional to this resistance. Thus, the mesoscopic effects in widely open systems remain poorly studied experimentally. The thermopower has appreciable advantages in this respect. Indeed, the classical magnitude of thermopower in the degenerate systems is small because of the symmetry of quasielectrons (above the Fermi level) and quasiholes (below the Fermi energy). In the mesoscopic systems, this symmetry is broken and the amplitude of mesoscopic fluctuations becomes larger than the mean value of thermopower [13]. Therefore, the thermopower is a much more sensitive tool for studying the mesoscopic phenomena compared to the magnetoresistance.

This work reports the results of experimental study of the mesoscopic fluctuations of thermopower (MFT) in a two-dimensional electron gas (2DEG) with a low-resistance (~$0.02h/e^2$) periodic antidot square lattice.

Experimental samples were fabricated on the basis of an AlGaAs/GaAs heterojunction containing 2DEG with electron mobility $\mu = (5–7) \times 10^5$ cm^2/(V s) and density $N_S = (2–5) \times 10^{11}$ cm^{-2} using electron-beam lithography and subsequent anisotropic plasma-chemical etching. The lattice parameter was $d = 0.9$ μm and the antidot radius was $a = 0.2–0.3$ μm with allowance for the depletion layers. The antidots were placed at the Hall bridge with sizes $L \times W = 9 \times 6$ μm (Fig. 1). The thermopower was measured using a heater in the form of a 12-μm-long 2-μm-wide conducting channel adjacent to the Hall bridge.

The thermopower was measured by the standard method of local heating that allows the measurement of diffusional thermopower without a contribution from phonon drag (see [14–16] and references cited therein). A weak current with frequency f was passed through the heater (between contacts *3* and *6*), and the potential

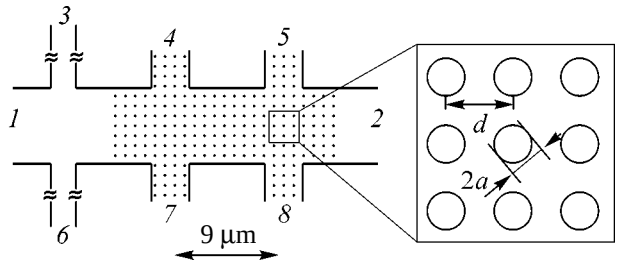

Fig. 1. Geometry of the experimental sample and arrangement of contacts. Lattice parameter is $d = 0.9$ μm, and the antidot radius is $a = 0.2$–0.3 μm.

difference between different billiard contact pairs was recorded at frequency $2f$ as a function of magnetic field perpendicular to the 2DEG plane. Joule heat produced by the heating current raises the temperature of electron gas near the heater and creates temperature gradient along the billiards. At a sufficiently low frequency f, the temperature gradient oscillates with frequency $2f$ and, therefore, the voltage measured at this frequency proves to be proportional to the thermopower. In this work, we report the results of studying the transverse thermovoltage U_{47} (the Nernst–Ettingshausen effect). Since the scheme of measuring the longitudinal thermovoltage U_{78} was asymmetrical, it was necessary to symmetrize it about reverting sign of magnetic field. This procedure is reasonable for the effects associated with classical transport, where the thermomagnetic phenomena are described in terms of a local thermopower tensor. However, this averaging loses its meaning in the case of mesoscopic thermopower fluctuations, because the latter are nonlocal and, generally, asymmetrical about changing sign of magnetic field. For this reason, we restricted ourselves to the study of transverse thermovoltage. The magnetoresistance was measured for the same structure. Measurements were carried out in a dissolution refrigerator (Oxford Instruments) at temperature $T = 60$ mK. Magnetic field was directed perpendicular to the 2DEG plane and varied from –2 to 2 T.

The magnetic-field dependences of the longitudinal $R_L = U_{45}/I_{12}$ and transverse (Hall) $R_H = U_{47}/I_{12}$ resistances measured for the bias current $I_{12} = 10^{-9}$ A are shown in Fig. 2a. The longitudinal magnetoresistance exhibits well-defined oscillations, with the main peak at $B \approx 0.18$ T corresponding to the commensurability condition $2R_c = d$, where R_c is the electron Larmor radius. The Hall resistance is nonlinear in this range of magnetic fields. Such a behavior of the magnetoresistance of antidot lattices is caused by the classical chaotic dynamics of electrons moving in a periodic potential of antidots [5, 6]. One can see in Fig. 2 that the mesoscopic conductance fluctuations are absent. A detailed analysis of these dependences shows that the MFC amplitude is lower than the instrumental noise ($\Delta U <$ 0.05 nV). To check that 2DEG was not heated by the

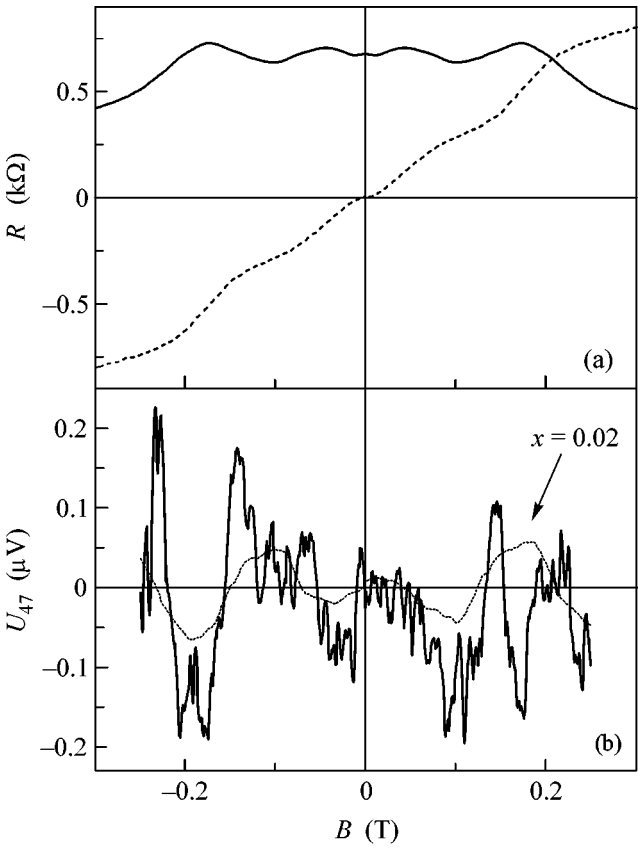

Fig. 2. (a) Longitudinal (solid line) and Hall (dots) magnetoresistances. (b) Equally scaled thermovoltages U_{47} measured for the minimal $I_{36} = 3.5 \times 10^{-7}$ A (solid line) and maximal $I_{36} = 4 \times 10^{-6}$ A (dots) heating currents.

bias current, which could suppress the MFC, the magnetoresistance was measured for $I_{12} = 10^{-10}$ A; however, this only impaired the signal-to-noise ratio. One can thus conclude that the MFC in an open antidot lattice are absent to within experimental accuracy.

The thermovoltage U_{47} demonstrates a cardinally different behavior (Fig. 2b). For a sufficiently high heating current, $I_{36} = 4 \times 10^{-6}$ A, for which the electron subsystem is strongly heated and its temperature breaks away from the lattice temperature, $T_e \gg T_L$, the thermopower is a smooth function of magnetic field and displays detectable oscillations accompanied by the change of sign. The features in the magnetoresistance and thermopower curves are correlated, allowing the conclusion to be drawn that they are also determined by the chaotic electron dynamics. The $U_{47}(B)$ dependence is antisymmetric with respect to the magnetic field, in accordance with the Onsager relation for the thermopower nondiagonal tensor component. The classical thermopower commensurate oscillations will be the subject of a separate paper. As the heating current decreases, the behavior of thermopower changes substantially; on the background of classical oscillations,

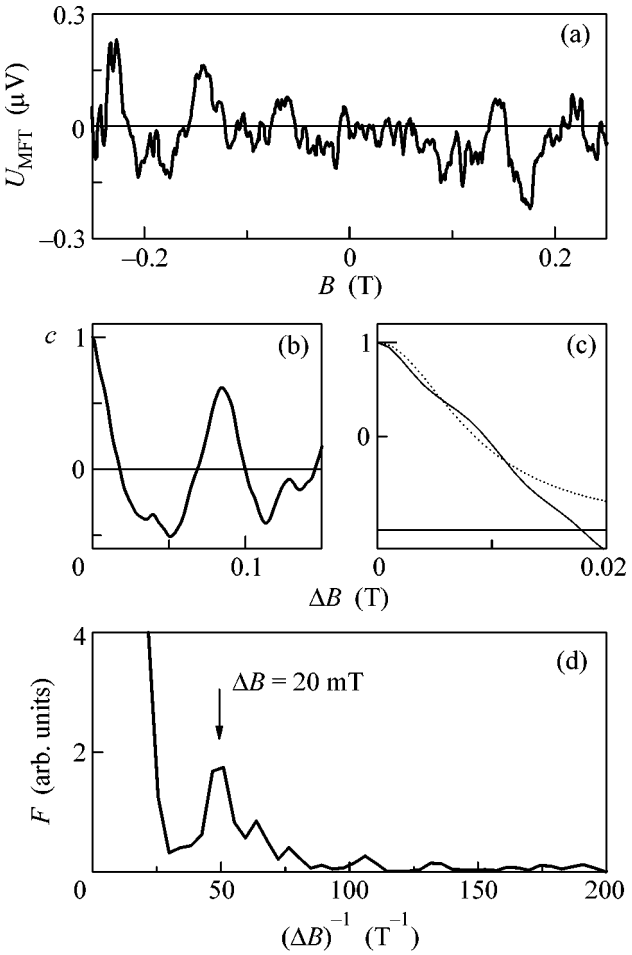

Fig. 3. (a) Mesoscopic fluctuations of thermal voltage U_{MFT} separated on the background of its classical commensurate oscillations; (b, c) autocorrelation function $C(U_{MFT})$; and (d) Fourier-transform spectrum of mesoscopic fluctuations; the dotted line in (c) shows the best approximation of the autocorrelation function by the Lorentzian curve in the range of small ΔB.

reproducible high-frequency fluctuations appear, whose relative amplitude increases and, for the heating current $I_{36} = 3.5 \times 10^{-7}$ A, becomes appreciably larger than the amplitude of classical thermopower oscillations. The strong dependence of the thermopower fluctuations on the electron temperature allows the conclusion to be drawn that they result from the quantum interference.

The MFT can be separated on the background of a smoothly varying classical thermopower through the subtraction of the $U_2(B)$curve corresponding to high power, for which the MFT are suppressed, from the low-power $U_1(B)$ curve. However, in so doing, one should keep in mind that, according to the Mott's formula, $S = eL_0(d\ln\sigma/dE)T_e$ ($L_0 = \pi^2 k_B^2/3e^2$ is the Lorentz number, k_B is the Boltzmann constant, and e is electron charge), while the thermovoltage is $U = S\nabla T_e = eL_0(d\ln\sigma/dE)T_e\nabla T_e$; i.e., it is proportional to the mean electron-gas temperature and its gradient inside the sample. Since both these quantities change with a change in heating power, the MFT should be calculated by taking difference $U_{MFT}(B) = U_1(B) - \alpha U_2(B)$, where $\alpha = T_{e1}\nabla T_{e1}/(T_{e2}\nabla T_{e2})$ and indices 1 and 2 refer to the weak and strong heating, respectively. In our case, the coefficient $\alpha \approx 0.02$ was found under the assumption that the MFT and classical oscillations do not correlate, i.e., from the condition that the correlator $C(U_{MFT}, U_2) = 0$. The separated mesoscopic fluctuations of thermal voltage U_{MFT} are shown in Fig. 3a.

The autocorrelation function $C(\Delta B)$ of the mesoscopic thermopower fluctuations is shown in Fig. 3b. The correlation magnetic field $\Delta B_c \approx 9$ mT corresponds to an area equal to $\Phi_0/\Delta B_c \approx 0.5$ μm^2, where $\Phi_0 = h/e$ is the magnetic flux quantum. In the conventional disordered conductors, $\Phi_0/\Delta B_c = \min(L_\varphi^2, S)$, where L_φ is the phase coherence length and S is the sample characteristic area. The estimate of the phase interruption time, according to [17], gives in our case $\tau_\varphi \approx 2 \times 10^{-9}$ s for $T =$ 60 mK, which corresponds to $L_\varphi = \sqrt{D\tau_\varphi} \approx 8$ μm. The experimental sample had approximately the same sizes. Therefore, $\Phi_0/\Delta B_c$ proves to be appreciably smaller than both L_φ^2 and the sample size. Assume that the main contribution to the MFT comes from the interference of electron trajectories localized inside the crossing-type billiards formed by four neighboring antidots. The areas of these billiards are $S_4 = d^2 - \pi a^2 \approx 0.6$ μm^2. According to [18], the value of $\Phi_0/\Delta B_c$ for single billiards coincides with the area encompassed by the classical trajectories passing through the billiards; i.e., it should be $\Phi_0/\Delta B_c \lessapprox S_4$, which is observed in our case. Thus, an appreciable contribution to the MFT comes from the interference of electron trajectories inside the crossings between four neighboring antidots.

On the tail of the autocorrelation function (at $\Delta B > \Delta B_c$), oscillations with a considerable amplitude are observed. Numerical simulation carried out in [18] shows that similar oscillations are also observed for the MFC because of the nonuniversal behavior of short trajectories. It was also shown in that work that, at small ΔB, the MFC autocorrelation function for single billiards (including billiards of the crossing type) are well described by the Lorentzian function. It is seen in Fig. 3c that, in our case, i.e., for the MFT in a periodic lattice with such crossings, the shape of the $C(\Delta B)$ curve is poorly described by the Lorentzian. We failed to explain unambiguously this discrepancy. It may be caused by the difference in the MFT and MFC spectra in single billiards, as well as by the interference of electron trajectories leaving the crossing. Such an interference may occur in our system. Indeed, let us compare τ_φ with the residence time τ_t of an electron in the crossing between four neighboring antidots. The latter time

can be estimated from the classical conductance under the assumption that an electron executes random hopping at a distance on the order of d in time τ_t (this assumption is justified if the electron transit time d/v_F to the neighboring crossing is much shorter than τ_t). The diffusion coefficient is then $D = d^2/\tau_t$. Conductance measurements give $\tau_t \approx 2.5 \times 10^{-11}$ s for the diffusion coefficient. This value is much larger than $d/v_F \approx 4 \times 10^{-12}$ s, justifying our assumption. Thus, we have for our system $d/v_F \ll \tau_t \ll \tau_\varphi$. The first inequality explains the overwhelming contribution to MFT from the electron trajectories interfering inside the crossing between four neighboring antidots, as was assumed above, whereas the second inequality ($\tau_t \ll \tau_\varphi$) allows one to expect that long electron trajectories leaving the crossing also make a contribution to the MFT.

The MFT Fourier-transform spectra, shown in Fig. 3d, indicate that the thermopower fluctuations are quasiperiodic and contain a component oscillating with the period $\Delta B = 20$ mT. This period corresponds to the Aharonov–Bohm h/e oscillations caused by the quantization of magnetic flux through the area πa^2 occupied by one antidot ($\Delta B = (h/e)/\pi a^2$). Phenomenologically, one can expect the presence of the Aharonov–Bohm h/e and $h/2e$ oscillations in our system on the areas d^2, πa^2, and $d^2 - \pi a^2$. The observation of the conductance oscillations with periods $\Delta B = (h/2e)/d^2$ and $\Delta B = (h/e)/(d^2 - \pi a^2)$ in the antidot lattices was already reported, in [19] and [9] respectively. In our case, the frequencies of all these oscillations are positioned at intervals appreciably larger than the peak width at $\Delta B = 20$ mT, so that this peak can be unambiguously assigned to the h/e oscillations on the area πa^2. It is worth noting that oscillations of this type can exist only in the presence of interference on long electron trajectories that encompass the antidot, i.e., pass through at least four adjacent crossings. It was shown above that such interference may occur in our system. An important feature of the MFT spectrum in our system is that the $h/2e$ oscillations, which are ordinarily treated as a periodic modulation of the weak-localization effect, are absent. This result is in accord with recent work [15] devoted to the thermopower of quantum dots, where the MFT was observed, whereas the weak-localization effects did not show up. Theoretically, the h/e and $h/2e$ oscillations in the lattices should behave in a substantially different way. Indeed, the h/e oscillations have random phases in different cells, so that their amplitude is suppressed as $1/\sqrt{N}$, where N is the number of cells. Under the same conditions, the amplitude of the Altshuler–Aronov–Spivak oscillations [20] having period $h/2e$ is not suppressed, because these oscillations are caused by the interference on the trajectory pairs that interchange upon time reversion and, hence, have zero phase difference in the absence of a magnetic field. In the presence of a large number of such trajectory pairs encompassing various areas in the system, the $h/2e$ oscillations can be suppressed by the magnetic field. Such a behavior of the h/e and $h/2e$ oscillations was confirmed in the experimental study of conductance [21]. However, recent work [22] reports the observation of conductance h/e oscillations in the absence of $h/2e$ oscillations in weak magnetic fields. A detailed explanation of all MFT features observed in this work is beyond the scope of the available models and calls for separate theoretical analysis.

Note in conclusion that we have experimentally studied the diffusional thermopower in a widely open square antidot lattice with a resistance of ~$0.02h/e^2$ at a temperature of 60 mK. Well-defined mesoscopic thermopower fluctuations were observed, whereas the mesoscopic conductance fluctuations were absent to within the experimental accuracy. Analysis of the MFT autocorrelation function $C(\Delta B)$ have shown that they are caused by the interference of electron trajectories geometrically localized inside crossings formed by four neighboring antidots. Contrary to the MFC in single billiards, $C(\Delta B)$ for the MFT in antidot lattice is not described by the Lorentzian function at small ΔB. The MFT spectrum contains a periodic component that corresponds to the h/e oscillations on the area occupied by one antidot. Thus, it has been demonstrated that, in the case of widely open systems, where the influence of mesoscopic effects on the traditionally studied resistance is small and undetectable, the thermopower provides a unique possibility of experimentally studying the quantum mesoscopic phenomena.

This work was supported by grant no. MK-253.2003.02 from the President of the Russian Federation, INTAS (grant no. 03-55-639), and the Russian Foundation for Basic Research (project no. 04-02-16894).

REFERENCES

1. K. Ensslin and P. M. Petroff, Phys. Rev. B **41**, 12307 (1990).
2. A. Lorke, J. P. Kotthaus, and K. Ploog, Superlattices Microstruct. **9**, 103 (1991).
3. D. Weiss, M. L. Roukes, A. Menschig, *et al.*, Phys. Rev. Lett. **66**, 2790 (1991).
4. G. M. Gusev, Z. D. Kvon, V. M. Kudryashov, *et al.*, Pis'ma Zh. Éksp. Teor. Fiz. **54**, 369 (1991) [JETP Lett. **54**, 364 (1991)].
5. É. M. Baskin, G. M. Gusev, Z. D. Kvon, *et al.*, Pis'ma Zh. Éksp. Teor. Fiz. **55**, 649 (1992) [JETP Lett. **55**, 678 (1992)].
6. R. Fleischmann, T. Geisel, and R. Ketzmerick, Phys. Rev. Lett. **68**, 1367 (1992).
7. G. M. Gusev, Z. D. Kvon, L. V. Litvin, *et al.*, Pis'ma Zh. Éksp. Teor. Fiz. **55**, 129 (1992) [JETP Lett. **55**, 123 (1992)].
8. F. Nihey and K. Nakamura, Physica B (Amsterdam) **184**, 398 (1993).

9. M. V. Budantsev, Z. D. Kvon, A. G. Pogosov, *et al.*, Pis'ma Zh. Éksp. Teor. Fiz. **59**, 614 (1994) [JETP Lett. **59**, 645 (1994)].
10. R. Schuster, K. Ensslin, D. Wharam, *et al.*, Phys. Rev. B **49**, 8510 (1994).
11. M. V. Budantsev, Z. D. Kvon, A. G. Pogosov, and L. V. Litvin, Superlattices Microstruct. **24**, 291 (1998).
12. A. Dorn, M. Sigrist, A. Fuhrer, *et al.*, Appl. Phys. Lett. **80**, 252 (2002).
13. A. V. Anisovich, B. L. Al'tshuler, A. G. Aronov, and A. Yu. Zyuzin, Pis'ma Zh. Éksp. Teor. Fiz. **45**, 237 (1987) [JETP Lett. **45**, 295 (1987)].
14. N. J. Appleyard, J. T. Nicholls, M. Y. Simmons, *et al.*, Phys. Rev. Lett. **81**, 3491 (1998).
15. S. F. Godijn, S. Moller, H. Buhmann, and L. W. Molenkamp, Phys. Rev. Lett. **82**, 2927 (1999).
16. A. G. Pogosov, M. V. Budantsev, D. Uzur, *et al.*, Phys. Rev. B **66**, 201303 (2002).
17. B. L. Altshuler, A. G. Aronov, and D. E. Khmelnitsky, J. Phys. C **15**, 7367 (1982).
18. R. A. Jalabert, H. U. Baranger, and A. D. Stone, Phys. Rev. Lett. **65**, 2442 (1990).
19. F. Nihey, S. W. Hwang, and K. Nakamura, Phys. Rev. B **51**, 4649 (1995).
20. B. L. Al'tshuler, A. G. Aronov, and B. Z. Spivak, Pis'ma Zh. Éksp. Teor. Fiz. **33**, 101 (1981) [JETP Lett. **33**, 94 (1981)].
21. C. P. Umbach, C. Van Haesendonck, R. B. Laibowitz, *et al.*, Phys. Rev. Lett. **56**, 386 (1986).
22. C. Naud, G. Faini, and D. Mailly, Phys. Rev. Lett. **86**, 5104 (2001).

Translated by V. Sakun

JETP Letters, Vol. 79, No. 4, 2004, pp. 171–176. From Pis'ma v Zhurnal Éksperimental'noĭ i Teoreticheskoĭ Fiziki, Vol. 79, No. 4, 2004, pp. 206–211.

Manifestation of the Bulk Phase Transition in the Edge Energy Spectrum in a Two-Dimensional Bilayer Electron System¶

E. V. Deviatov[1, *], A. Würtz[2], A. Lorke[2], M. Yu. Melnikov[1], V. T. Dolgopolov[1], A. Wixforth[3], K. L. Campman[4], and A. C. Gossard[4]

[1] *Institute of Solid State Physics, Russian Academy of Sciences, Chernogolovka, Moscow region, 142432 Russia*
** e-mail: dev@issp.ac.ru*

[2] *Laboratorium für Festkörperphysik, Universität Duisburg-Essen, D-47048 Duisburg, Germany*

[3] *Institut für Physik, Universitat Augsburg, Uhiversitatsstrasse, 1 D-86135 Augsburg, Germany*

[4] *Materials Department and Center for Quantized Electronic Structures, University of California, Santa Barbara, California 93106, USA*

Received January 22, 2004

We use a quasi-Corbino sample geometry with independent contacts to different edge states in the quantum Hall effect regime to investigate the edge energy spectrum of a bilayer electron system at a total filling factor of $\nu = 2$. By analyzing nonlinear *I–V* curves in normal and tilted magnetic fields, we conclude that the edge energy spectrum is in a close connection with the bulk one. At the bulk phase transition spin-singlet–canted antiferromagnetic phase, the *I–V* curve becomes linear, indicating the disappearance or strong narrowing of the $\nu = 1$ incompressible strip at the edge of the sample. © *2004 MAIK "Nauka/Interperiodica".*

PACS numbers: 73.21.Ac; 73.43.Nq

In a quantizing magnetic field, energy levels in a two-dimensional (2D) electron gas (2DEG) bend up near the edges of the sample, forming edge states (ESs) at the intersections with the Fermi level. Electron transport through ESs is responsible for many transport phenomena in 2D, as it was firstly proposed by Büttiker [1] and further developed by Chklovskii *et al.* [2] for interacting electrons. This ES picture is in good agreement with experimental results [3] on the transport both along ESs and between them.

Two principally different sample geometries were applied for transport investigations *between* different ESs: (i) a cross-gated Hall-bar [3] and (ii) a split-gated quasi-Corbino geometry [4, 5]. While measurements in a Hall-bar geometry provide information on the equilibration length between ESs [3, 6], investigations in a quasi-Corbino geometry are used to study the energy spectrum at the edge of a 2D system [5]. So far all experiments on the interedge channel equilibration have been performed on single-layer 2D systems, despite the fact that bilayer electron systems also seem to be very interesting.

In the bulk of a bilayer system, each Landau level is split into four sublevels corresponding to the spin and symmetric–antisymmetric splitting, which is caused by interlayer tunneling. In the simplest case of a weak Coulomb interlayer interaction, the interplay between the symmetric–antisymmetric splitting Δ_{SAS} and the Zeeman splitting is responsible for the bulk properties of bilayer systems at a filling factor of $\nu = 2$. Δ_{SAS} depends only on the electron concentration, so at fixed total filling factor, it diminishes with increasing magnetic field. In contrast, the Zeeman splitting is proportional to the absolute value of the magnetic field. For this reason, at a total filling factor of $\nu = 2$, in low quantizing magnetic fields, two occupied energy levels are separated by a bare Zeeman energy. These two occupied levels belong to different spin orientations, so that the system is in a spin-singlet state. The excitation energy at a filling factor of $\nu = 2$ is determined by the next energy scale, i.e., the symmetric–antisymmetric splitting, and is equal to $\Delta_{SAS} - g\mu B$. Increasing the magnetic field at fixed total filling factor, the excitation energy goes to zero. At zero excitation energy, $\Delta_{SAS} = g\mu B$ and a spectrum reconstruction occurs: at higher fields, Δ_{SAS} is the minimal energy scale, so both the filled levels are at the same spin orientation (in the field direction). The bilayer system is said to be in a ferromagnetic state. This spin-singlet–ferromagnetic phase transition can be driven also by an in-plane field component at fixed normal magnetic field. Indeed, this is only the Zeeman term which depends on the absolute value of the field, while the other energy scales are determined by the normal field component.

Regarding the single-particle approximation (without significant inter-layer interactions), while increas-

¶ This article was submitted by the authors in English.

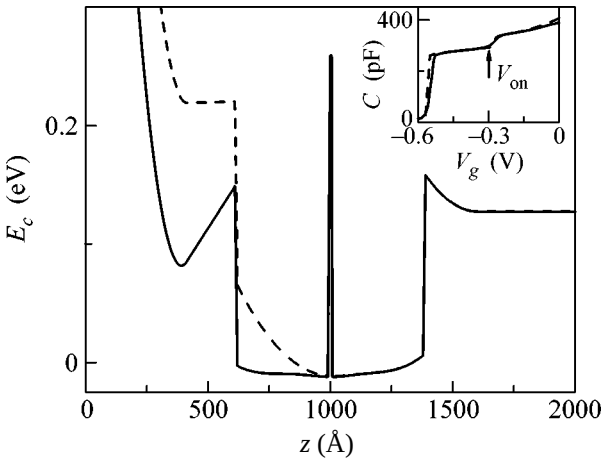

Fig. 1. Quantum well subband diagram at zero gate voltage (solid line) and at twice smaller electron conservation (dashed line) as calculated from the growth sequence of the structure (calculated using Poisson–Schrodinger solver by G. Snider). Inset shows the capacitance of the sample in dependence on the gate voltage calculated from the subband diagram (dashed) and measured in the experiment (solid). The magnetic field is zero.

ing the Zeernan splitting, the bilayer system at a filling factor of $\nu = 2$ undergoes a direct phase transition from a spin-singlet to a ferromagnetic state [7] at a critical magnetic field of $B_c = \Delta_{SAS}/g\mu$. However, in experiments with high interlayer Coulomb interaction [8, 9] (the distance between the layers is comparable to the magnetic length), the transition point is significantly shifted to lower fields. This was understood as a manifestation of many-body effects [10–12]. It was shown theoretically that the interlayer Coulomb interaction shifts the transition point to a value of $\mu g B_c \approx \Delta_{SAS}^2/E_c$, where E_c is the Coulomb energy. At the field B_c, a transition from the spin-singlet to a novel canted antiferromagnetic state now occurs. In this new phase, electron spins in both layers are canted from the field direction due to the Coulomb interaction. This bulk phase was experimentally investigated [8, 9] and the obtained results are in good agreement with theoretical predictions [10–12].

The situation at the sample edge is expected to be more complicated. The ES structure is determined by both the edge potential and the bulk spectrum of a bilayer system. The latter can be very complicated even for the simplest situation of a total filling factor of $\nu = 2$ in the bulk [7–9, 13]. Moreover, the excitation spectrum is strongly dependent on the local filling factor, which varies widely at the sample edge. For these reasons, even a systematic of the excitations at the edge is unknown *ab initio*.

Here, we use a quasi-Corbino sample geometry to investigate the edge spectrum of excitations at a total filling factor of $\nu = 2$ in a bilayer electron system in normal and tilted magnetic fields while approaching the bulk phase transition from a spin-singlet to a canted antiferromagnetic state. At the bulk transition point, the *I–V* curve becomes linear, indicating a strong narrowing of the incompressible strip between two ESs.

Our bilayer structures are grown by molecular beam epitaxy on a semi-insulating GaAs substrate. The active layers form a 760 Å wide parabolic quantum well. In the center of the well, a three-monolayer-thick AlAs sheet is grown which serves as a tunnel barrier between both parts on either side. The symmetrically doped well is capped by 600-Å $Al_xGa_{1-x}As$ ($x = 0.3$) and 40-Å GaAs layers. The symmetric–antisymmetric splitting in the bilayer electron system as determined from far infrared measurements and model calculations [14] is equal to $\Delta_{SAS} = 1.3$ meV.

At zero gate voltage, the quantum well is practically symmetric, see Fig. 1 (solid line). It contains 4.2×10^{11} cm^{-2} electrons, which are distributed in both parts of the well. Applying a negative voltage to the gate makes the potential relief asymmetric (see Fig. 1, dashed line), indicating the depletion of the upper electron layer at low enough voltages.

This is illustrated in the inset to Fig. 1, where both measured (solid) and calculated (dashed) capacitances are shown as a function of the gate voltage in zero magnetic field. At the point of the abrupt changing of the capacitance (bilayer onset, $V_{on} = -0.3$ V), electrons are leaving the top part of the well and the distance between the gate and the 2D system is enlarged.

Samples are patterned in a quasi-Corbino geometry [5] (see Fig. 2). The square-shaped mesa has a rectangular etched region inside. Ohmic contacts are made to the inner and outer edges of the mesa (each of the contacts is connected to both electron systems in the two parts of the well). The top gate does not completely encircle the inner etched region but leaves uncovered a narrow (3 μm) strip (gate-gap) of 2DEG at the outer edge of the sample.

At integer total filling factor $\nu = 2$, edge channels are running along the etched edges of the sample (see Fig. 2). Depleting the electron system under the gate to a smaller integer filling factor $g = 1$ (as shown in the figure), one channel is reflected at the gate edge and redirected to the outer edge of the sample. In the gate-gap region, ESs originating from different contacts run in parallel along the outer (etched) edge of the sample, at a distance determined by the gate-gap width. Thus, the applied geometry allows us to separately contact ESs with different spin and layer indices and bring them into an interaction at a controllable length.

In our experimental setup, one of the inner contacts is always grounded. We apply a dc current to one outer ohmic contact and measure the dc voltage drop between two remaining inner and outer contacts. To increase the Zeeman splitting with respect to other energy scales, in our bilayer structure, we apply an in-plane magnetic field at fixed normal field by tilting the

sample. Experiments are performed at a temperature of 30 mK in magnetic field up to 14 T.

Measured *I–V* curves are presented in Fig. 3 for normal and tilted magnetic fields for a filling factor of $\nu = 2$ in the gate gap and $g = 1$ under the gate.

In normal magnetic field, the obtained *I–V* curve is of a diode-like form. It is nonlinear and consists of two branches, which starts from corresponding onset voltages—positive V_{th}^{+} and negative V_{th}^{-} thresholds. In between these thresholds, the current is practically zero. The positive branch of *I–V* is close to linear and characterized by low resistance. In contrast, the negative branch is strongly nonlinear and of higher resistance, see Fig. 3.

In normal magnetic field, the positive threshold V_{th}^{+} is close to the bare Zeeman splitting (0.21 meV in a field of 8.7 T). The negative threshold is one order of magnitude higher (V_{th}^{-} is about 2 meV) and corresponds to Δ_{SAS} in our bilayer structure. In both cases, it is a problem to estimate the experimental accuracy—the exact value of the threshold depends on the determination method. For example, the positive threshold we can define either by an extrapolation from high currents or as the voltage at which a significant current appears. These values are slightly different, as can be seen from Fig. 3. For the negative threshold, the second method seems to be more appropriate because of the strong nonlinear form of the curve. Nevertheless all relevant energy scales in a bilayer system (Zeeman splitting, symmetric–antisymmetric splitting, and a cyclotron splitting, which is about 15 meV here) are very different, so it is easy to assign a threshold to the appropriate spectral gap.

Both threshold voltages are strongly dependent on the in-plane field, see Fig. 3. They are diminishing with increasing in-plane field and disappear at a tilt angle of $\theta = 45°$. A calculated *I–V* trace for the case of full equilibration between two ESs is also shown in Fig. 3 (dash–dot line) for the comparison with $\theta = 45°$ data. It can be seen that, despite disappearance of the threshold voltages at $\theta = 45°$, the experimental curve is still slightly nonlinear.

The curves in Fig. 3 are given for two sweep directions—from positive to negative currents and vice versa. A small hysteresis can be seen. It is a maximum in normal magnetic field, becomes smaller at a tilt angle of $\theta = 30°$, and disappears at $\theta = 45°$. This hysteresis is a key feature for transport between two spin-split ESs [15–17]—for some electrons, spin flip is accompanied by nuclear spin flop. The hysteresis is an effect of the high nuclear relaxation time (for a thorough discussion, see [17]).

The dramatic influence of the in-plane magnetic field on the experimental *I–V* traces can also be seen from Fig. 4a. It demonstrates *I–V* curves in a much wider current/voltage range. The experimental nonlinear *I–V* curves are clearly flattening when the in-plane field increases. At a tilt angle of $\theta = 45°$, even the curve shape is very different from the normal field case.

The described behavior is totally different from that of a single-layer structure, where no influence of the in-

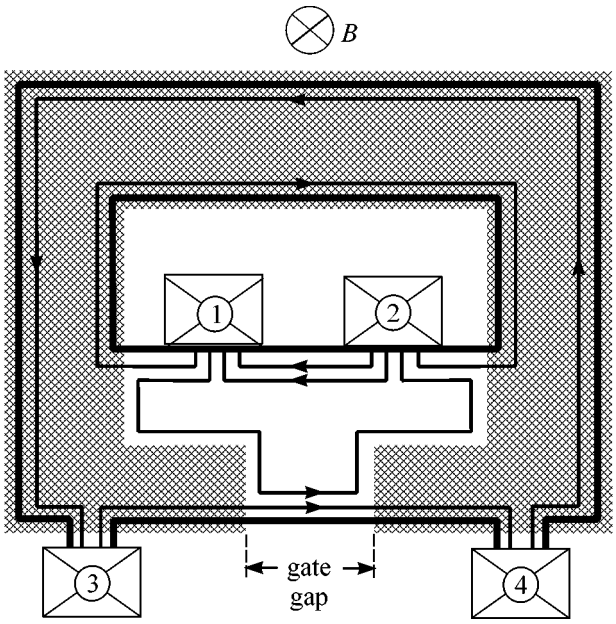

Fig. 2. Schematic diagram of the pseudo-Corbino geometry. Contacts are positioned along the etched edges of the ring-shaped mesa (thick outline). The shaded area represents the Schottky gate. Arrows indicate the direction of electron drift in the edge channels for filling factors of $\nu = 2$ in the ungated regions and $g = 1$ under the gate.

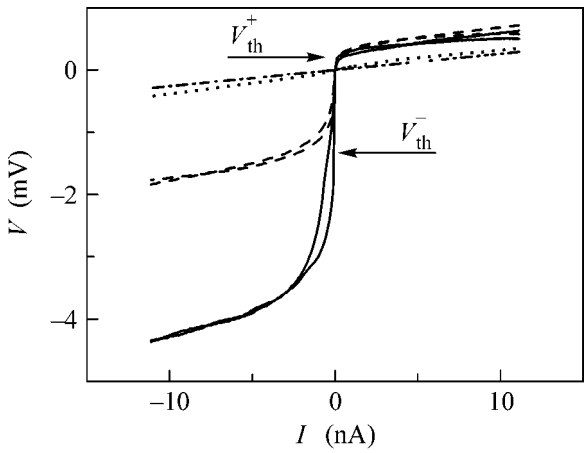

Fig. 3. *I–V* curves for a total filling factor of $\nu = 2$ and $g = 1$ under the gate at different tilt angles. They are $\theta = 0$ (solid line), $\theta = 30°$ (dashed line), $\theta = 45°$ (dotted line). Dash–dot line depicts fully equilibrium *I–V* curve, calculated from Landau–Buttiker formulas. The normal magnetic field is constant and equals 8.7 T.

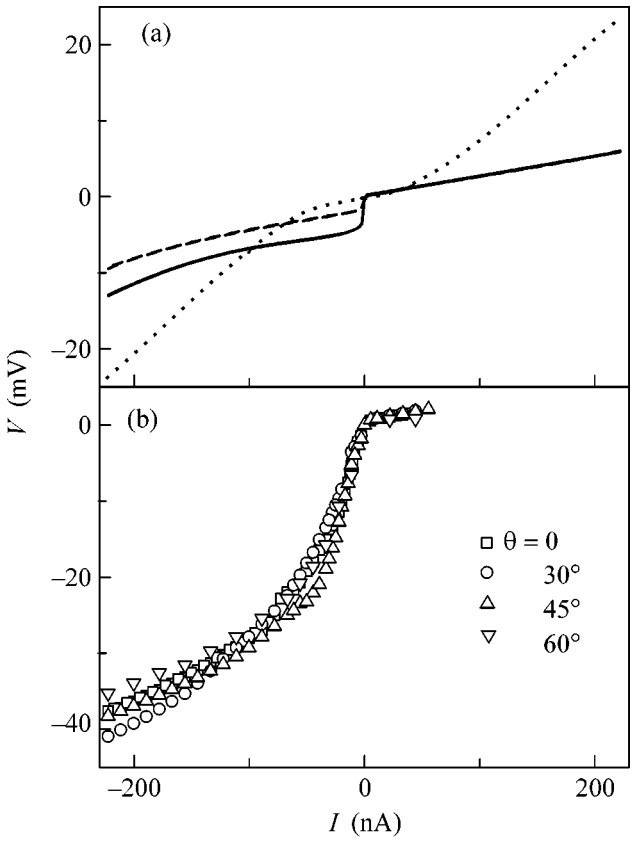

Fig. 4. *I–V* curves for a total filling factor of ν = 2 and $g = 1$ under the gate at different tilt angles in a wide current/voltage range. (a) The present bilayer system. The tilt angles are θ = 0 (solid line), θ = 30° (dashed line), θ = 45° (dotted line). (b) A single-layer heterostructure, discussed in [17]. The tilt angles are θ = 0 (squares), θ = 30° (circles), θ = 45° (up triangles), θ = 60° (down triangles).

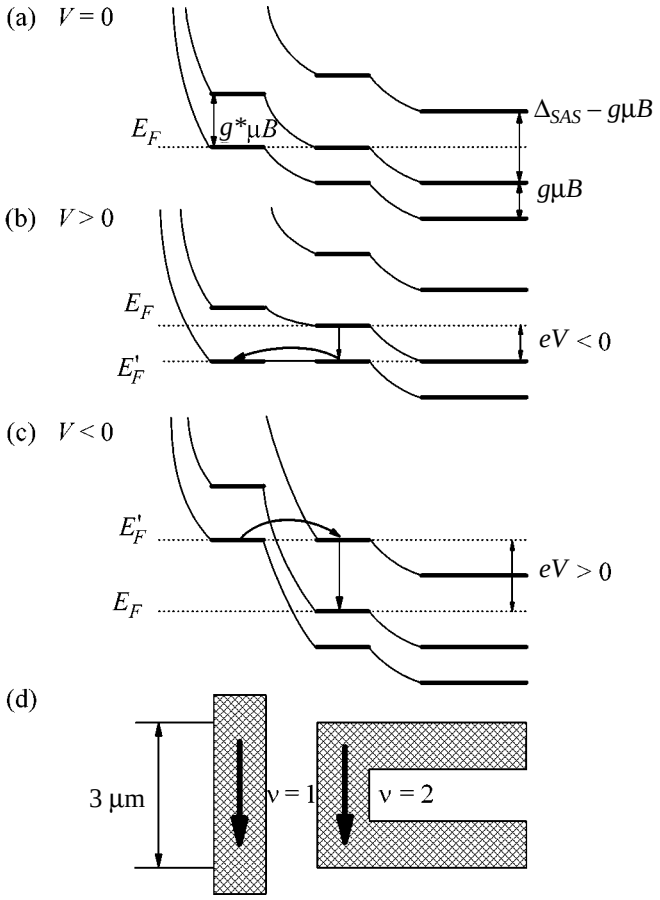

Fig. 5. Energy subband diagram of the sample edge in the gate gap for filling factors of ν = 2 and $g = 1$. (a) No voltage V applied between the inner and outer ESs. (b) $V > 0$, in the situation shown, the outer ES is shifted down in energy by $eV = -|g|\mu_B B$; (c) $V < 0$, here the energy shift is $eV > 0$. (d) Sketch of the compressible strips in the gate-gap region. Arrows in Figs. 5b and 5c indicate new ways for electron relaxation opening up at high potential imbalance.

plane magnetic field on the nonlinear *I–V* curves can be observed [17]. To demonstrate it in comparison with the bilayer data, we present in Fig. 4b *I–V* curves for a single-layer structure [17] at different tilt angles. Because of high hysteresis in a single-layer case, these curves are obtained by waiting for 10 min at each point to have time-independent *I–V* curves. From both the values of the thresholds and tilted field behavior, we should conclude that bilayer properties are important in the present experiment.

Using the gated part of the sample for magnetocapacitance measurements, we reproduced the previously obtained results [9, 13] on the bulk bilayer spectrum at a total filling factor of ν = 2 in normal and tilted magnetic fields: (i) In normal magnetic field, the bulk activation energy, obtained from the magnetocapacitance, is close to the single-particle Δ_{SAS}. (ii) While increasing the in-plane magnetic field component, the bulk bilayer system goes to the transition into the canted antiferromagnetic phase. This phase transition is characterized by the appearance of a deep minimum in the activation energy at a tilt angle of θ = 45°.

Let us start the discussion from the case of normal magnetic field. The bulk bilayer system at a filling factor of ν = 2 is in a spin-singlet state [13] and is far from the phase transition point. The energy structure in the bulk at a filling factor of ν = 2 can therefore be depicted in a single-particle approximation as two filled quantum levels under the Fermi energy separated by the Zeeman gap. The energy level structure is depicted in Fig. 5a in the gate-gap region. Approaching the sample edge, two occupied energy levels bend up because of the rising edge potential.

In our experimental geometry, we independently contact inner (always grounded) and outer ESs. For this reason the measured voltage drop V is equal to the energy shift of the outer ES in respect to the inner one, see Figs. 5b and 5c. For a positive measured voltage,

$V > 0$, the outer ES is shifted down in energy by a value of $eV < 0$. It can be seen from Fig. 5b that, at the value of the voltage $V = V_{th}^{+} = -|g|\mu B/e$ (where g is the bare g factor, $e < 0$ is the electron charge), the lowest (the only occupied in both ESs) energy level is flattened between two ESs, so that electrons can easily move from one ES into the other. Thus, starting from the $eV_{th}^{+} = -|g|\mu B$, electrons can be transferred between ESs by vertical relaxation in the inner ES between two spin-split levels and move along the lowest energy level to the outer ES, see Fig. 5b. This positive voltage V_{th}^{+} is characterized by a sharp rise in the current; i.e., it is a threshold voltage for the positive branch of the *I–V* curve. It is a reason for the experimentally observed V_{th}^{+} to be close to the bare Zeeman gap. On the other hand, a negative voltage shifts the outer ES up in energy. Electrons always have to tunnel through the potential barrier from the outer ES into the inner one. This tunneling is only possible from the occupied states in the outer ES either into the empty states in the inner ES or into the excited energy states in it. The latter process (with further vertical relaxation in the inner ES to the Fermi level) is more likely for $eV > E_a$, where E_a is the energy of the first excited state. For this reason, experimental *I–V* traces change their slopes at $eV = E_a$, which we refer to as the negative threshold voltage V_{th}^{-}. As we know from bulk spectrum investigations, at a filling factor of $\nu = 2$, the first excited state is separated from the ground state by Δ_{SAS}. It is a reason for V_{th}^{-} to be close to Δ_{SAS} in normal magnetic field.

For an increase of the in-plane magnetic field component, the Coulomb interaction becomes more and more important, so that the simple single-particle picture described above is no longer adequate. In the bulk, the quantum levels are mixed into a new ground state of the system, which is separated from the excited state by a very low energy at the transition point [10]. Approaching the sample edge, the electron concentration is diminishing due to the edge potential. The local filling factor is still $\nu = 2$ before the inner ES and becomes $\nu = 1$ in between the inner and outer ESs (see Fig. 5d). The energy structure at the edge is determined by the local filling factor, so the system is still at $\nu = 2$ ground state before the inner ES and changes to the $\nu = 1$ ground state between two ESs. In the inner ES, the electron concentration changes from the value corresponding to $\nu = 1$ to the value $\nu = 2$.

The electron system in the vicinity of the $\nu = 1$ incompressible strip can be described as a $\nu = 1$ ground quantum Hall state with some amount of electron excitations (right side of $\nu = 1$ strip in Fig. 5d), or as a $\nu = 1$ ground quantum Hall state with some amount of holes, on the opposite side of the $\nu = 1$ strip. It is the edge potential in the $\nu = 1$ incompressible strip that separates electrons and holes on both sides of the strip. Consequently, the main result of our experiment should be interpreted as a practical disappearance of this potential barrier (or, possibly, of the incompressible $\nu = 1$ strip itself) under conditions of the canted antiferromagnetic phase in the bulk. In these conditions, electrons can freely move between ESs without spin-flips, so there is no reason both for the nonlinear behavior of experimental *I–V* traces and for the hysteresis on them.

We used a quasi-Corbino sample geometry with independent contacts to different edge states in the quantum Hall effect regime to investigate the edge spectrum of a bilayer electron system at a total filling factor of $\nu = 2$. By analyzing nonlinear *I–V* curves in normal and tilted magnetic fields, we found that the edge energy spectrum is in a close connection with the bulk one. At the bulk transition spin-singlet–canted antiferromagnetic phase, the *I–V* traces become linear, indicating the disappearance of the potential barrier between $\nu = 1$ ground state with some amount of electron excitations and the $\nu = 1$ ground state with some amount of holes at the edge of the sample.

We wish to thank Dr. A.A. Shashkin for help during the experiments and discussions. We gratefully acknowledge financial support by the Deutsche Forschungsgemeinschaft, SPP "Quantum Hall Systems," under grant no. LO 705/1–2. The part of the work performed in Russia was supported by the Russian Foundation for Basic Research and the programs "Nanostructures" and "Mesoscopies" from the Russian Ministry of Sciences. V.T.D. acknowledges support by the A. von Humboldt foundation. E.V.D. acknowledges support by the Russian Science Support Foundation.

REFERENCES

1. M. Büttiker, Phys. Rev. B **38**, 9375 (1988).
2. D. B. Chklovskii, B. I. Shklovskii, and L. I. Glazman, Phys. Rev. B **46**, 4026 (1992).
3. For a review see R. J. Haug, Semicond. Sci. Technol. **8**, 131 (1993).
4. G. Müller, E. Diessel, D. Wiess, *et al.*, Surf. Sci. **263**, 280 (1992).
5. A. Würtz, R. Wildfeuer, A. Lorke, *et al.*, Phys. Rev. B **65**, 075303 (2002).
6. G. Müller, D. Weiss, A. V. Khaetskii, *et al.*, Phys. Rev. B **45**, 3932 (1992).
7. A. Sawada, Z. F. Ezawa, H. Ohno, *et al.*, Phys. Rev. Lett. **80**, 4534 (1998); A. Sawada, Z. F. Ezawa, H. Ohno, *et al.*, Phys. Rev. B **59**, 14888 (1999).
8. V. Pellegrini, A. Pinczuk, B. S. Dennis, *et al.*, Phys. Rev. Lett. **78**, 310 (1997); V. Pellegrini, A. Pinczuk, B. S. Dennis, *et al.*, Science **281**, 799 (1998).
9. V. S. Khrapai, E. V. Deviatov, A. A. Shashkin, *et al.*, Phys. Rev. Lett. **84**, 725 (2000).

10. S. Das Sarma, S. Sachdev, and L. Zheng, Phys. Rev. Lett. **79**, 917 (1997); Phys. Rev. B **58**, 4672 (1998); E. Demler and S. Das Sarma, Phys. Rev. Lett. **82**, 3895 (1999); L. Brey, E. Demler, and S. Das Sarma, Phys. Rev. Lett. **83**, 168 (1999).
11. T. Jungwirth, S. P. Shukla, L. Smrcka, *et al.*, Phys. Rev. Lett. **81**, 2328 (1998); A. H. MacDonald, P. M. Platzman, and G. S. Boebinger, Phys. Rev. Lett. **65**, 775 (1990).
12. S. V. Iordanski and A. Kashuba, Pis'ma Zh. Éksp. Teor. Fiz. **75**, 419 (2002) [JETP Lett. **75**, 348 (2002)].
13. V. T. Dolgopolov, A. A. Shashkin, E. V. Deviatov, *et al.*, Phys. Rev. B **59**, 13235 (1999).
14. M. Hartung, A. Wixforth, K. L. Campman, and A. C. Gossard, Solid State Electron. **40**, 113 (1996); G. Salis, B. Graf, K. Ensslin, *et al.*, Phys. Rev. Lett. **79**, 5106 (1997).
15. D. C. Dixon, K. R. Wald, P. L. McEuen, and M. R. Melloch, Phys. Rev. B **56**, 4743 (1997).
16. T. Machida, S. Ishizuka, T. Yamazaki, *et al.*, Phys. Rev. B **65**, 233304 (2002).
17. E. V. Deviatov, A. Wurtz, A. Lorke, *et al.*, cond-mat/0303498.
18. J. J. Koning, R. J. Haug, H. Sigg, *et al.*, Phys. Rev. B **42**, 2951 (1990). Our measurements of the onset voltage for the positive branch at cyclotron split filling factor combinations will be published elsewhere.

JETP Letters, Vol. 79, No. 4, 2004, pp. 177–182. From Pis'ma v Zhurnal Éksperimental'noĭ i Teoreticheskoĭ Fiziki, Vol. 79, No. 4, 2004, pp. 212–217.

The Anisotropic Conductivity of Two-Dimensional Electrons on a Half-Filled High Landau Level¶

I. S. Burmistrov

Landau Institute for Theoretical Physics, Russian Academy of Sciences, Moscow, 117940 Russia
Institute for Theoretical Physics, University of Amsterdam, 1018 XE Amsterdam, The Netherlands
e-mail: burmi@itp.ac.ru

Received January 22, 2004

We study the conductivity of two-dimensional interacting electrons on the half-filled Nth Landau level with $N \gg 1$ in the presence of quenched disorder. The existence of the unidirectional charge-density wave state at temperature $T < T_c$, where T_c is the transition temperature, leads to the anisotropic conductivity tensor. We find that the leading anisotropic corrections are proportional to $(T_c - T)/T_c$ just below the transition, in accordance with the experimental findings. Above T_c, the correlations corresponding to the unidirectional charge-density wave state below T_c result in corrections to the conductivity proportional to $\sqrt{T_c/(T - T_c)}$. © *2004 MAIK "Nauka/Interperiodica".*

PACS numbers: 73.20.Mf; 71.45.Lr

1. INTRODUCTION

Two-dimensional electrons in a perpendicular magnetic field was a subject of intensive studies, both theoretical and experimental, for several decades [1, 2]. It has been found that the properties of two-dimensional electrons in the magnetic field are strongly affected by the presence of electron–electron interaction as well as by impurities. The behavior of the system in a strong magnetic field where only the lowest Landau level is occupied has been investigated in great detail [2]. But only a few attempts were made to consider the system in a *weak* magnetic field (large number of Landau levels $N \gg 1$ are occupied) where the Coulomb energy at distances of the order of the magnetic length exceeds the cyclotron energy [3].

Progress in understanding the clean two-dimensional electrons in a weak magnetic field was achieved by Aleiner and Glazman, who, by using the small parameter $1/N \ll 1$, have derived the successive theory that describes electrons on the partially filled Nth Landau level [4]. By treating the effective electron–electron interaction on the Nth Landau level within the Hartree–Fock approximation, Koulakov, Fogler, and Shklovskii [5] predicted a unidirectional charge-density-wave (UCDW) state (stripe phase) for the half-filled high Landau level at zero temperature and in the absence of disorder. Moessner and Chalker [6] showed the existence of the UCDW state on the half-filled high Landau level without disorder below some temperature T_0. In the presence of disorder, the UCDW state on the half-filled high Landau level can exist if the Landau level broadening $1/2\tau$ does not exceed the critical value $1/2\tau_c = 4T_0/\pi$ [7]. (We use the system of units with $\hbar = 1$, $c = 1$, and $k_B = 1$ throughout the letter.)

The anisotropic magnetoresistance discovered near half-fillings of Landau levels at low temperatures was attributed to the existence of the UCDW state [8]. This stimulates an extensive study of the properties of two-dimensional electrons in a weak magnetic field [9]. However, to date, the magnetoresistance of the UCDW state has been theoretically considered in the zero temperature limit only where stripes have well-defined edges [9].

The main objective of the present letter is to present the results for the conductivity tensor of the UCDW state developed on the half-filled high Landau level in the presence of the quenched disorder just below the transition temperature T_c, where the expansion in the CDW order parameter Δ is justified.

2. UCDW STATE

The two-dimensional electrons in a weak perpendicular magnetic field H occupy a large number ($N \gg 1$) of the Landau levels. We assume that disorder is *weak*, so it leads to the Landau level broadening $1/2\tau$ that satisfies the condition $1/2\tau \ll \omega_H$, where $\omega_H = eH/m$ is the cyclotron frequency, with e and m being the electron charge and the effective electron mass, respectively. Simultaneously, we imply that the number of impurities exceeds the number of states on the Landau level, i.e., impurities lift the degeneracy of the Landau level completely [11]. This means that the Landau level broadening $1/2\tau$ should be larger than $\omega_H|a|/z_0$, where a stands

¶ This article was submitted by the author in English.

for the impurity scattering length and z_0 ($\gg|a|$) is the decay length of the electron wave function in the direction perpendicular to the two-dimensional plane. Thereby, we assume that the Landau level broadening $1/2\tau$ satisfies the condition $\omega_H|a|/z_0 \ll 1/2\tau \ll \omega_H$. As the temperature decreases, transition from the homogeneous state to the UCDW state occurs. Vector **Q** that characterizes a period of the UCDW can be oriented along a spontaneously chosen direction. Usually, the orientation is fixed either by the intrinsic anisotropy of the crystal or by the small external in-plane magnetic field [9]. Hereinafter, we assume that the vector **Q** is directed under angle ϕ with respect to the x axis. The period of the UCDW seems to be of the order of the cyclotron radius $R_c = l_H\sqrt{2N+1}$, where $l_H = 1/\sqrt{m\omega_H}$ denotes the magnetic length. More precisely, the modulus of the vector **Q** equals $Q = r_0/R_c$, where $r_0 \approx 2.4$ is the first zero of the zeroth order Bessel function of the first kind $\mathcal{J}_0(z)$ [5, 7]. In the mean-field approximation, the temperature T_c of the second-order transition from the homogeneous to UCDW state is determined as the solution of the following equation [7]:

$$\frac{T_c}{T_0} = \frac{2}{\pi^2}\zeta\left(2, \frac{1}{2} + \frac{1}{4\pi T_c\tau}\right), \quad (1)$$

where $\zeta(2, z)$ is the generalized Riemann zeta function and T_0 is the transition temperature in the *clean* case ($1/\tau \ll T_0$). We notice that Eq. (1) has a solution for T_c only if the Landau level broadening is smaller than the critical one $1/2\tau \le 1/2\tau_c = 4T_0/\pi$. According to [5, 6],

$$T_0 = \frac{r_s\omega_H}{4\pi\sqrt{2}}\left[\ln\left(1 + \frac{c}{r_s}\right) - \frac{c}{\sqrt{2} + r_s}\right], \quad \frac{1}{N} \ll r_s \ll 1, \quad (2)$$

where $c = 1/(\sqrt{2}\, r_0) \approx 0.3$, and $r_s = \sqrt{2}\, e^2/\varepsilon v_F \ll 1$, with v_F and ε being the Fermi velocity and the dielectric constant of a media, respectively. It is worth mentioning that T_0 is determined by the characteristic energy $e^2/R_c \sim r_s\omega_H \ll \omega_H$ of the screened electron–electron interaction on the Nth Landau level.

If we take into account the fluctuations of the UCDW order parameter, the transition becomes of the first order at lower temperature $T_c - \delta T$, where $\delta T/T_c \propto h_1(\eta_c)N^{-2/3}$ [7]. Here, for convenience, we introduce the dimensionless parameter $\eta_c = 1/4\pi T_c\tau$, which we use throughout the letter. The function $h_1(\eta_c)$ decreases monotonically from the value 0.46 at $\eta_c = 0$ to zero at $\eta_c \longrightarrow \infty$. As it is known, the fluctuations of the UCDW order parameter produce power divergences and, therefore, destroy it in the infinite system. In the finite system of size L, the UCDW state survives, provided that the condition $L/R_c \ll h_2(\eta_c)N^{1/3}$ holds. Here, the function $h_2(\eta_c)$ monotonically increases from the value 0.55 at $\eta_c = 0$ to infinity at $\eta_c \longrightarrow \infty$. Therefore, in the considered case of a weak magnetic field ($N \gg 1$), the effect of the fluctuations on the transition is negligible and the mean-field picture is well justified.

3. RESULTS

The conductivity tensor σ_{ab} of the two-dimensional electrons on the half-filled high Landau level above the transition temperature T_c, i.e., in the homogeneous state, is known to be isotropic [1]. To this end, we show that, in the presence of the *quenched weak* disorder, the existence of the UCDW state on the half-filled high Landau level below T_c results in *anisotropic* corrections to the isotropic conductivity tensor σ_{ab}. For a temperature slightly below T_c, where the condition $T_c - T \ll T_c$ holds, the anisotropic corrections are given as

$$\left.\begin{matrix}\delta\sigma_{xx}^{(\mathrm{anis})}\\ \delta\sigma_{yy}^{(\mathrm{anis})}\end{matrix}\right\} = \mp Nf(\eta_c)\mathcal{G}(\eta_c)\cos[2\phi]\frac{T_c - T}{T_c}, \quad (3)$$

and

$$\left.\begin{matrix}\delta\sigma_{xy}^{(\mathrm{anis})}\\ \delta\sigma_{yx}^{(\mathrm{anis})}\end{matrix}\right\} = Nf(\eta_c)\mathcal{G}(\eta_c)\sin[2\phi]\frac{T_c - T}{T_c}. \quad (4)$$

The functions $f(z)$ and $g(z)$ are defined as

$$f(z) = \frac{32\mathcal{J}_1^2(r_0)z^3}{\left(\frac{1}{2} + z\right)^5}, \quad g(z) = \frac{16\pi z}{\left(\frac{1}{2} + z\right)\left(z^2 + \left(\frac{1}{2} + z\right)^2\right)}, \quad (5)$$

where $g(z)$ will be used below. The other function $\mathcal{G}(z)$ is given as

$$\mathcal{G}(z) = \frac{\zeta\left(2, \frac{1}{2} + z\right) - z\zeta\left(3, \frac{1}{2} + z\right)}{-3\zeta\left(4, \frac{1}{2} + z\right) + 4\Phi_0(z) + 2\Phi_2(z)}, \quad (6)$$

with

$$\Phi_n(z) = \frac{\zeta\left(2, \frac{1}{2} + z\right)}{z^2\mathcal{J}_0^2(nr_0)} - \frac{\mathrm{Im}\psi\left(\frac{1}{2} + z + iz\mathcal{J}_0(nr_0)\right)}{z^3\mathcal{J}_0^3(nr_0)}. \quad (7)$$

The $\psi(z)$ stands for the digamma function, and the symbol Im denotes the imaginary part.

There are several features of the main results (3) and (4). First of all, the anisotropic corrections $\delta\sigma_{ab}^{(\mathrm{anis})}$ are proportional to $(T_c - T)/T_c$. Although Eqs. (3) and (4) are derived only for the case of a short-range random potential (quenched disorder), it can be shown that the anisotropic corrections remain proportional to $(T_c - T)/T_c$ in the case of a long-range random potential that corresponds to high mobility samples used in experiments [8] as well. We emphasize that such temperature

dependence of the developing anisotropy in magnetoresistance was observed in the experiments [8].

The angle dependence of the anisotropic correction (3) to conductivity σ_{xx} has the minimum for $\phi = 0$ that corresponds to the vector **Q** directed along the *x* axis and stripe oriented along the *y* axis. From Eq. (3), we see that the conductivity σ_{yy} along the stripe is enhanced, whereas the conductivity σ_{xx} across the stripes (along the modulation of the order parameter) is suppressed, as it should be according to the experiments [8]. At the same time, the anisotropic correction (4) to σ_{xy} vanishes. If the vector **Q** is oriented at angle $\phi = \pi/4$ with respect to the *x* axis, the anisotropic correction (3) to σ_{xx} becomes zero due to the symmetry between the *x* and *y* axes. Conversely, the anisotropic correction (4) to σ_{xy} attains the minimum.

The behavior of the anisotropic corrections (3) and (4) as the functions of the parameter η_c for fixed temperature *T* and angle ϕ are shown in Fig. 1.

In addition, the existence of the UCDW state on the half-filled high Landau level leads to the isotropic correction that, for $T_c - T \ll T_c$, is as follows:

$$\delta\sigma_{xx}^{(\mathrm{isot})} = -\frac{N}{\pi}[g(\eta_c) + f(\eta_c)]\mathcal{G}(\eta_c)\frac{T_c - T}{T_c}. \quad (8)$$

The behavior of the isotropic correction (8) as a function of η_c for fixed temperature *T* is shown in Fig. 1.

4. MODEL

The grand canonical partition function of the two-dimensional interacting electrons in the random potential $V(r)$ subjected to the perpendicular constant magnetic field *H* and the time-dependent external vector potential **A** is given by

$$\mathcal{Z} = \int \mathcal{D}[\Psi, \Psi^\dagger]\mathcal{D}[V]\mathcal{P}[V]\exp\mathcal{S}_0[\Psi, \Psi^\dagger, V], \quad (9)$$

where the action $\mathcal{S}_0[\Psi, \Psi^\dagger, V]$ in the Matsubara representation has the form

$$\mathcal{S}_0 = \int_r \Psi^\dagger(\mathbf{r})[i\omega + \mu - \mathcal{H}_0 + \hat{K} - V(\mathbf{r})]\Psi(\mathbf{r}) - \frac{T}{2}\int_{rr'\alpha\nu_n}\sum \Psi^\dagger(\mathbf{r})I_n^\alpha\Psi(\mathbf{r})\frac{e^2}{\varepsilon|\mathbf{r}-\mathbf{r}'|}\Psi^\dagger(\mathbf{r}')I_{-n}^\alpha\Psi(\mathbf{r}'). \quad (10)$$

Here, we use the matrix notation $\Psi^\dagger(\ldots)\Psi = \Psi^{\dagger\alpha}_{\omega_n}(\ldots)^{\alpha\beta}_{nm}\Psi^\beta_{\omega_m}$ for the electron annihilation $\Psi^\alpha_{\omega_n}(\mathbf{r})$ and creation $\Psi^{\dagger\alpha}_{\omega_n}(\mathbf{r})$ operators. Superscripts $\alpha, \beta = 1, \ldots, 2N_r$ stand for replica indices combined with spin ones. We introduce the replica indices in order to average over the random potential $V(\mathbf{r})$. The subscripts ω_n, ω_m denote the Matsubara fermionic frequencies $\omega_n = \pi T(2n + 1)$. The one-particle Hamiltonian $\mathcal{H}_0$ for a two-dimensional electron in the presence of the magnetic field $H = \epsilon_{ab}\partial_a A_b^{\mathrm{st}}$ is defined as $\mathcal{H}_0 = -\mathbf{D}^2/(2m)$ with the covariant derivative $\mathbf{D} = \nabla - ie\mathbf{A}^{\mathrm{st}}$. The matrix ω has only diagonal elements $\omega^{\alpha\beta}_{nm} = \omega_n\delta^{\alpha\beta}\delta_{nm}$ that represent the Matsubara frequencies ω_n. The matrix I_n^α with elements $(I_n^\alpha)^{\beta\gamma}_{lm} = \delta^{\alpha\beta}\delta^{\gamma\alpha}\delta_{m-l,n}$ is a generator of the $U(1)$ gauge transformation. The time-dependent external vector potential **A** is involved through the matrix $\hat{K} = \sum_{\alpha,n} K(\nu_n)I_n^\alpha$, where

$$K(\nu_n) = -\frac{e}{m}\mathbf{A}(\nu_n)\mathbf{D} + \frac{e^2}{2m}\sum_{\nu_m}\mathbf{A}(\nu_{n-m})\mathbf{A}(\nu_m). \quad (11)$$

Here, $\mathbf{A}(\nu_n)$ is the Fourier component of the external vector potential **A** with frequency $\nu_n = 2\pi Tn$.

We assume the white-noise distribution for the random potential $V(\mathbf{r})$ is

$$\mathcal{P}[V(\mathbf{r})] = \frac{1}{\sqrt{2\pi g}}\exp\left[-\frac{1}{2g}\int_r V^2(\mathbf{r})\right]. \quad (12)$$

5. METHOD

To proceed, we integrate over the random potential $V(\mathbf{r})$ in Eq. (9). As usual, it leads to the quartic interaction that we decouple by introducing the matrix field $Q(\mathbf{r})$ [12]. The annihilation $\Psi(\mathbf{r})$ and creation $\Psi^\dagger(\mathbf{r})$ operators written in the basis of the eigenfunctions $\phi_{pk}(\mathbf{r})$ of the Hamiltonian $\mathcal{H}_0$

$$\Psi(\mathbf{r}) = \sum_{p,k}\psi_{pk}\phi_{pk}(\mathbf{r}), \quad \Psi^\dagger(\mathbf{r}) = \sum_{p,k}\psi^\dagger_{pk}\phi^*_{pk}(\mathbf{r}) \quad (13)$$

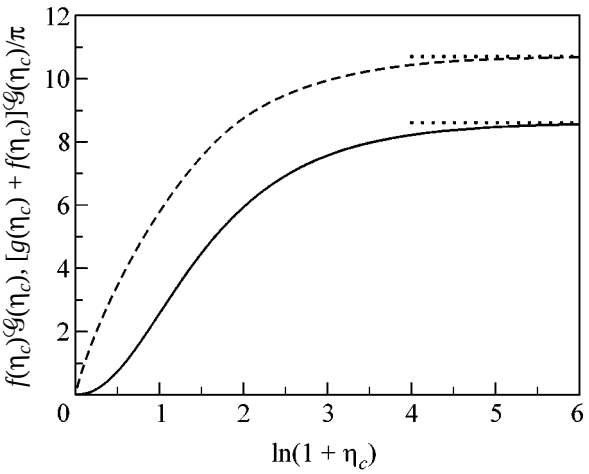

Fig. 1. The $f(\eta_c)\mathcal{G}(\eta_c)$ and $[g(\eta_c) + f(\eta_c)]\mathcal{G}(\eta_c)/\pi$ as functions of $\ln(1 + \eta_c)$.

involve the electron states on all Landau levels. Therefore, the term with the electron–electron interaction in the action (10) contains the interactions of electrons from different Landau levels. In general, to treat problem (10) analytically seems to be impossible. However, as it was shown in [4], if the $N-1$ Landau levels are filled, whereas the Nth Landau level is partially occupied, one can obtain a description of the system in terms of electrons on the Nth Landau level only provided that the relative strength of the bare Coulomb interaction is *small*, $r_s \ll 1$, and the magnetic field is rather *weak*, $Nr_s \gg 1$.

Following the same strategy as in [10], we obtain the grand canonical partition function $\mathcal{Z}$ as

$$\mathcal{Z} = \int \mathcal{D}[\Psi, \Psi^\dagger]\mathcal{D}[Q]\exp\mathcal{S}[\Psi, \Psi^\dagger, Q], \qquad (14)$$

where

$$\mathcal{S} = \int_r \Psi^\dagger(\mathbf{r})[i\omega + \mu - \mathcal{H}_0 + \hat{K} + iQ]\Psi(\mathbf{r}) - \frac{1}{2g}\mathrm{Tr}Q^2 \qquad (15)$$

$$-\frac{T}{2}\int_{rr'}\sum_{\alpha\nu_n}\psi^\dagger(\mathbf{r})I_n^\alpha\psi(\mathbf{r})U_{\mathrm{scr}}(\mathbf{r},\mathbf{r}')\psi^\dagger(\mathbf{r}')I_{-n}^\alpha\psi(\mathbf{r}').$$

Here, the symbol Tr denotes the trace over the Matsubara replica combined with spin and spatial indices. The electron–electron interaction is written in terms of electron operator $\psi(\mathbf{r}) = \sum_k \psi_{Nk}\phi_{Nk}(\mathbf{r})$ on the Nth Landau level only. The screened interaction $U_{\mathrm{scr}}(\mathbf{r})$ of electrons on the Nth Landau level takes into account the effects of electrons on the other levels and has the following form [4, 10]:

$$U_{\mathrm{scr}}(q) = \frac{2\pi e^2}{\varepsilon q}\frac{1}{1 + \dfrac{2\left(1 - \dfrac{\pi}{6\omega_H\tau}\right)}{qa_B}(1 - \mathcal{J}_0^2(qR_c))}. \qquad (16)$$

It is worth mentioning that the range of the screened electron–electron interaction (16) is determined by the Bohr radius $a_B = \varepsilon/me^2$. We assume that the magnetic field is so weak that the condition $Nr_s^2 \gg 1$ holds. That means that the range a_B of the screened electron–electron interaction (16) is much smaller than the magnetic length l_H. It allows us to treat the interaction in the Hartree–Fock approximation [6].

In the absence of the external vector potential $\mathbf{A}$, one can project the first line in Eq. (15) onto the Nth Landau level, i.e., substitute $\Psi(\mathbf{r}) \longrightarrow \Psi(\mathbf{r})$. Then, the action becomes to involve electrons on the Nth Landau level only and, evidently, it simplifies the analysis. The accuracy of such projection is of the order of $\max\{T, \tau^{-1}\}/\omega_H \ll 1$. It is worthwhile to mention that the correction $\pi/6\omega_H\tau \ll 1$ in the screened interaction (16) results in the correction of the same order to the T_0. For reasons to be explained shortly, we neglect this effect. However, in order to investigate the response of the system to the external vector potential $\mathbf{A}$, such projection onto the Nth Landau level is not appropriate. We should leave the action (15) as it stands, because the matrix elements $D^a_{p_1p_2} = \int_r \phi^*_{p_1k}(\mathbf{r})D^a\phi_{p_2k}(\mathbf{r})$ of the covariant derivative $\mathbf{D} = (D^x, D^y)$ involve the electron states on the adjacent Landau levels. As the last step, we mention that the electrons on the Nth Landau level should be regarded as spin-polarized, according to the numerical findings [14].

The action (15) involves the unitary matrix field $Q(\mathbf{r})$. There exists the saddle-point solution $Q(\mathbf{r}) = W^{-1}U_{\mathrm{sp}}W$ in the absence of the electron–electron interaction. Here, the constant unitary matrix W describes the global rotation, whereas $(U_{\mathrm{sp}})^{\alpha\beta}_{nm} = \delta^{\alpha\beta}\delta_{nm}\,\mathrm{sgn}\,\omega_n/2\tau$ with $1/2\tau = \sqrt{g/2\pi l_H^2}$. Being motivated by the form of the saddle-point solution, we split the matrix field $Q(\mathbf{r})$ in transverse $W(\mathbf{r})$ and longitudinal $U(\mathbf{r})$ components as $Q(\mathbf{r}) = W^{-1}(\mathbf{r})(U_{\mathrm{sp}} + U(\mathbf{r}))W(\mathbf{r})$. As it is well known, the transverse field $W(\mathbf{r})$ is responsible for weak localization corrections [12], but, in the case of interest, they are of the order of $\ln N/N \ll 1$. Therefore, we eliminate the transverse field from the future considerations by formally putting $W(\mathbf{r}) = 1$. The transformation of the variable $Q(\mathbf{r})$ discussed above leads to the additional measure in the functional integral [13]

$$\ln I[U] \sim \int_r \sum_{\omega_n\omega_m}^{\alpha\beta}[1 - \Theta(nm)]U^{\alpha\alpha}_{nn}(\mathbf{r})U^{\beta\beta}_{mm}(\mathbf{r}), \qquad (17)$$

where $\Theta(x)$ stands for the Heaviside step function.

To describe the UCDW state, we introduce the CDW order parameter Δ that is related with a distortion of the electron density on the Nth Landau level

$$\langle\delta\rho(\mathbf{q})\rangle = 2\pi l_H^{-2}F_{NN}(\mathbf{q})[\delta(\mathbf{q} - \mathbf{Q}) + \delta(\mathbf{q} + \mathbf{Q})]\Delta, \qquad (18)$$

where the $F_{p_1p_2}(\mathbf{q})$ is defined as

$$F_{p_1p_2}(\mathbf{q}) = 2\pi l_H^2\sum_k \phi^*_{p_1k}(0)\phi_{p_2k}(\mathbf{q}l_H^2)e^{i\frac{1}{2}q_xq_yl_H^2}. \qquad (19)$$

In particular, the form-factor $F_{NN}(q) \approx \mathcal{J}_0(qR_c)$ for $qR_c \ll 2N$. The presence of the distortion of the electron density by the charge-density wave on the Nth Landau level results in the additional periodic potential $\lambda(\mathbf{r})$ that is related with the UCDW order parameter as

$$\lambda(\mathbf{q}) = (4\pi)^2T_0F_{NN}^{-1}(q)[\delta(\mathbf{q} - \mathbf{Q}) + \delta(\mathbf{q} + \mathbf{Q})]\Delta. \qquad (20)$$

After the Hartree–Fock decoupling [15] of the interaction term in the action (15) and integration over electrons, we obtain

$$\mathcal{Z} \sim \int \mathcal{D}[U] I[U] \exp \mathcal{S}[U], \tag{21}$$

where the action becomes

$$\mathcal{S} = -\frac{1}{2g}\mathrm{Tr}U^2 + \mathrm{Tr}\ln(1 + (iU + \hat{K} + P_N \lambda P_N)G). \tag{22}$$

The projection operator $P_N(\mathbf{r}, \mathbf{r}') = \sum_k \phi_{Nk}(\mathbf{r})\phi^*_{Nk}(\mathbf{r}')$ in the action (22) indicates that the potential $\lambda(\mathbf{r})$ exists on the Nth Landau level only. In general, the UCDW state on the Nth Landau level creates the potential not only on the same level but also on the adjacent ones. We neglect this effect since it results in the corrections to the conductivity tensor σ_{ab} of the order of $1/N^2$ beside expressions (3), (4), and (8).

The saddle-point Green function $G^{\alpha\beta}_{nm}(\mathbf{r}, \mathbf{r}')$ is determined as

$$G^{\alpha\beta}_{nm}(\mathbf{r}, \mathbf{r}') = \delta^{\alpha\beta}\delta_{nm}\sum_{pk}\phi^*_{pk}(\mathbf{r})\phi_{pk}(\mathbf{r}')G^{-1}_p(\omega_n),$$
$$G^{-1}_p(\omega_n) = i\omega_n + \omega_H(p - N) + i\frac{\mathrm{sgn}\,\omega_n}{2\tau}. \tag{23}$$

We notice that Green function (23) coincides with the Green function averaged over disorder in the self-consistent Born approximation [1].

6. CONDUCTIVITY TENSOR

With the action (22) in hand, we can evaluate the contributions to the conductivity tensor σ_{ab} due to the presence of the UCDW state on the half-filled Landau level. As one can verify, the contributions of the first order in the UCDW induced potential $\lambda(\mathbf{r})$ vanish. In order to find the contributions to σ_{ab} of the second order in λ, we should expand the action (22) up to the second order in both λ and K. Then, integrating over the U fields, we obtain several contributions. We present the diagrams that correspond to them in the standard perturbative technique in Fig. 2.

The first three diagrams (Fig. 2a) yield only the isotropic contribution

$$\sigma^{(a)}_{ab}(\nu_n) = -T\sum_{\omega_n}\frac{G^3_N(\omega_n)}{1 + g\pi^{\omega_n}(0,0)}\frac{T_0^2\Delta^2}{(1 + g\pi^{\omega_n}(0,Q))^2} \times \frac{4\pi\omega_H}{\nu_n}\left(\frac{2}{m}\sum_p D^a_{Np}D^b_{pN}G_p(\omega_n + \nu_n) - \delta_{ab}\right). \tag{24}$$

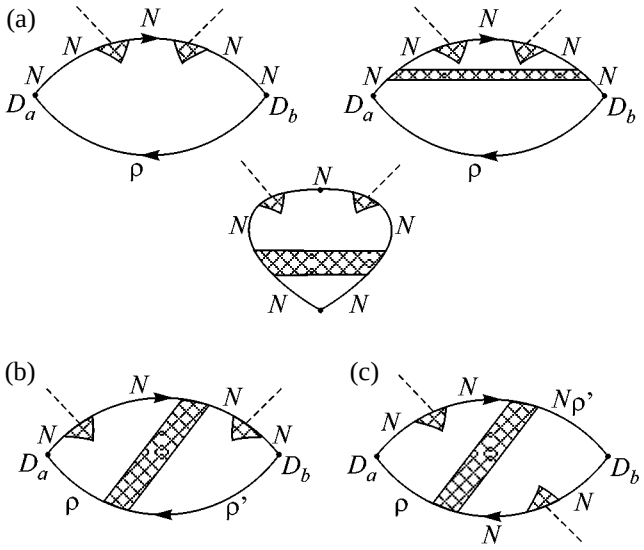

Fig. 2. Diagrams for the corrections to σ_{ab}. The solid lines are the Green functions, the $N/p/p'$ symbols denote the Landau level, the dashed lines are the UCDW induced potential $\lambda(\mathbf{r})$, and the shaded blocks are impurity ladders.

Here, the polarization operator $\pi^{\omega_n}(\nu_n, q)$ on the Nth Landau level is defined as

$$\pi^{\omega_n}(\nu_n, q) = -n_L G_N(\omega_n + \nu_n)G_N(\omega_n)F^2_{NN}(q). \tag{25}$$

The contribution of diagram (Fig. 2b) is seemed to be proportional to $\mathcal{J}_0(r_0)$ and therefore vanishes. The last diagram (Fig. 2c) is as follows:

$$\sigma^{(c)}_{ab}(\nu_n) = \frac{8\pi\omega_H}{\nu_n m}T\sum_{\omega_n}\frac{G^2_N(\omega_n)G^2_N(\omega_n + \nu_n)T_0^2\Delta^2}{(1 + g\pi^{\omega_n}(0,Q))(1 + g\pi^{\omega_n}(\nu_n, Q))} \times \sum_{pp'} G_p(\omega_n)G_{p'}(\omega_n + \nu_n)\frac{D^a_{pN}D^b_{p'N}I_{NpNp'}(\mathbf{Q})}{1 + g\pi^{\omega_n}(0,Q)}, \tag{26}$$

where a single impurity line is written in the Landau level indices representation as

$$I_{p_1p_2p_3p_4}(\mathbf{Q}) = g\int_q F_{p_1p_2}(\mathbf{q})F_{p_3p_4}(-\mathbf{q})e^{-i\mathbf{q}\mathbf{Q}l_H^2}. \tag{27}$$

The contribution (26) contains the anisotropic as well as isotropic corrections to σ_{ab}. If we take $p = p' = N \pm 1$, we obtain the anisotropic contribution due to the structure of matrix elements $D^a_{p_1p_2}$. The opposite case $p = N \pm 1$ and $p' = N \pm 1$ results in the isotropic correction.

Now, with the help of the results $I_{N,N\pm1,N,N\pm1} \approx ge^{\mp 2i\phi}\mathcal{J}^2_1(r_0)$ and $I_{N,N\pm1,N,N\mp1} \approx g\mathcal{J}^2_1(r_0)$, we perform the summation over the Landau level indices as

well as over the Matsubara frequency. As the last step, we express the UCDW order parameter Δ via the temperature difference $T_c - T \ll T_c$ as [7]

$$\Delta = \zeta\left(2, \frac{1}{2} + \eta_c\right)\sqrt{\mathcal{G}(\eta_c)}\sqrt{\frac{T_c - T}{T_c}} \tag{28}$$

and obtain the results (3), (4), and (8).

7. FLUCTUATIONS OF THE ORDER PARAMETER

There is a legitimate question about the effect of the fluctuations on the conductivity tensor above and below the transition temperature T_c. Below, we consider the former case as more interesting. At $T > T_c$, the mean-field order parameter $\Delta = 0$ on average, but the average of its square $\langle\Delta^2\rangle$ is nonzero. It leads to the appearance of the corrections to the conductivity tensor σ_{ab} above T_c due to the presence of the UCDW correlations. We can find the contributions of the order parameter fluctuations to σ_{ab} by substituting $\langle\Delta^2\rangle$ for Δ^2 in Eqs. (24) and (26).

Generally, the angle ϕ and modulus Q of the CDW vector $\mathbf{Q}$ can fluctuate simultaneously. Naturally, only the isotropic correction can appear in this case. Then, the result for the correction one can obtain from Eq. (8) with the help of the following substitutions:

$$\frac{T_c - T}{T_c} \longrightarrow \frac{r_0}{4\pi N}\sqrt{\frac{T_c}{T - T_c}},$$
$$\mathcal{G}(z) \longrightarrow \sqrt{\frac{\zeta^{-1}\left(2, \frac{1}{2} + z\right)}{\gamma\zeta\left(2, \frac{1}{2} + z\right) + \mathcal{J}_1^2(r_0)z^2\zeta\left(4, \frac{1}{2} + z\right)}}, \tag{29}$$

where $\gamma = \partial \ln T_0/\partial r_0 \approx 2.58$. It is worthwhile to mention that these fluctuational contribution (29) to σ_{ab} above T_c is analogous to the correction for conductivity of a normal metal due to superconducting pairing [16]. The fluctuation correction (29) has square-root divergence at $T \longrightarrow T_c$. This fact indicates that the result (29) is not applicable in the vicinity of the transition temperature T_c. The limit of applicability is determined by the requirement that the fluctuational correction should be much smaller than σ_{ab} itself.

8. CONCLUSIONS

Summarizing, we calculated the anisotropic, as well as isotropic, corrections to the conductivity tensor of the two-dimensional electrons on the half-filled high Landau level just below the transition to the UCDW state. The corrections obtained are proportional to $(T_c - T)/T_c$, which is in agreement with that found in the experiments. Also, we calculated the fluctuational correction to the conductivity tensor of the two-dimensional electrons above the transition.

I am grateful to M.A. Baranov, L.I. Glazman, M.V. Feigelman, S.V. Iordansky, P.M. Ostrovsky, and M.A. Skvortsov for illuminating discussions. Financial support from the Russian Foundation for Basic Research, the Russian Ministry of Science, Dynasty Foundation, Forschungszentrum Jülich (Landau Scholarship), and Dutch Science Foundation (FOM) is acknowledged.

REFERENCES

1. T. Ando, A. B. Fowler, and F. Stern, Rev. Mod. Phys. **54**, 437 (1982).
2. *The Quantum Hall Effect*, Ed. by R. E. Prange and S. M. Girvin (Springer, Berlin, 1987; Mir, Moscow, 1989).
3. A. H. MacDonald and S. M. Girvin, Phys. Rev. B **33**, 4009 (1986); A. P. Smith, A. H. MacDonald, and G. Gumbs, Phys. Rev. B **45**, 8829 (1992); L. Belkhir and J. K. Jain, Solid State Commun. **94**, 107 (1995); R. Morf and N. d'Ambrumenil, Phys. Rev. Lett. **74**, 5116 (1995).
4. I. L. Aleiner and L. I. Glazman, Phys. Rev. B **52**, 11296 (1995).
5. A. A. Koulakov, M. M. Fogler, and B. I. Shklovskii, Phys. Rev. Lett. **76**, 499 (1996); Phys. Rev. B **54**, 1853 (1996).
6. R. Moessner and J. T. Chalker, Phys. Rev. B **54**, 5006 (1996).
7. I. S. Burmistrov and M. A. Baranov, Phys. Rev. B **68**, 155328 (2003).
8. M. P. Lilly, K. B. Cooper, J. P. Eisenstein, *et al.*, Phys. Rev. Lett. **82**, 394 (1999); R. R. Du, D. C. Tsui, H. L. Stormer, *et al.*, Solid State Commun. **109**, 389 (1999); J. P. Eisenstein, M. P. Lilly, K. B. Cooper, *et al.*, Physica E (Amsterdam) **9**, 1 (2000).
9. M. Fogler, in *High Magnetic Fields: Applications in Condensed Matter Physics and Spectroscopy*, Ed. by C. Berthier, L.-P. Levy, and G. Martinez (Springer, Berlin, 2002).
10. I. S. Burmistrov, Zh. Éksp. Teor. Fiz. **122**, 150 (2002) [JETP **95**, 132 (2002)].
11. E. M. Baskin, L. N. Magarill, and M. V. Entin, Zh. Éksp. Teor. Fiz. **75**, 723 (1978) [Sov. Phys. JETP **48**, 365 (1978)].
12. K. B. Efetov, A. I. Larkin, and D. E. Khmel'nitzkiĭ, Zh. Éksp. Teor. Fiz. **79**, 1120 (1980) [Sov. Phys. JETP **52**, 568 (1980)].
13. A. M. M. Pruisken, Nucl. Phys. B **235**, 277 (1984).
14. X.-G. Wu and S. L. Sondhi, Phys. Rev. B **51**, 14725 (1995).
15. H. Fukuyama, P. M. Platzman, and P. W. Anderson, Phys. Rev. B **19**, 5211 (1979).
16. L. G. Aslamasov and A. I. Larkin, Phys. Lett. A **26**, 238 (1968).

JETP Letters, Vol. 79, No. 4, 2004, pp. 183–187. From Pis'ma v Zhurnal Éksperimental'noĭ i Teoreticheskoĭ Fiziki, Vol. 79, No. 4, 2004, pp. 218–222.

Anticrossing Phenomena in a Resonator with 2D Electrons on Liquid Helium¶

J. Klier[1], A. Würl[1], and V. Shikin[2]

[1] *Fakultät für Physik, Universität Konstanz, 78457 Konstanz, Germany*

[2] *Institute of Solid State Physics, Russian Academy of Sciences, Chernogolovka, Moscow region, 142432 Russia*

Received January 22, 2004

We have investigated the details of the eigenmode for a resonator containing a two-dimensional electron system (2DES) formed on the surface of liquid helium. We show that anticrossing phenomena occur near the crossing point $\omega_0 = \omega_c$, where ω_0 is the eigenmode of the resonator and ω_c is the cyclotron frequency. The structure of the coupling constant is established. It is a flexible parameter, i.e., sensitive especially to magnetic field and electron density. A finite coupling leads to a perturbation, $\delta\omega$, of the eigenmode of the resonator in presence of the 2DES. Corresponding calculations and measurements of $\delta\omega$ are presented. The theory fits the experimental data. The influence of anticrossing on the cyclotron resonance absorption line shape is demonstrated. © *2004 MAIK "Nauka/Interperiodica".*

PACS numbers: 67.70.+n; 73.20.-r; 73.50.-h

Cyclotron resonance (CR) measurements in magnetic fields represent a valuable method of studying the electronic properties of two-dimensional electron systems (2DESs). In low density electron systems, the CR is usually investigated by using a resonator cavity (see, e.g., [1–8]). Under these conditions, the CR of the electrons appears when the requirement

$$\omega_0 = \omega_c \tag{1}$$

is fulfilled. Here, ω_0 is the resonator eigenmode and $\omega_c = (eB)/(m_e c)$ is the electron cyclotron frequency in magnetic field B, m_e is the free electron mass, e is the elementary charge, and c is the velocity of light.

However, this condition is only correct in the limiting case $n_s \longrightarrow 0$, where n_s is the average density of the 2DES. If $n_s \neq 0$, then the coupling between the resonator mode and the 2DES becomes important due to the development of anticrossing mode repulsion around the crossing point $\omega_0 = \omega_c$ (1). The effect of anticrossing in the system "resonator + 2DES" is similar to well-known phenomena, e.g., the predissociation effect in the behavior of diatomic molecules [9], the dispersion of the dielectric constant near atomic oscillator eigenmodes [10], energy gaps in the free electron spectrum caused by periodical potential perturbation [10, 11], the so-called polariton effect in dielectrics [12], etc. It has surmised to be fixed in any CR measurements [1–8]; however, this effect was not discussed so far (to be correct, see comment [13]). Here, we present a detailed analysis of this problem and show the influence of anticrossing phenomena in CR absorption measurements.

The main information about "anticrossing" is extracted from measurements of the shift of the eigenmode of the resonator, $\delta\omega$, caused by the presence of a 2DES. For these investigations, the setup shown in the inset in Fig. 1 has been used. Details of this setup are discussed in [8].

The resonator eigenmode is determined by the position of the maximum of the transmission signal. Examples of such signal structures are presented in Fig. 1. A typical set of data for ω_e, the eigenmode of the resonator in presence of electrons as function of B and electron density n_s is shown in Fig. 2. These data can be understood as a combination of two contributions, i.e.,

$$\omega_e = \omega_0 + \delta\omega, \text{ with } \delta\omega = \delta\omega_\sigma + \delta\omega_p, \tag{2}$$

where ω_0 is the eigenmode of the empty resonator with just the Si substrate inside it (at fixed liquid helium level and electric field $E_\perp = 0$; see Fig. 1).

The first contribution, $\delta\omega_\sigma$, is due to the finite conductivity of the 2DES. In the limiting case, when the coupling constant $\sigma \ll 1$ (the definition of σ is shown below in Eq. (8)), the shift σ is a linear function of n_s (at least when $B \longrightarrow 0$). So, we obtain

$$\delta\omega_\sigma(n_s, B)\big|_{B\to 0} \propto n_s, \quad \delta\omega_\sigma(n_s, B)\big|_{B\to\infty} \longrightarrow 0. \tag{3}$$

The second contribution in $\delta\omega$, $\delta\omega_p$, results from the sensitivity of the eigenmode on the liquid helium level and $E_\perp$ in the resonator (the electric pressing field applied to the Si substrate). Such a shift is not sensitive to magnetic field and has a nonlinear dependence on n_s.

¶ This article was submitted by the authors in English.

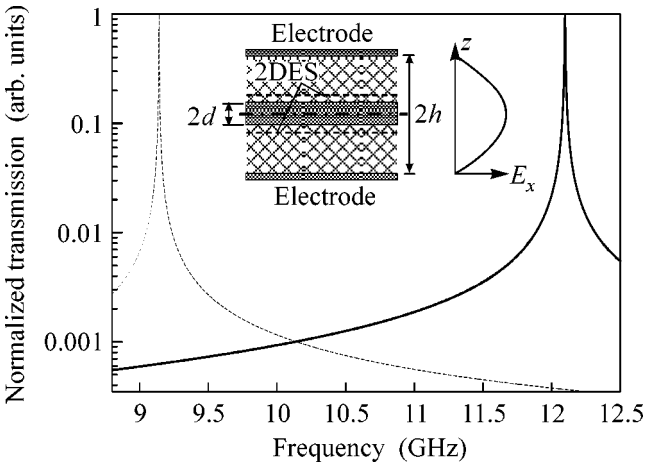

Fig. 1. The measured transmission signals for the empty resonator (solid line) and for the system "resonator + Si" (dashed line), with eigenmodes ω_{empty} and ω_0, respectively. Inset: schematical sketch of the cavity and, at the center, of the dielectric Si substrate with a helium film around it (the total thickness is $2d$). Two high frequency coax lines (not shown) are connected left and right to the resonator to apply the microwave excitation to the system "resonator + 2DES" and measure its transmitted signal. $2h$ is the distance between the upper and lower electrodes. On the right, a typical profile of the electric field E is shown.

Using Eqs. (2) and (3), we can renormalize the experimental data presented in Fig. 2. The results are shown in Figs. 3 and 4. Figure 3 presents the shift $\delta\omega_\sigma$ versus B. It is evident that the distribution $\delta\omega_\sigma$ follows the requirements in (2) and (3): $\delta\omega_\sigma$ is additive with $\delta\omega_p$ (Fig. 4), is linear dependent on n_s, and goes to zero when $B \longrightarrow \infty$.

To check the properties of $\delta\omega_p$, we have plotted its dependence against the normalized electron density (see Fig. 4). As indicated above, the shift $\delta\omega_p$ includes two effects. One of them corresponds to a decreasing eigenmode when $E_\perp \neq 0$ (without the presence of electrons, i.e., $n_s = 0$). In this case, the electric field lifts the helium level and so the eigenmode goes down (see Fig. 1). The other effect, when $n_s \neq 0$, arises from the electron pressure, $P_{el} \propto eE_\perp n_s$, which pushes the helium level down and, hence, the eigenmode increases (see Fig. 4). Variances of this shift have been discussed [14].

To explain the data in Fig. 3, we need the dispersion calculated for the model setup (inset in Fig. 1). The Maxwell equations for the E mode with

$$E_z = 0, \quad E_y = 0, \quad E_x \neq 0, \tag{4}$$

are completed by the boundary conditions. The electric fields are zero for $z = \pm h$. Along the boundaries $z = \pm d$ of the Si layer, we have to equate E_x from both sides of these boundaries.

It is also necessary to take into account the contribution arising from the presence of the movable 2DES. The 2D electrons are localized along the helium film, with thickness d_{He}, above the Si substrate. Typically, $d_{He} < d$, where $2d$ is the thickness of the Si substrate

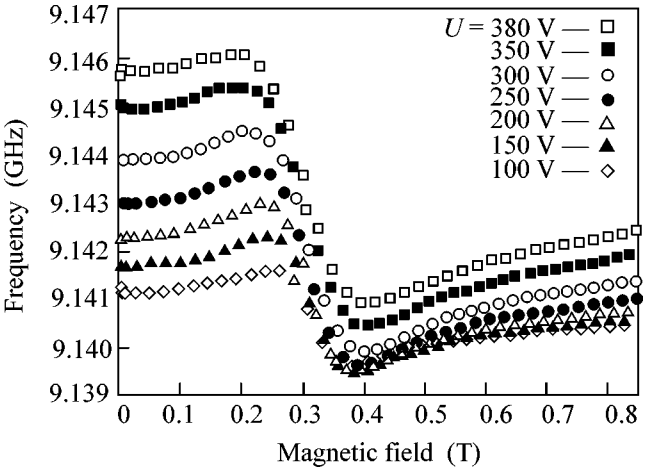

Fig. 2. The measured dependence of ω_e vs. B for several electron densities. The experimental conditions correspond to a saturation density of the 2D electron layers on the bulk helium surface. Therefore, $n_s \propto U$, where U is the potential difference between the Si substrate and the cavity. Here, $U_{crit} = 384$ V; i.e., this potential corresponds to the maximum charge density, $n_s^{crit} = 2 \times 10^{12}$ m^{-2}, on a bulk helium surface due to the electrohydrodynamical instability.

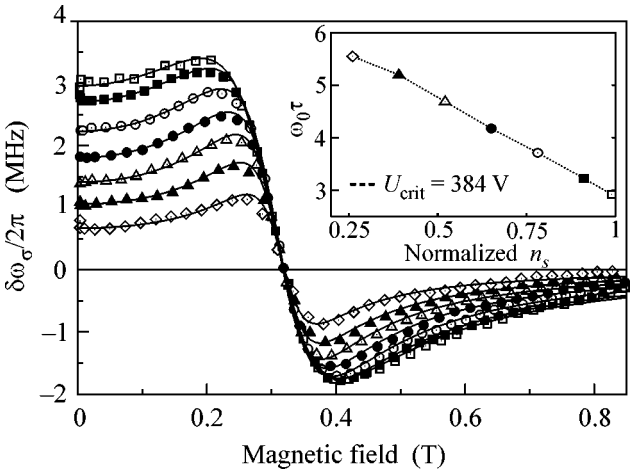

Fig. 3. The dependence of $\delta\omega_\sigma$ vs. B. $\delta\omega_\sigma$ is extracted from the measured data in Fig. 2 using Eqs. (2) and (3). The solid lines represent the fits to the data using Eq. (10) and the relaxation time τ as fitting parameter. Inset: the dependence of $\omega_0\tau$ on n_s after the fitting program (Eq. (10)) has been realized. Here, the data are normalized to the maximum density, at $U_{crit} = 384$ V.

(see inset in Fig. 1) and $(\epsilon_{He} - 1) \ll (\epsilon_{Si} - 1)$. Therefore, and for simplification, we neglect the existence of d_{He}. ϵ_{He} and ϵ_{Si} are the dielectric constant of liquid helium and the Si substrate. As a result, we have, along the Si substrate, a jump of the magnetic field, caused by 2D electron motion,

$$H_y^{vac}(d) - H_y^{Si}(d) = \frac{4\pi j_x(d)}{c}, \quad (5)$$

with

$$j_x = en_s v_x,$$
$$\left(i\omega + \frac{1}{\tau}\right)v_x = \frac{eE_x}{m_e} + \omega_c v_y, \quad \left(i\omega + \frac{1}{\tau}\right)v_y = -\omega_c v_x, \quad (6)$$

where v_x and v_y are the components of the electron velocity and τ is the momentum relaxation time.

Based on these calculations, we can formulate the dispersion law as

$$\tan(qd) - \frac{\sin(kd) + \cos(kd)\cot(kh)}{\cos(kd) - \sin(kd)\cot(kh)} = \frac{4\pi i}{c}\sigma_{xx}, \quad (7)$$

where $k^2 = \dfrac{(\omega_e - \delta\omega_p)^2}{c^2}$ and $q^2 = \epsilon_{Si}\dfrac{(\omega_e - \delta\omega_p)^2}{c^2}$. σ_{xx} is the ac conductivity of the 2DES in magnetic field. Again, because the thickness of the helium film is much less than d, it is not important for the definition of ω_e. The result (7) has been published in [14] but without considering magnetic field.

The conductivity $\sigma_{xx}(\omega, \omega_c)$ of the 2DES is described by the conventional ac Drude form

$$\sigma_{xx} = \sigma'_{xx} + i\sigma''_{xx},$$

$$\text{with } \sigma'_{xx} = \sigma'(\omega\tau, \omega_c\tau), \quad \sigma''_{xx} = \sigma''(\omega\tau, \omega_c\tau),$$

where ω is the external pumping frequency.

From Eq. (7), it becomes evident that the coupling constant σ is defined as

$$\sigma = \frac{4\pi i}{c}\sigma_{xx}. \quad (8)$$

If σ is small enough ($\sigma \ll 1$), then the general expression (Eq. (7)) can be simplified; i.e.,

$$\tan(q_0 d) - \frac{\sin(k_0 d) + \cos(k_0 d)\cot(k_0 h)}{\cos(k_0 d) - \sin(k_0 d)\cot(k_0 h)} = 0$$
$$\text{with } k_0^2 = \frac{\omega_0^2}{c^2} \text{ and } q_0^2 = \epsilon_{Si}\frac{\omega_0^2}{c^2}. \quad (9)$$

$$h\delta\omega'_\sigma = 4\pi\sigma''_{xx}(\omega_0, \omega_c) f, \quad (10)$$

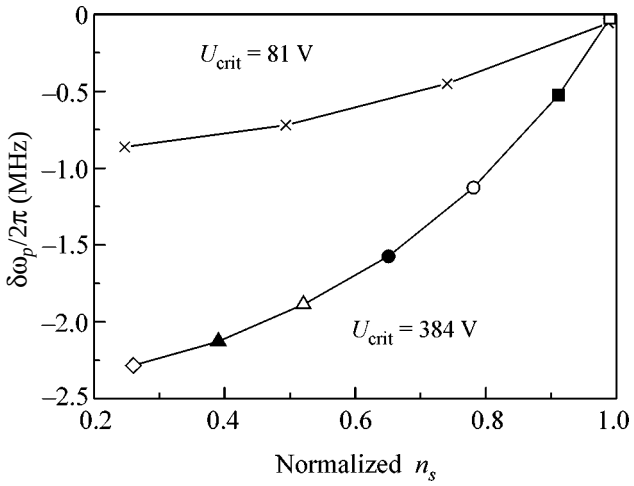

Fig. 4. The shift $\delta\omega_p$ vs. normalized electron density ("1" along the horizontal axis corresponds to the given critical value of n_s^{crit}). The lower line corresponds to the data shown in Figs. 2 and 3, when U_{crit} = 384 V. The upper line shows $\delta\omega_p$ measured for a thinner bulk helium film, with U_{crit} = 81 V. The observed dependence reflects the sensitivity of the transmission signal to the helium level; i.e., the electron pressure P_{el} is proportional to U^2. So, $\delta\omega_p$ is a nonlinear function of U.

$$h\delta\omega''_\sigma = 4\pi\sigma'_{xx}(\omega_0, \omega_c) f,$$
$$f = \cos(k_0 d)\sin(q_0 d)\frac{\tan(k_0 d)\tan[d(q_0 - k)] - 1}{\cos[d(q_0 - k)]}. \quad (11)$$

We can see that, in linear approximation, when $\sigma \ll 1$, the shift $\delta\omega$ is proportional to the imaginary part of the conductivity, i.e., $\delta\omega'_\sigma \propto \sigma''_{xx}$. Such a dependence fits the experimental data for $\delta\omega_\sigma$, with the normalization in one point (see Fig. 3). Normalization allows one to circumvent the lack of knowledge of the electron density n_s and the geometrical factor f. Results similar to Eqs. (10) and (11), but for a different resonator geometry, have been obtained in [15].

From successful fitting to the data (solid lines in Fig. 3), we can conclude the following: (a) Eq. (2) is a reasonable presentation for $\delta\omega$; (b) the geometrical factor f in Eqs. (10) and (11) is not sensitive to both n_s and B; and (c) the scale of the coupling constant σ (Eq. (8)) is far from the resonance condition small enough. Using the data in Fig. 3 and an estimation of n_s via $U/d \sim en_s$, we can conclude that

$$0.01 < \mathrm{Re}\sigma|_{B \to 0} < 0.04, \quad (12)$$

where σ is from Eq. (8). This estimation is consistent with the simplifications Eqs. (9)–(11). It also indicates that the quality of the eigenmode peaks in the reflection

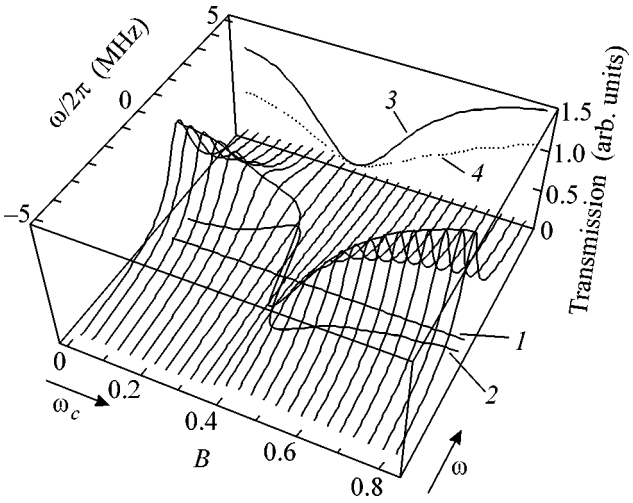

Fig. 5. Frequency scans (ω axis) as a function of the applied magnetic field *B* (along this axis, ω_c is determined). Each scan represents a measured transmission signal, $T(\omega, B)$, with the dependence of the maxima and signal shape on $\sigma''_{xx}(B)$. The trace in the ω, *B* plane (line *1*) corresponds to the condition $\omega = \omega_0$. Line *2* exhibits the path of the frequency at the maxima of the transmission lines. Details of this line are presented in Fig. 3. The trace in the *B*, *T* plane (line *3*) represents the CR absorption under optimal conditions, i.e., the maxima of the transmission signals. Line *4* reflects the situation for a fixed frequency, i.e., $\omega = \omega_c$, during the CR absorption measurements.

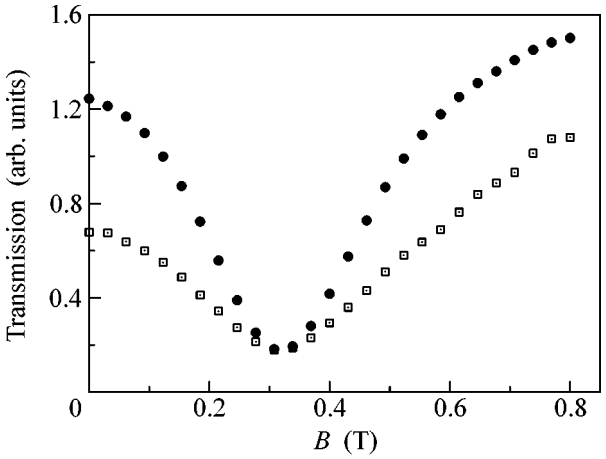

Fig. 6. A comparison of transmission vs. magnetic field for CR measurements with fixed ω (open symbols) and flexible ω (solid symbols).

(or transmission) data is much better than for the CR-line shape.

In Fig. 5, the general experimental picture of the transmission signal *T*, for the setup shown in the inset in Fig. 1, is presented as a function of *B* and ω. The profiles of $T(\omega, B)$ for fixed *B* but changing ω clearly show pronounced eigenmode peaks. The position of these peaks in the ω, *B* plane follows line *2*, formed in the vicinity of line *1* with $\omega = \omega_0$.

The quality of the peaks of the eigenmode goes down in the vicinity of the anticrossing area. The trace of the $T(\omega, B)$ profile in the ω, *T* plane corresponds to the information of the CR absorption. This trace is quite sensitive to the conditions of the projection.

Using the $T(\omega, B)$ presentation (Fig. 5), we can explain in detail the information (Fig. 6). The "solid" and "open" symbols correspond to projections of the $T(\omega, B)$ profile to the plane (*T*, *B*) (lines *3* and *4* in Fig. 5). Certainly, the optimal experimental path corresponds to line *3*.

In conclusion, we have demonstrated and explained the existence of anticrossing phenomena in the system "resonator + 2DES." The scale of the coupling constant σ (Eq. (8)) is deduced from the data (12). The coupling is flexible (it is sensitive to both magnetic field and electron density). Such a flexibility reduces $\delta\omega_\sigma$ to zero at the crossing point $\omega_0 = \omega_c$. However, in the vicinity of this point, the shift $\delta\omega_\sigma$ exists and can be measured. The experimental verification of the anticrossing phenomena is shown in Figs. 3 and 5. It looks like a $\delta\omega(B)$ shift, which is similar to the dielectric constant dispersion in optics (see [9, 10]). The general picture of the transmission signal versus ω and *B* in the presence of anticrossing phenomena is discussed (see Fig. 5). The details of the anticrossing cyclotron resonance line shift $\delta\omega_\sigma$ are investigated. The measured data of $\delta\omega_\sigma$ follow the predictions (Eq. (9)) quite well (see Fig. 3). The coupling between anticrossing phenomena and behavior of the CR absorption line width is discussed. The optimal way to measure such a line shape is indicated (see "solid" symbols in Fig. 6 and line *3* in Fig. 5).

We thank P. Leiderer for informative discussions. This activity is supported by the DFG, Forschergruppe "Quantengase," the EU-RTN "Surface Electrons on Mesoscopic Structures," and the Russian Foundation for Basic Research (grant no. 03-02-16121).

REFERENCES

1. G. Dresselhaus, A. F. Kip, and C. Kittel, Phys. Rev. **98**, 368 (1955).
2. T. R. Brown and C. C. Grimes, Phys. Rev. Lett. **29**, 1233 (1972).
3. V. Edel'man, Pis'ma Zh. Éksp. Teor. Fiz. **24**, 510 (1976) [JETP Lett. **24**, 468 (1976)]; Pis'ma Zh. Éksp. Teor. Fiz. **26**, 647 (1977) [JETP Lett. **26**, 493 (1977)].
4. V. Edel'man, Zh. Éksp. Teor. Fiz. **77**, 673 (1979) [Sov. Phys. JETP **50**, 338 (1979)].
5. L. Wilen and R. Giannetta, Phys. Rev. Lett. **60**, 231 (1988).

6. E. Teske, Yu. Monarkha, M. Seck, and P. Wyder, Phys. Rev. Lett. **82**, 2772 (1999).
7. Yu. Monarkha, E. Teske, and P. Wyder, Phys. Rev. B **59**, 14884 (1999); Phys. Rev. B **62**, 2593 (2000).
8. J. Klier, A. Würl, P. Leiderer, *et al.*, Phys. Rev. B **65**, 165428 (2002); and references therein.
9. L. D. Landau and E. M. Lifshitz, *Course of Theoretical Physics*, Vol. 3: *Quantum Mechanics: Non-Relativistic Theory*, 3rd ed. (Nauka, Moscow, 1974; Pergamon, New York, 1977).
10. J. M. Ziman, *Principles of the Theory of Solids* (Cambridge Univ. Press, London, 1964; Mir, Moscow, 1966), p. 269.
11. N. W. Ashcroft and N. D. Mermin, *Solid State Physics* (Holt, Rinehart and Winston, New York, 1976; Mir, Moscow, 1979), p. 826.
12. H. Raether, *Excitations of Plasmons and Interband Transitions by Electrons* (Springer, Berlin, 1980).
13. In Ref. [5], the existence of the anti-crossing problem for the system "resonator + 2DES" has been indicated (see comments in their Ref. [7]). However, there is no information with respect to $\delta\omega$ caused by anti-crossing phenomena (neither theoretically nor experimentally).
14. A. Würl, J. Klier, P. Leiderer, and V. Shikin, J. Low Temp. Phys. **126**, 511 (2002).
15. V. Shikin, Pis'ma Zh. Éksp. Teor. Fiz. **75**, 31 (2002) [JETP Lett. **75**, 29 (2002)].

JETP Letters, Vol. 79, No. 4, 2004, p. 188.

Erratum: "Electric Control of Magnetic Moment in a Ferromagnet/Semiconductor Hybrid System" [JETP Lett. 78 (9), 564 (2003)]

V. L. Korenev

PACS numbers: 85.35.Be; 85.75.-d; 99.10.Cd

In Eq. (2), *Jp* should be replaced by *Jg*.

P. 565, right column, 6th line from bottom should read "coupling parameter $K \equiv J^2 g/4\beta < 1$."

P. 567, left column, 15th line from bottom should read "5×10^8 Hz."

0021-3640/04/7904-0188$26.00